THE SPIN HALL EFFECT IN PLATINUM/FERROMAGNET MULTILAYERS AND ITS APPLICATION IN THREE-TERMINAL MAGNETIC TUNNEL JUNCTION STRUCTURES

A Dissertation

Presented to the Faculty of the Graduate School

of Cornell University

In Partial Fulfillment of the Requirements for the Degree of

Doctor of Philosophy

by

Minh-Hai Nguyen

August 2017

THE SPIN HALL EFFECT IN PLATINUM/FERROMAGNET MULTILAYERS AND ITS APPLICATION IN THREE-TERMINAL MAGNETIC TUNNEL JUNCTION STRUCTURES

Minh-Hai Nguyen, Ph. D.

Cornell University 2017

The spin Hall effect (SHE) has been shown to be strong in several heavy, nonmagnetic metals such as Pt, beta-phase Ta and beta-phase W. Owing to its relatively low electrical resistivity, Pt is a more favorable choice for the channel of three-terminal magnetic tunnel junction (3T-MTJ) devices for power efficient magnetoresistive memory applications.

In this dissertation, I will be discussing our efforts in understanding the dominant SHE mechanism in thin and nonuniform Pt films. Our results support the dominant role of the intrinsic SHE in Pt which implies that the spin Hall angle of Pt scales linearly with, and thus can be further enhanced by increasing, its resistivity. We demonstrate that by doping Pt with Hf impurities, the spin torque efficiency of $Pt_{85}Hf_{15}$/Co bilayer can be more than 2 times larger that of pure Pt due to 3 times higher resistivity. The second half of the dissertation describes the development of 3T-MTJ devices using a Pt channel. We demonstrate that a thin Hf spacer between the Pt channel and the MTJ results in 2 times lower magnetic damping without any significant detrimental effect on the interfacial spin transparency. Moreover, the 3T-MTJ devices with PtHf channel and a Hf spacer exhibit low power and nanosecond fast switching, promising for power efficient memory applications. We also demonstrate that the performace of Pt-based 3T-MTJ devices is robust at cryogenic temperatures, thus making this structure attractive for cryogenic applications.

BIOGRAPHICAL SKETCH

Minh-Hai Nguyen was born in 1985, the last year of the failed communist economic model that crippled the entire nation, in Duong, a small and isolated fishing village in a southern province of Vietnam. His early and serious myopia, which wasn't remedied until entering middle school, hindered him from physical activities with the neighbor kids, so he spent his childhood reading his father's rusty books on science and technology. The family later spent a vast portion of their saving and income to support his high school study in a nearby town where he made a rapid progress by the end of which he was awarded the Le Van Thiem Prize by the Vietnam Institute of Mathematics.

In 2005, he received the Monbusho scholarship by Japanese government to pursue his undergraduate study in electronics engineering at the University of Electro-Communications in Tokyo, Japan. The scholarship was later extended to his graduate study in Physics at Kyoto University with Prof. Sawada. After getting the Master degree, he was accepted to the Ph. D. program in Physics at Cornell University. He joined in Prof. Buhrman's research group in 2013 and started studying the spin Hall effect in metallic multilayers. Upon finishing his education at Cornell, he will join Intel Corporation as a Yield analyst. He got married in 2012 and is now living with his wife and one child.

To my parents,

who have always been supporting every of my adventures.

ACKNOWLEDGMENTS

All my scientific findings, professional and personal developments during these 5 years at Cornell would not be accomplished without the strong and consistent support of a great many mentors, colleagues and friends at Cornell, in Ithaca and in the U.S. to whom I am and will always be in huge debt.

My special thanks to my thesis advisor, Prof. Bob Buhrman, who has been following my work, offering guidance, scrutinizing the data and stimuling new ideas. I would like to thank Prof. Dan Ralph, who has always given helpful insights and advices, and Prof. Craig Fennie for his support.

My lab work has received a great support from my labmates. Chi-Feng Pai was a instructive mentor who helped me learn nanofabrication, magnetic characterization and measurements. Graham Rowlands spent a considerable amount of time tutoring me on instrumentation with Python. I also learned a lot of nanofabrication from Sriharsha Aradhya, and enjoyed the fruitful discussions with Yongxi Ou, Shengjie Shi, Junbo Park, Praveen Gowtham, Luis Vilela-Leão, Yun Li, Li Jun and Ryan Tapping.

A large part of my research would not be completed without the constructive collaboration with other groups at Cornell. I would like to thank Alex Mellnik, Colin Jermain, Neal Reynolds and Greg Stiehl in Ralph group for their scientific and technical help. Careful TEM imaging and analysis by Kayla Nguyen and Prof. David Muller were extremely helpful for us. I would also thank the CNF and CCMR staff who have been doing a good service in supporting our research, especially Rob Ilic, Garry Bordonaro, Alan Bleier, Steve Kriske and Nathan Ellis.

I am grateful for the support of the scientists at Raytheon BBN Technologies during my summer internship there, especially Graham Rowlands, Colm Ryan and Tom Ohki, and the espresso machine which helped keep us awake during long summer days. I also learned a lot from the useful discussions with many colleagues around the country: Satoru Emori, Kohei Ueda, Luqiao Liu and Tim Phung.

My research work would not be effectively carried out without a balanced private life. For that, I am indebted to Tam Tran and Duyen Bui, who helped us settle down in Ithaca, Hung Phi Tran's family and Alex-Thai Vo's family for always being there for us whenever we need help , teaching us American culture, politics and history.

I would never successfully complete my degree without the strong, consistent and patient support from my wife and the little kid. Finally, I would like to give special thanks to my father, who had initiated my scientific aspiration and home-schooled me in my early years, and my late mother, who had dedicated her entire life for the survival and wellbeing of the family.

TABLE OF CONTENTS

LIST OF ABBREVIATIONS

3T	three-terminal
AHE	anomalous/extraordinary Hall effect
AMR	anisotropic magnetoresistance
DL	damping-like
FL	field-like
FM	ferromagnetic, ferromagnet
FMR	ferromagnetic resonance
HM	heavy metal
HR	harmonic response
ISHE	inverse spin Hall effect
MRAM	magnetoresistive random access memory
MTJ	magnetic tunnel junction
NM	non-magnetic
PMA	perpendicularly magnetized anisotropy
RT	room temperature
SBF	spin back flow
SH	spin Hall
SHA	spin Hall angle
SHE	spin Hall effect
SML	spin memory loss
ST	spin torque
TMR	tunneling magnetoresistance

PREFACE

It has been an extremely active period of time for research on the spin Hall effect (SHE) in heavy metals since I joined Prof. Buhrman's group in summer 2013. Only two years before then the strong SHE in Pt reported by Luqiao Liu *et al.* caused an uproar in the magnetic and spintronic community, followed by reports on even larger spin Hall angles (SHAs) in Ta and W. Since then the number of new findings on the subject has exponentially increased. Its application in the three-terminal magnetic tunnel junction (3T-MTJ) devices attracted a great deal of attention from the memory industry, such as Samsung, HGST and Intel. Many mysteries were unveiled, debates raised and resolved, and some left unanswered.

My first project in Buhrman group was to reduce the Gilbert magnetic damping in Pt/FeCoB bilayers using a spacer, under the guidance of Chi-Feng Pai. By very careful etching, Chi-Feng and I were the first to make 3T-MTJ devices using a Pt channel. It came as a nice surprise that although a thin Hf spacer of about 0.5 nm can reduce the damping by half, it does not considerably affect the interfacial spin transparency. Consequently, our 3T-MTJ devices with a Pt channel and Hf spacer exhibited low switching currents in relatively low resistivity channels, thus making the structure suitable for low power MRAM applications. I will discuss these results in chapter 4.

My next attempt was to use Pt and Hf to create the A-15 lattice structure which we suspected to cause the giant SHE in beta-phase W. Although I wasn't successful on proving the relation of A-15 structure and giant SHE, I happened to get a strangely looking thickness dependence of the damping-like spin torque efficiency in Pt/Co bilayers. About the same time, I studied the SHE mechanisms and spin transport in multilayers for my A-exam, and attempted to develope a simple matrix formulation for spin current tranmission in multilayers that can be readily implemented on

computers. Combined with several sleepless nights, I came up with an elegant explanation for the "strangely looking" data which supports the Elliott-Yafet spin scattering mechanism and the intrinsic SHE in Pt. The details of this work will be discussed in chapter 2.

The confirmation of the intrinsic SHE in Pt has several important implications: First, it clears out some confusion regarding the values of SHA of Pt, especially determined at different temperatures in which there is a large variation of the resistivity. It points out that the determination of SHA of Pt thin and nonuniform films is not straightforward and needs more careful analysis. It also implies that the SHA of Pt is not a constant but rather can be enhanced by increasing its resistivity as long as the spin Hall conductivity is kept relatively constant. This led to my next project which was to dope Pt with impurities to increase its resistivity. The results show that a fraction of Hf impurities, about 15%, can boost the SHA to 2 -3 times larger due to 3 times higher resistivity and will be discussed in chapter 3. It was natural to apply these developments into the 3T-MTJ memory devices to reduce the critical current density. This was demonstrated in the work presented in chapter 6.

I started to get involved in the IARPA C3 program in my internship at Raytheon BBN Technologies in summer 2016. The C3 program attempts to design and demonstrate superconducting processing units in which the 3T-MTJ is an attractive option for their embedded cryogenic memory. Graham Rowlands and I developed a fast pulse measuring scheme which was later used to demonstrate the reliable switching of Pt-based 3T-MTJ devices at 3.1 K and its compatibility with the nTron devices (developed by Berggren group at MIT). The work is summarized in chapter 5.

During my 4 years in Buhrman group, the field of SHE has made a rapid progress in furthering our understanding of the nature of SHE in heavy metals / ferrormagnet multilayers.

However, there emerged many open questions to be investigated. The interfacial component of the SHE is still in active debate. The weak field-like effect complicates the analyses in experiments quantifying the spin torques and in switching measurements on 3T-MTJ devices. Those are addressed in the final chapter, chapter 7.

CHAPTER 1

The Spin Hall Effect in Nonmagnetic/Ferromagnetic Bilayers

This chapter outlines some of the key factors of the spin Hall effect (SHE) in metallic nonmagnetic / ferrormagnetic multilayers. I first review the discovery of the giant SHE in heavy metals such as Pt, β-Ta and β-W, and the controversy on the strength of the SHE in Pt, followed by three possible SHE mechanisms and their electrical properties. An important magnetic-spintronic application of the SHE in metals, the three-terminal magnetic tunnel junction, is then introduced. Finally, three methods to readily quantify the SHE-induced spin torques in multilayers that are employed in the experiments in later chapters are described.

1.1. The spin Hall effect in heavy metals

Compared to electrical charges, the spin degree of freedom has a much shorter history, starting from its first observation by the Stern-Gerlach experiment in 1922. Along with arduous scientific studies on electron as well as nuclear spins, theoretically and experimentally, the possibility to combine electron charges and spins to store and manipulate information, the so-called electro-spintronics (or usually spintronics for short), has always been tempting. The foremost and technologically challenging step is the generation of strong enough (electron) spin polarized currents, or spin currents for short. A number of optical and electrical methods, among which is the spin filtering by ferromagnetic (FM) thin films, were proposed, and the efficiency varies from one to another. The next step is to use the spin polarization and/or current to store or manipulate information. Using spins for storage faces many challenges, such as the confinement of spin polarization, protection from environmental noise (photons, heat and magnetic field) and readout methods. An alternative is to use spin currents for manipulating information, especially in magnetic logic and memory devices.

In 1996, J. C. Slonczewski [1] and L. Berger [2] independently proposed a mechanism for the interaction of electron spins and the magnetization in FM materials, called spin transfer torque (STT), or sometimes spin torque (ST) for short, in which spins exchange their angular momentum with the magnetization [3,4]. This openned up a new realm of scientific and technological exploration since it provides a convenient way to "transfer" spin currents to magnetic dynamics which can be electrically read out by magneto-resistive (MR) effects, such as the anisotropic MR (AMR) and tunneling MR (TMR). An immediate, and commercialized, application of this mechanism is the magnetic tunnel junction (MTJ) structure which consists of two FM layers separated by a thin insulating barrier, one of which (reference layer) has a fixed magnetization and

that of the other (free layer) can be flipped parallel or anti-parallel to it. A longitudinal spin current is generated by "spin filtering" of one or two FM layers and switches the magnetization of the free layer via STT [5], as illustrated in Fig. 1.1. The effectiveness of the switching depends on a number of factors including the magnitude of the spin current (i.e. the efficiency of spin filtering), Gilbert magnetic damping and magnetic anisotropy of the system. The shortcomings of this 2-terminal configuration, which will be discussed in section 1.3, originate from the basic requirement that an electrical current needs to be sent through the FM layers, and therefore the tunnel barrier, to generate a longitudinal spin current.

The possibility of switching the FM magnetization by a transverse spin current was demonstrated by Miron *et al*. [6] in perpendicularly magnetized anisotropy (PMA) Pt/Co bilayers, but was then attributed to the Rashba effect [7] at the interface. About the same time and independently, Liu *et al.* demonstrated the strong anti-damping effect of current-induced spin torque on the ferromagnetic resonance (FMR) lineshape in Pt/Py (Py = $Ni_{81}Fe_{19}$) bilayers [8] and soon later the switching of Pt/Co PMA samples [9], but this time attributed the origin of the anti-damping torque to the spin Hall effect (SHE) [10–12] in the bulk of the Pt layer, by which opposite spin accumulations are built on the top and bottom surfaces on the Pt film due to spin-dependent transverse movement of electrons of opposite spins, as illustrated in Fig. 1.2. Since the Rashba effect and SHE are described by overlapping formulisms in which they both induce damping-like and field-like torques, it is not experimentally straightforward to distinguish one from the other. Although the origin of the current-induced spin torques in Pt and some other heavy metals such as Ta and W is still an ongoing debate, recent measurements on the dependence of the spin torque on the thickness of a Hf spacer in W/Hf/CoFeB PMA structures [13] suggested the bulk SHE origin of the current-induced transverse spin current. It is also the viewpoint of the works presented in

this dissertation.

The main objection to the strong SHE in nonmagnetic (NM) metals is its relative strength determined experimentally comparing to the theoretically evaluated values. The most common figure of merit for the SHE is the spin Hall angle (SHA), defined as the ratio of the SHE-induced spin current density and the electrical current density, given by

$$\vec{j_s} = \theta_{\mathrm{SH}} \cdot (\vec{\sigma} \times \vec{j_e}) \qquad (1.1)$$

where $\vec{\sigma}$ is the spin polarization, $\vec{j_s}$ and $\vec{j_e}$ are the spin and electrical current densities, respectively, and θ_{SH} the SHA. The values of SHA were found by spin-torque FMR, harmonic response, in-plane MTJ switching measurements (discussed below in section 1.4) and some other techniques to be large, 0.07 - 0.12 for Pt [8,14–16], -(0.11 – 0.15) for β-phase Ta [16,17] and -(0.30 – 0.33) for β-phase W [18] (note that Pt has positive SHA while Ta and W have negative SHAs), much larger than theoretically calculated values. Fig. 1.3 shows calculated values of (intrinsic) spin Hall conductivity = $\theta_{\mathrm{SH}} / \rho$ (ρ: resistivity) using the tight-binding model for 4d and 5d elements, reproduced from Ref. [19]. Note that for typical resistivities of 20, 200 and 200 μΩcm for Pt, β-Ta and β-W, respectively, from Fig. 1.3, the SHAs for those materials are about 0.02, -0.05 and -0.05, about 3 – 5 times smaller than the experimentally estimated values mentioned above. A compresenive list of SHA values can be found in Table 1 of Ref. [20] and Table 1 of Ref. [21]. However, more recent theoretical works support the large SHA of Pt [22,23] which is more consistent with experiments.

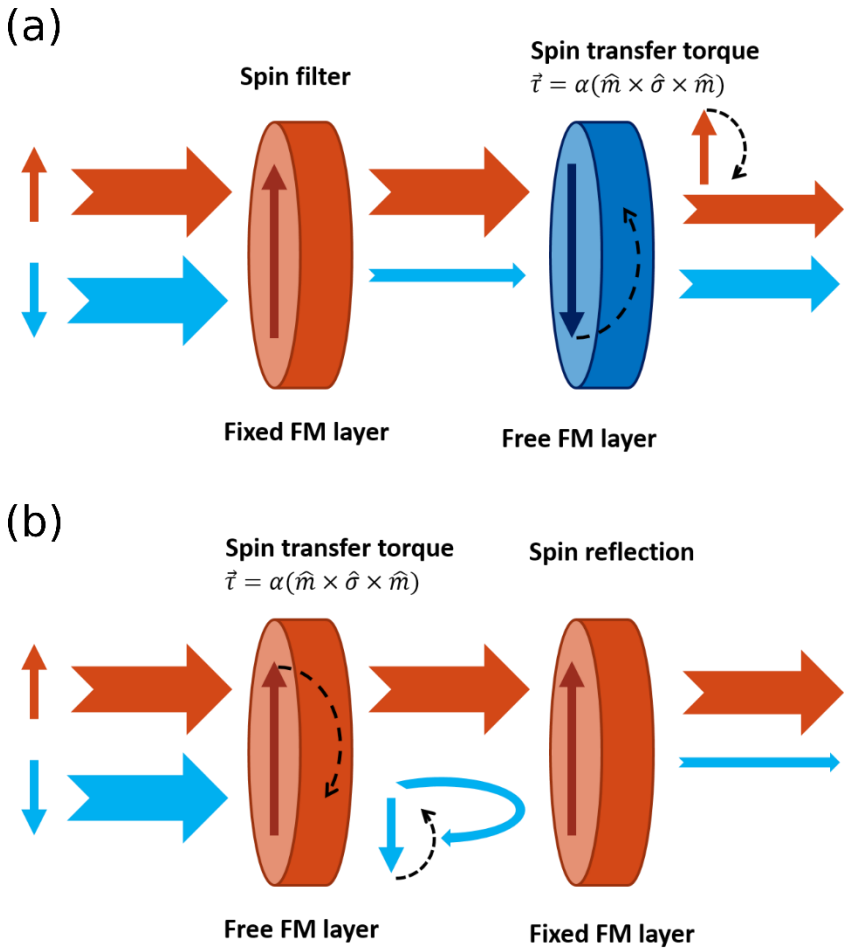

Figure 1.1: Illustration of the switching of MTJ by STT. (a) For AP to P transition, the STT by the majority spin current reverse the magnetization of the free layer. (b) For P to AP transition, the STT originates from the reflection at the fixed layer interface of the minority spin current.

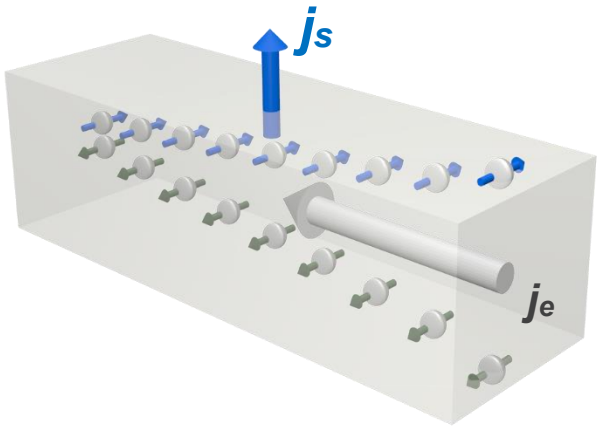

Figure 1.2: Illustration of the spin Hall effect in (extended) thin films. Due to spin-orbit interfaction, electrons with opposite spins deflect to different directions and build up opposite spin accumulations on the top and bottom surfaces.

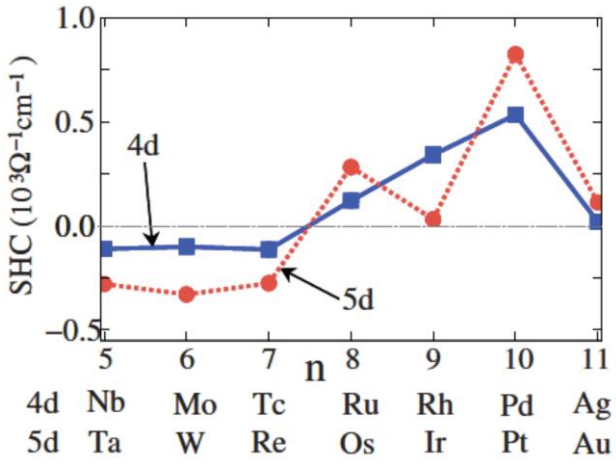

Figure 1.3: (Reproduced from Ref. [19]) Intrinsic spin Hall conductivity of 4d and 5d elements, calculated by tight-binding model.

Although the experimentally estimated values of the SHA of Ta and W are quite consistent across many different measurements, that of Pt has been controversial, ranging from 0.02 [24,25] to 0.2 [15,26,27]. Those discrepancies in Pt SHA values led to the scrutiny of various spin torque probing techniques and the associated analyses, as discussed in Ref. [28]. Part of the inconsistency of the measured SHA is due the interfacial spin transparency at the NM/FM interface, as suggested by the semiclassical spin-drift diffusion model [29,30]. Based on this model, the (damping-like) spin torque efficiency, defined as the ratio of the SHE-induced spin current density flowing into the FM layer and the electrical current density in the NM layer, is related to the internal SHA of the NM layer by the interfacial transparency as [29,30]:

$$\xi_{\mathrm{DL}} \equiv \frac{2e}{\hbar} \cdot \frac{j_s^{\mathrm{FM}}}{j_e^{\mathrm{NM}}} = \theta_{\mathrm{SH}} \cdot T_{\mathrm{int}} \approx \theta_{\mathrm{SH}} \left(1 + \frac{1}{2\lambda_s \rho_{\mathrm{NM}} G_r} \right)^{-1} \tag{1.2}$$

where T_{int} is the interfacial spin transparency, λ_s and ρ_{NM} are the spin diffusion length and resistivity of the NM layer (assumed to be uniform), G_r is the real part of the spin mixing conductance of the interface $G^{\uparrow\downarrow} = G_r + iG_i$. Here we assume that the NM thickness is much larger than λ_s. The spin transmission at the interface causes the experimentally observed "effective SHA" (or spin torque efficiency), which is derived from the dynamics of the FM magnetization under the effect of SHE-induced spin torques, to depend on the particular NM/FM interface, as reported in Refs. [26,27]. The value of the spin mixing conductance can be theoretically calculated or experimentally estimated by the measurement of Gilbert magnetic damping constant as shown in chapter 4.

Another crucial reason for the controversy regarding the SHA of Pt is that its value is not necessarily invariant for a particular element. Theories suggest that the relation of the SHA and the resistivity of the NM layer is determined by the combination of different SHE mechanisms, as

discussed in the next section. Note that the estimated values of SHA for β-Ta and β-W are in good agreement across different measurements due to their high and rather stable resistivity so that the effect of interfacial transparency and SHE mechanism are minimal, since $2\lambda_s\rho_{NM}G_r \gg 1$. On the contrary, due to its relatively lower resistivity, the SHA value of Pt is sensitive to impurity and surface scatterings, especially when the Pt film is thin, comparable to its spin diffusion length. Therefore, it is important to understand the dominant SHE mechanism(s) in Pt.

1.2. Possible mechanisms of SHE

The SHE in nonmagnetic metals is phenomenologically similar to the extraordinary/anomalous Hall effect (AHE) in FM, except for the lack/existence of an internal magnetization. Thus it is natural to categorize the possible mechanisms of SHE into 2 general types, similar to those of AHE [20,31]: the intrinsic SHE which is due to the band structure of the material, and the extrinsic SHE which is due to the spin-orbit coupling at scattering events. The extrinsic SHE is further divided into spin skew scattering and side-jump mechanisms. Experimentally, these 3 mechanisms can be distinguished by their relative strength and dependence on the purity of the materials.

In the intrinsic SHE, the spin-dependent transverse velocities originate from the effect of spin-orbit coupling on the electronic band structure between scattering events. The spin Hall conductivity (SHC) $\sigma_{xy}^{s_z}$ can be expressed in terms of the Berry curvature Ω_n^z as

$$\sigma_{xy}^{s_z} = \frac{e}{\hbar}\sum_k \Omega^z(k) = \frac{e}{\hbar}\sum_k\sum_n f_{kn}\Omega_n^z(k) \qquad (1.3)$$

where f_{kn} is the Fermi distribution function of the n-th band at k. Since the spin Hall conductivity is proportional to the transverse velocity of spin carriers which is generated between momentum scattering events, it is independent of the momentum relaxation time τ. Thus the spin Hall angle

$$\theta_{\mathrm{SH}} = \frac{2e}{\hbar}\frac{\sigma_{xy}^s}{\sigma_{xx}^c} \qquad (1.4)$$

is inversely proportional to the electrical conductivity σ_{xx}^c.

In the spin skew scattering mechanism, during momentum scattering events, electrons of different spin directions experience different effective magnetic field gradients due to strong spin-orbit coupling. Spin-dependent transverse velocities are consequently induced, thus give a net transverse spin current. Since the spin skew scattering is associated with momentum scattering which generates both longitudinal velocity for charge carriers and transverse net velocity for spins,

the spin Hall conductivity is proportional to the electrical conductivity. Thus, the spin Hall angle, defined by equation (1.4), is independent of electrical conductivity.

Side-jump occurs due to the spin-dependent different acceleration and deceleration during momentum scattering events which results in an effective transverse displacement. Under an applied electric field $\boldsymbol{E}$, the momentum just before the collisions is $\boldsymbol{k} = e\boldsymbol{E}\tau$. Since the average spin drift due to side-jump is proportional to the momentum transfer $\Delta\boldsymbol{k}$ during the collision, the spin drift velocity is independent of τ. Thus, similar to the intrinsic SHE, the spin Hall conductivity due to side-jump scattering is independent of the electrical conductivity. Consequently, the spin Hall angle is inversely proportional to the electrical conductivity.

In Pt, the side-jump contribution has been theoretically evaluated to be much smaller than the intrinsic one [32]. Thus, the remaining challenge is to evaluate the relative strengths of the intrinsic and skew scattering mechanisms. A straightforward electrical strategy is to measure SHC with varying electrical conductivity. This can be done by changing the temperature, as demonstrated in Refs. [21,24] which supports the dominance of intrinsic SHE in Pt. One counter argument to the quantitative results of this method is that the SHC varies with the relative position of the Fermi level and the Berry curvature which may be temperature dependent [33].

In chapter 2, I will be discussing the second method to experimentally confirm the intrinsic SHE in Pt which is to vary the electrical conductivity of Pt thin films by surface scattering [34]. The thickness dependence of the DL spin torque efficiency of Pt indicates the constant value of SHC, not spin Hall angle.

The identification of the dominant SHE mechanism in Pt has an important technological implication, that is the spin Hall angle $\theta_{SH} = \sigma_{SH} \cdot \rho$ of Pt can be enhanced by increasing its electrical resistivity ρ. For a given critical spin torque for switching, the dissipation energy scales

with $\rho / \theta_{SH}^2 = 1/(\sigma_{SH}^2 \cdot \rho)$, thus increasing ρ without detrimental effect on σ_{SH} reduces the power consumption. This idea is investigated in perpendicularly magnetized Pt/Co samples in Chapter 3, in which Al and Hf impurities are doped into Pt to increase the bulk resistivity, and its application in switching devices is demonstrated in chapter 6.

1.3. Three-terminal MTJ structure powered by the giant SHE

The giant SHE in certain nonmagnetic metals, such as Pt, Ta and W, provides an effective way to generate a transverse spin current from an electrical one. This opens up new opportunities for magnetic-spintronic applications, such as spin-torque driven magnetic nano-oscillators [35], current driven domain wall motion [36], magnetic skyrmions [37] and magnetic tunnel junctions (MTJs) [17]. In chapters 4 – 6, the SHE in Pt is utilized to drive the magnetization of the three-terminal MTJ (3T-MTJ) structure which is a promising candidate for magneto-resistive random access memory (MRAM) applications.

The most common, and already commercialized, type of MRAM devices is the 2-terminal MTJ (2T-MTJ) structure in which a thin, 1 – 2 nm, insulating tunnel barrier (commonly MgO) is sandwiched between two FM layers whose magnetizations are in-plane (IP-MTJ) or perpendicular (pMTJ) to the film plane. The magnetization of one FM layer (reference layer) is fixed (or "pinned") and that of the other layer (free layer) can be flipped parallel (P) or anti-parallel (AP) to the fixed one, either by an external field along the easy axis, or by spin-transfer torque (STT-MTJ) by a current flowing through the MTJ. The tunneling magnetoresistance (TMR) of the MTJ is defined as

$$\mathrm{TMR} \equiv \frac{R_{\mathrm{AP}} - R_{\mathrm{P}}}{R_{\mathrm{P}}} \cdot 100\% \qquad (1.5)$$

where $R_{\mathrm{P}} < R_{\mathrm{AP}}$ are the MTJ resistance in P and AP states. For effective and fast readout, the higher TMR the better. Another figure of merit is the thermal stability factor $\Delta = E_g/k_B T$ which is the ratio of the energy barrier E_g between the P and AP states and the thermal fluctuation $k_B T$ (k_B is the Boltzman constant and T is the temperature). Depending of the size of the particular memory cell, the data retention of 10 years requires a minimum value of Δ to be 40 – 60.

The 2-terminal STT-MTJ structure offers many advantanges over other contemporary

candidates for memory technology, as listed in Table 1.1 (reproduced from Ref. [38]). Owing to its nonvolatility, it has low standby power which is critical for mobile applications. It can also be faster than most non-volatile memory types. However, it has several shortcomings which are inherent to its 2-terminal structure in which the write and read lines share the same path through the MTJ tunnel barrier. First, there is an upper limit of writing current flowing through the MTJ until the breakdown of the tunnel barrier. This also sets minimum limits on the write/bit-error-rates and switching time. Furthermore, the writing critical current needs to be high enough above the reading current to avoid the read-disturb-errors that occur when the reading current unwantedly alters the state of the MTJ. Thus this configuration imposes strict restrictions on device optimization. Another critical drawback of the MTJ structure is the "incubation delay" which hinders the fast switching of the devices. This delay refers to the time the magnetization of the free layer needs to gain sufficient initial torque from the thermal fluctuation to be effectively driven by the spin torques.

Soon after the discovery of the giant SHE in NM metals, a new class of MRAM was proposed. This 3-terminal (3T-MTJ) structure has an MTJ on top of a channel made from a strong SHE material such as Pt [15], Ta [17] or W [18], as schematically illustrated in Fig. 1.4. The device is read by the same way as the 2-terminal counterpart, but is written/switched by the spin torques induced from the electrical current flowing in the channel by the SHE. By separating the read and write paths, the 3T-MTJ structure avoids the breakdown of the tunnel barrier and the read-disturb-errors, allows flexibility in optimization. Furthermore, it has been recently demonstrated experimentally [39] and by micromagnetic simulations [40] that the 3T-MTJ devices can switch very fast, ~1 ns, below the "incubation delay" mentioned above. The fast switching of the 3T-MTJ devices is attributed to the role of the Oersted field (generated by the writing current) and/or any

SHE-induced field-like effects in the evolution and reversal of magnetic domains in the FM free layer [40]. Thus this structure promises a solution for power efficient and fast memories in which device density is not a critical factor.

In chapter 4 and chapter 6, I will be discussing our efforts to reduce the critical current density and power consumption of 3T-MTJ devices by using a thin Hf spacer between the MTJ and the channel to reduce the magnetic damping (chapter 4), and by using $Pt_{85}Hf_{15}$ alloy for channel to obtain higher spin torque efficiency (chapter 6). Another attractive property of the 3T-MTJ structure is the consistent performance at low, cryogenic temperatures which is demanded in superconducting computers. The performance of 3T-MTJ devices at a low temperature of 3.1 K, as well as its integration with superconducting logic devices, is discussed in chapter 5.

Table 1.1: Comparison of key features of existing and emerging memories. Reproduced from Ref. [38].

	SRAM	**eDRAM**	**DRAM**	**eFlash (NOR)**	**Flash (NAND)**	**FeRAM**	**PCM**	**ReRAM**	**STT-MRAM**
Endurance (cycles)	Unlimited	Unlimited	Unlimited	10^5	10^5	10^{14}	10^9	10^9	Unlimited
Read/write access time (ns)	< 1	1 - 2	30	10 / 10^3	100 / 10^6	30	10 / 100	1 - 100	2 - 30
Density	Low	Medium	Medium	Medium	High	Low	High	High	Medium
Write power	Medium	Medium	Medium	High	High	Medium	Medium	Medium	Medium
Standby power	High	Medium	Medium	Low	Low	Low	Low	Low	Low
Other	Volatile	Volatile. Refresh.	Volatile. Refresh.	High voltage	High voltage	Destructive readout	Operating < 125C	Complex mechanism	Low read signal

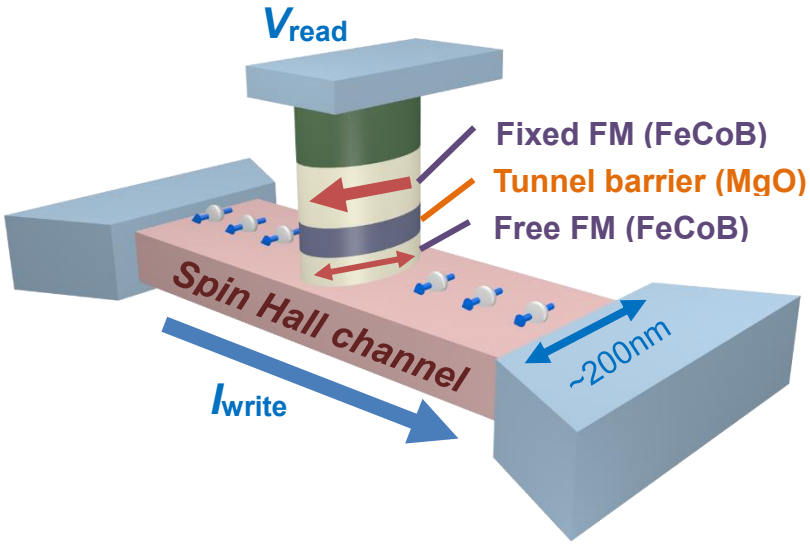

Figure 1.4: Basic structure of the 3T-MTJ devices. The spin current induced by the SHE in the channel flows transversely into the free layer and switches its magnetization via the spin transfer torque. The state of the MTJ is determined by reading the drop voltage while flowing a small current throught the MTJ.

1.4. Quantitative determination of SHE-induced spin torques

The debate on the inconsistent values of the SHA of Pt is largely associated with the methods to quantify the strength of the SHE-induced spin torques in multilayers and their analyses. A comprehensive review of the issue can be found in Ref. [28]. Along with our understanding of the SHE and magnetic and spin dynamics in multilayers, more accurate quantitative methods have been propsed and widely employed [8,14,16,17,41–44]. This section introduces three common methods that are used in later chapters: the spin-torque ferromagnetic resonance (ST-FMR), the switching measurement of in-plane 3T-MTJ structure and the harmonic response technique.

In ST-FMR measurements [8], the Oersted field and the SHE-induced anti-damping torque generated from an electrical current in the NM layer of an in-plane magnetized NM/FM bilayer modify the FMR lineshape as

$$\mathrm{V}_{\mathrm{mix}} = S \cdot F_S(H_{\mathrm{ext}}) + A \cdot F_A(H_{\mathrm{ext}}) \tag{1.6}$$

where

$$F_S(H_{\mathrm{ext}}) = \frac{\Delta^2}{\Delta^2 + (H_{\mathrm{ext}} - H_0)^2},\ F_A(H_{\mathrm{ext}}) = \frac{\Delta \cdot (H_{\mathrm{ext}} - H_0)}{\Delta^2 + (H_{\mathrm{ext}} - H_0)^2}, \tag{1.7}$$

S and A are constants whose ratio is given by

$$\frac{S}{A} = \xi_{\mathrm{FMR}} \frac{\hbar}{e\mu_0 M_s t_{\mathrm{FM}} t_{\mathrm{NM}}} \cdot \frac{1}{\sqrt{1 + M_{\mathrm{eff}} / H_{\mathrm{ext}}}}. \tag{1.8}$$

Here H_{ext} is the (sweeping) external field applied at 45° to the easy axis of the sample, H_0 the resonance field, Δ the linewidth, ξ_{FMR} the (damping-like) spin torque efficiency, μ_0 the vacuum permeability, M_s the FM saturation magnetization, M_{eff} the effective field and t the layer thickness. In this configuration, the SHE-induced anti-damping torque (Oersted field) is responsible for the symmetric F_S (anti-symmetric F_A) part of the FMR lineshape. By fitting the FMR lineshape to equation (1.7), we can extract their contributions S and A from whose ratio the spin torque

efficiency can be determined by equation (1.8). Note that M_{eff} and the Gilbert magnetic damping α can be readily determined from the frequency-dependent ST-FMT measurements as

$$f = \frac{\gamma}{2\pi}\sqrt{H_0(H_0 + M_{\text{eff}})} \tag{1.9}$$

and

$$\Delta = f \cdot \alpha \cdot 2\pi / \gamma \tag{1.10}$$

where γ is the gyromagnetic ratio. Thus, the ST-FMR method gives a simple and quick determination of many important parameters. However, the current analysis ignores the field-like effect of the SHE which causes errors in the estimated value of the damping-like torque [27]. The estimation of other parameters is unaffected by the field-like torque and therefore is used in chapter 4. Since the SHE-induced field-like torque has no effect on the estimation of the parameter *S* in equation (1.6) but on the parameter *A*, a remedy to this problem is to carefully calibrate the amount of the microwave current flowing in the spin Hall material. This allows a more accurate estimation of *A*, as demonstrated in the study of topological insulator / FM bilayers [45].

Another method to quantifying the DL spin torque in in-plane multilayers is the measurement of DC current switching of 3T-MTJ devices with in-plane magnetic anisotropy. As discussed above, the DC current switching of 3T-MTJ devices is thermally activated, therefore a current ramp-rate measurement, in which the critical currents at different current sweeping rates are determined, needs to be performed to obtain the critical current density J_0 at zero thermal fluctuation, as described in Ref. [46]. The DL spin torque efficiency is then calculated as [47]

$$\xi_{\text{DL}} = \frac{2e}{\hbar}\mu_0 M_s t_{\text{FM}} \alpha \left(H_c + M_{\text{eff}}/2\right)/J_0, \tag{1.11}$$

where H_c is the coercive field of the FM free layer. Note that the model, which is originally developed for the 2-terminal MTJ structure, ignores the field-like effects induced by the Oersted

field from the channel current and/or by the SHE in the 3T-MTJ structure which can play an important role in the switching mechanism [40].

While the above techniques were developed for in-plane magnetized bilayers, the AC harmonic response technique by Kim and Hayashi *et al.* was initially established for perpendicularly magnetized anisotropy (PMA) samples [41] and later extended for in-plane ones [44]. The basic idea is to apply an AC current through the bilayer to excite the AC response of the magnetization which results in an oscillating resistance due to certain anisotropy magnetoresistance (AMR) effects. The Hall voltage, which is the product of an AC current and resistance of the same frequency, exhibits second-harmonic response to the excitation current. For small oscillation of the magnetization around the normal of the plane, the SHE-induced damping-like (DL) and field-like (FL) spin torques $\xi_{\mathrm{DL,FL}}$ can be modeled as (oscillating) longitudinal and transverse effective fieldsv $\Delta H_{\mathrm{L,T}}$, respectively, as

$$\xi_{\mathrm{DL(FL)}} = \frac{2e}{\hbar}\mu_0 M_s t_{\mathrm{FM}} \cdot \Delta H_{\mathrm{L(T)}} / j_e \tag{1.12}$$

where j_e is the electrical current density in the NM layer. From the formulism described in Ref. [41], the two effective fields can be determined by taking the ratio of the slope of the second-harmonic Hall voltage versus the longitudinal and transverse applied fields $H_{\mathrm{L,T}}$ and the curvature of the first-harmonic Hall voltage versus $H_{\mathrm{L,T}}$ (determined by the PMA anisotropy field) as given by:

$$\Delta H_{\mathrm{L(T)}} = -2\frac{\partial V_{2\varpi}}{\partial H_{\mathrm{L(T)}}} \Big/ \frac{\partial^2 V_{\varpi}}{\partial H_{\mathrm{L(T)}}^2}. \tag{1.13}$$

Note that for simplicity we ignore the contribution of the planar Hall effect which is expected to be much smaller than the anomalous Hall effect in most NM/FM structures. This method, if expected to be valid, gives the estimation for both DL and FL spin torque efficiencies which are

not fully quantified in the previously mentioned methods. However, the equation (1.13) is based on the assumption that the Hall voltage arises solely from the anomalous Hall effect. In the presence of the AMR-induced planar Hall effect, which is relatively small in many systems including Pt/Co bilayers, a correction to equation (1.13) is needed [44]. It is also shown that the spin Hall magnetoresistance in metallic bilayers [48] due to the reflection of the spin current at the interface may cause non-linear contribution to the Hall signals [30]. Additionally, the contribution of the unidirectional spin Hall magnetoresistance, observed in Ta/Co and Pt/Co systems [49], to the Hall signals is still unclear. Therefore, the accuracy of this method requires more experimental and theoretical studies on those magnetoresistance effects which is out of the scope of this dissertation.

REFERENCES

[1] J. C. Slonczewski, J. Magn. Magn. Mater. **159**, L1 (1996).

[2] L. Berger, Phys. Rev. B **54**, 9353 (1996).

[3] M. Stiles and A. Zangwill, Phys. Rev. B **66**, 014407 (2002).

[4] D. C. Ralph and M. D. Stiles, J. Magn. Magn. Mater. **320**, 1190 (2008).

[5] D. D. Tang and Y.-J. Lee, *Magnetic Memory - Fundamentals and Technology* (Cambridge University Press, 2010).

[6] I. Mihai Miron, G. Gaudin, S. Auffret, B. Rodmacq, A. Schuhl, S. Pizzini, J. Vogel, and P. Gambardella, Nat. Mater. **9**, 230 (2010).

[7] Y. A. Bychkov and E. I. Rashba, JETP Lett. **39**, 78 (1984).

[8] L. Liu, T. Moriyama, D. C. Ralph, and R. A. Buhrman, Phys. Rev. Lett. **106**, 036601 (2011).

[9] L. Liu, O. J. Lee, T. J. Gudmundsen, D. C. Ralph, and R. A. Buhrman, Phys. Rev. Lett. **109**, 096602 (2012).

[10] M. I. Dyakonov and V. I. Perel, Phys. Leters **35A**, 459 (1971).

[11] J. Hirsch, Phys. Rev. Lett. **83**, 1834 (1999).

[12] S. Zhang, Phys. Rev. Lett. **85**, 393 (2000).

[13] C.-F. Pai, M.-H. Nguyen, C. Belvin, L. H. Vilela-leão, D. C. Ralph, and R. A. Buhrman, Appl. Phys. Lett. **104**, 082407 (2014).

[14] L. Liu, C.-T. Chen, and J. Z. Sun, Nat. Phys. **10**, 561 (2014).

[15] M.-H. Nguyen, C.-F. Pai, K. X. Nguyen, D. A. Muller, D. C. Ralph, and R. A. Buhrman, Appl. Phys. Lett. **106**, 222402 (2015).

[16] C. F. Pai, M. Mann, A. J. Tan, and G. S. D. Beach, Phys. Rev. B **93**, 144409 (2016).

[17] L. Liu, C.-F. Pai, Y. Li, H. W. Tseng, D. C. Ralph, and R. A. Buhrman, Science **336**, 555 (2012).

[18] C.-F. Pai, L. Liu, Y. Li, H. W. Tseng, D. C. Ralph, and R. A. Buhrman, Appl. Phys. Lett. **101**, 122404 (2012).

[19] T. Tanaka, H. Kontani, M. Naito, T. Naito, D. Hirashima, K. Yamada, and J. Inoue, Phys. Rev. B **77**, 165117 (2008).

[20] A. Hoffmann, IEEE Trans. Magn. **49**, 5172 (2013).

[21] M. Isasa, E. Villamor, L. E. Hueso, M. Gradhand, and F. Casanova, Phys. Rev. B **91**, 024402 (2015).

[22] K. Ando, S. Takahashi, K. Harii, K. Sasage, J. Ieda, S. Maekawa, and E. Saitoh, Phys. Rev. Lett. **101**, 036601 (2008).

[23] L. Wang, R. J. H. Wesselink, Y. Liu, Z. Yuan, K. Xia, and P. J. Kelly, Phys. Rev. Lett. **116**, 196602 (2016).

[24] M. Morota, Y. Niimi, K. Ohnishi, D. H. Wei, T. Tanaka, H. Kontani, T. Kimura, and Y. Otani, Phys. Rev. B **83**, 174405 (2011).

[25] Y. Niimi, H. Suzuki, Y. Kawanishi, Y. Omori, T. Valet, A. Fert, and Y. Otani, Phys. Rev. B **89**, 054401 (2014).

[26] W. Zhang, W. Han, X. Jiang, S.-H. Yang, and S. S. P. Parkin, Nat. Phys. **11**, 496 (2015).

[27] C.-F. Pai, Y. Ou, L. H. Vilela-Leão, D. C. Ralph, and R. A. Buhrman, Phys. Rev. B **92**, 064426 (2015).

[28] L. Liu, R. A. Buhrman, and D. C. Ralph, arXiv:**1111**.3702 (2011).

[29] P. M. Haney, H.-W. Lee, K.-J. Lee, A. Manchon, and M. D. Stiles, Phys. Rev. B **87**, 174411 (2013).

[30] Y.-T. Chen, S. Takahashi, H. Nakayama, M. Althammer, S. Goennenwein, E. Saitoh, and G. Bauer, Phys. Rev. B **87**, 144411 (2013).

[31] G. Vignale, J. Supercond. Nov. Magn. **23**, 3 (2010).

[32] S. Lowitzer, M. Gradhand, D. Kodderitzsch, D. V. Fedorov, I. Mertig, and H. Ebert, Phys. Rev. Lett. **106**, 056601 (2011).

[33] G. Guo, S. Murakami, T.-W. Chen, and N. Nagaosa, Phys. Rev. Lett. **100**, 096401 (2008).

[34] F. Warkusz, Electrocompon. Sci. Technol. **5**, 99 (1978).

[35] L. Liu, C.-F. Pai, D. C. Ralph, and R. A. Buhrman, Phys. Rev. Lett. **109**, 186602 (2012).

[36] S. Emori, U. Bauer, S.-M. Ahn, E. Martinez, and G. S. D. Beach, Nat. Mater. **12**, 611 (2013).

[37] W. Jiang, P. Upadhyaya, W. Zhang, G. Yu, M. B. Jungfleisch, F. Y. Fradin, J. E. Pearson, Y. Tserkovnyak, K. L. Wang, O. Heinonen, S. G. E. te Velthuis, and A. Hoffmann, Science **349**, 283 (2015).

[38] A. D. Kent and D. C. Worledge, Nat. Nanotech. **10**, 187 (2015).

[39] S. V. Aradhya, G. E. Rowlands, J. Oh, D. C. Ralph, and R. A. Buhrman, Nano Lett. **16**, 5987 (2016).

[40] G. E. Rowlands, S. V. Aradhya, S. Shi, E. H. Yandel, J. Oh, D. C. Ralph, and R. A. Buhrman, Appl. Phys. Lett. **110**, 122402 (2017).

[41] J. Kim, J. Sinha, M. Hayashi, M. Yamanouchi, S. Fukami, T. Suzuki, S. Mitani, and H. Ohno, Nat. Mater. **12**, 240 (2013).

[42] K. Garello, I. M. Miron, C. O. Avci, F. Freimuth, Y. Mokrousov, S. Blügel, S. Auffret, O. Boulle, G. Gaudin, and P. Gambardella, Nat. Nanotech. **8**, 587 (2013).

[43] X. Fan, H. Celik, J. Wu, C. Ni, K.-J. Lee, V. O. Lorenz, and J. Q. Xiao, Nat. Commun. **5**,

3042 (2014).

[44] M. Hayashi, J. Kim, M. Yamanouchi, and H. Ohno, Phys. Rev. B **89**, 144425 (2014).

[45] A. R. Mellnik, J. S. Lee, A. Richardella, J. L. Grab, P. J. Mintun, M. H. Fischer, A. Vaezi, A. Manchon, E.-A. Kim, N. Samarth, and D. C. Ralph, Nature **511**, 449 (2014).

[46] E. B. Myers, F. J. Albert, J. C. Sankey, E. Bonet, R. A. Buhrman, and D. C. Ralph, Phys. Rev. Lett. **89**, 196801 (2002).

[47] J. Z. Sun, Phys. Rev. B **62**, 570 (2000).

[48] J. Kim, P. Sheng, S. Takahashi, S. Mitani, and M. Hayashi, Phys. Rev. Lett. **116**, 097201 (2015).

[49] C. O. Avci, K. Garello, A. Ghosh, M. Gabureac, S. F. Alvarado, and P. Gambardella, Nat. Phys. **11**, 570 (2015).

CHAPTER 2

Spin torque study of the spin Hall conductivity and spin diffusion length in platinum thin films with varying resistivity

Minh-Hai Nguyen[1], D. C. Ralph[1,2], R. A. Buhrman[1]

[1]*Cornell University, Ithaca, New York 14853, USA*

[2]*Kavli Institute at Cornell, Ithaca, New York 14853, USA*

(Published: Physical Review Letters **116**, 126601 on 24 March 2016)

ABSTRACT

We report measurements of the spin torque efficiencies in perpendicularly-magnetized Pt/Co bilayers where the Pt resistivity ρ_{Pt} is strongly dependent on thickness t_{Pt}. The damping-like spin Hall torque efficiency per unit current density, ξ^j_{DL}, varies significantly with t_{Pt}, exhibiting a peak value $\xi^j_{DL} = 0.12$ at t_{Pt} = 2.8 - 3.9 nm. In contrast, ξ^j_{DL} / ρ_{Pt} increases monotonically with t_{Pt} and saturates for t_{Pt} > 5 nm, consistent with an intrinsic spin Hall effect mechanism, in which ξ^j_{DL} is enhanced by an increase in ρ_{Pt}. Assuming the Elliott-Yafet spin scattering mechanism dominates we estimate that the spin diffusion length $\lambda_s = (0.77 \pm 0.08) \times 10^{-15}\ \Omega m^2 / \rho_{Pt}$.

MAIN TEXT

The spin Hall effect (SHE) [1–3], in which a transverse spin current density j_{SHE} is induced by a longitudinal charge current density j_e and whose strength is characterized by the spin Hall angle $\theta_{\mathrm{SH}} \equiv (2e/\hbar) j_{\mathrm{SHE}} / j_e$, has recently drawn much attention because of its promise for spintronics applications [4–13]. Mechanisms which might give rise to the SHE [14,15] include the intrinsic SHE [1,16], side-jump scattering [17] and skew scattering [18]. Two common methods to quantify the strength of the SHE are to employ ferromagnet/normal metal (FM/NM) bilayers and either (1) detect the spin transfer torque that the SHE-induced spin current from the NM layer exerts on the magnetization of the adjacent FM layer [19,20], or (2) use spin pumping to inject a spin current from the FM to the NM and detect the electric current in the NM layer that is induced by the inverse SHE (ISHE) [21–23]. In the former case due to spin backflow (SBF) at the FM/NM interface [24,25] and/or enhanced spin scattering at the interface (spin memory loss or SML) [26], only a portion $j_s^{\mathrm{NM|FM}}$ of the SHE-induced spin current j_{SHE} is absorbed in the FM layer, and that reduces the damping-like (DL) spin Hall (SH) torque efficiency per unit current density $\xi_{\mathrm{DL}}^{j} \equiv (2e/\hbar) j_s^{\mathrm{NM|FM}} / j_e = T_{\mathrm{int}} \theta_{\mathrm{SH}}$ to be less than θ_{SH}, where $T_{\mathrm{int}} = j_s^{\mathrm{NM|FM}} / j_{\mathrm{SHE}}$ (<1) is the interfacial spin transparency. SBF and/or SML can similarly reduce the strength of spin-pumping/ISHE signals.

Large values of ξ_{DL}^{j} have been reported for Pt [19,27–31], beta-Ta [19] and beta-W [4]. Special attention has been paid to Pt because its relatively low resistivity compared to the other SH materials would be beneficial for reducing Ohmic losses in applications. Values of ξ_{DL}^{j} for Pt have been reported spanning the range 0.06 - 0.12 [19,27–29], depending on the FM/Pt interface [31], and are usually accompanied by a relatively small field-like (FL) torque efficiency

whose magnitude and sign vary with the interface, FM magnetic anisotropy and temperature [29,32–36]. From an analysis of SBF based on a spin diffusion model [24,25], these ξ_{DL}^{j} results indicate that the underlying internal value of θ_{SH} for Pt is ~ 0.2 or even larger [28,29,31]. However, the determination of θ_{SH} from ξ_{DL}^{j} using the spin diffusion model requires an accurate value of the spin diffusion length λ_s, and in the case of Pt that value has long been controversial. Measurements by different techniques, at low and room temperatures, have reported a wide range, 1 - 11 nm, for λ_s in Pt [21–23,37–48]. Those measurements will be reviewed along with our analysis later in this Letter.

Here we report that ξ_{DL}^{j} has a strong, unexpected dependence on Pt thin film thickness t_{Pt} in perpendicularly-magnetized Pt/Co bilayers, as measured by the harmonic response (HR) technique [20,29]. In particular we report that ξ_{DL}^{j} exhibits a peak at $t_{Pt} = 2.8 - 3.9$ nm and gradually decreases at larger Pt thickness. This behavior is counter to the common expectation, reported in prior experiments with different layer structures [38,40,45], that ξ_{DL}^{j} should simply increase and saturate at a maximum value as t_{Pt} exceeds the spin diffusion length λ_s in Pt. Our interpretation of our result is that the spin Hall angle is linearly dependent on the Pt resistivity ρ_{Pt}, which in turn varies approximately inversely with t_{Pt} in our samples in the thin Pt limit, $t_{Pt} \leq 4$ nm, due to strong diffusive scattering at the Pt interface(s). We observe that the spin-torque efficiency *per unit applied electric field* $\xi_{DL}^{E} = \xi_{DL}^{j} / \rho_{Pt}$ increases monotonically with t_{Pt} and saturates at $t_{Pt} \approx 5$ nm. This is consistent with a spin Hall conductivity σ_{SH} that is independent of ρ_{Pt}, which indicates that the intrinsic SHE (and/or side-jump scattering) determines the spin Hall angle in our Pt films. The variation of ξ_{DL}^{E} with t_{Pt} is consistent with an *effective* $\lambda_s^{eff} = 2.0 \pm 0.1$ nm, but this

determination neglects the fact that spin relaxation in Pt is predicted to be dominated by the Elliott-Yafet (E-Y) mechanism [49,50], so that λ_s should scale linearly with $1/\rho_{\mathrm{Pt}}$ and therefore the spin diffusion length should depend on t_{Pt} in our samples, as well. We find that an analysis that assumes that $\lambda_s\rho_{\mathrm{Pt}}$ is a constant in our bilayer samples fits the experimental results well, and from the fit we obtain $\lambda_s\rho_{\mathrm{Pt}} = (0.77 \pm 0.08)\times 10^{-15}\ \Omega\cdot\mathrm{m}^2$. As discussed below, taking into account that λ_s should scale $\mu\ 1/r_{\mathrm{Pt}}$ would appear to resolve a prolonged controversy regarding the values of λ_s obtained from various SHE and ISHE experiments.

We studied multilayer samples consisting of *substrate* | Ta(1) | Pt(t_{Pt}) | Co(1) | MgO(2) | Ta(1) (numbers in parentheses are thicknesses in nm) grown on oxidized Si substrates by sputter-deposition in a vacuum of $<1.0\times10^{-7}$ Torr. The Ta(1) seeding layer resulted in a smoother multilayer [51] and enhanced perpendicular magnetic anisotropy (PMA) of the Co. The Pt thickness t_{Pt}, as averaged over the sample area, was varied in fine steps from 1.2 nm to 15 nm with a relative uncertainty of about 5%. This series of samples exhibit PMA with coercivity of ≈ 0.4 T without post-deposition annealing. The saturation magnetization is $M_s = (1.08 \pm 0.05)\times 10^6$ A/m with an apparent "magnetic dead layer" of $t_{\mathrm{FM}}^{\mathrm{dead}} = 0.26 \pm 0.04$ nm [29]. For the HR measurements, the multilayer stacks were patterned into $5\ \mu\mathrm{m}\times 60\ \mu\mathrm{m}$ Hall bars by photolithography and ion milling. All measurements were carried out at room temperature (RT).

The sheet conductance of the films were determined by 4-probe resistance measurements of a set of microbars of varying width, length and probe spacing, which minimized errors due to sample geometry and reduced the statistical measurement error to below 1%. Thus the main source of error comes from the uncertainty of film thicknesses. The resistivity of Pt layer ρ_{Pt} was determined by subtracting the sheet conductance of a separately fabricated Ta(1) | Co(1) | MgO(2)

| Ta(1) stack from that of our samples containing the Pt layer. In Fig. 2.1(a) we show ρ_{Pt} for the samples as a function of t_{Pt}. The sharp increase of ρ_{Pt} with decreasing t_{Pt} is a well-known phenomenon due to strong diffusive scattering at a Pt surface [48,52–56].

The DL and FL SH torque efficiencies of these PMA samples were measured by the HR technique [20,29] with the same alternating voltage amplitude (4 V) applied to the Hall bars in all measurements, corresponding to an alternating electric field of constant magnitude $E = 67$ kV/m. Fig. 2.1(b) shows the SH torque-induced longitudinal H_{L} (corresponding to DL torque) and transverse H_{T} (corresponding to FL torque) equivalent fields per unit applied electric field determined by the HR measurement as functions of t_{Pt}. As t_{Pt} increases, H_{L} quickly increases and then saturates for $t_{\mathrm{Pt}} > 5$ nm. H_{T} starts for t_{Pt} near zero from a value that is negative in our convention, opposite to the Oersted field generated by the charge current flow in the Pt, but quickly reaches a positive maximum and then decreases gradually. (We will discuss the details of our analysis of this H_{T} behavior elsewhere.) We determine the DL (FL) SH torque efficiencies *per unit applied current density* as

$$\xi^{j}_{\mathrm{DL(FL)}} = \frac{2e}{\hbar}\mu_0 M_s (t_{\mathrm{FM}} - t^{\mathrm{dead}}_{\mathrm{FM}}) \cdot H_{\mathrm{L(T)}} / j_e \qquad (2.1)$$

where $j_e = E / \rho_{\mathrm{Pt}}$. Fig. 2.1(c) shows the DL and FL torque efficiencies per unit current density as functions of t_{Pt}. ξ^{j}_{DL} first increases with t_{Pt} and reaches a maximum ≈ 0.12 at $t_{\mathrm{Pt}} = 2.8 - 3.9$ nm, but then, surprisingly, decreases gradually with t_{Pt}. The thickness dependence of ξ^{j}_{DL} that we observe is qualitatively similar to that observed in YIG/Pt bilayers [56] but quite different from other previous ferromagnetic resonance (FMR) measurements [38,40,44,45] and spin pumping/ISHE experiments [21–23] on metallic FM/Pt bilayers where the data typically are fit

by a simple functional form [37]:

$$\xi_{\mathrm{DL}}^{j}(t_{\mathrm{NM}}) = \frac{2e}{\hbar} T_{\mathrm{int}} j_s(t_{\mathrm{NM}}) / \, j_e(t_{\mathrm{NM}}) = \xi_{\mathrm{DL,max}}^{j} \left(1 - \mathrm{sech}(t_{\mathrm{NM}} / \lambda_{\mathrm{s}})\right). \qquad (2.2)$$

This is the behavior expected for an ideal (T_{int} =1) interface with no SBF, or alternatively one where SML is the dominant cause for T_{int} < 1. However, we emphasize that Eq. (2.2) holds only under the assumption of constant ρ_{NM} and hence thickness-independent values for q_{SH} and λ_{s}. In the intrinsic SHE regime, which has recently been reported to describe Pt [41,57], and also in the side-jump regime, it is the spin Hall conductivity σ_{SH} that is expected to be constant, independent of $\rho_{\mathrm{NM}}(t_{\mathrm{NM}})$ while the spin Hall angle $\theta_{\mathrm{SH}}(t_{\mathrm{NM}}) = (2e/\hbar)\sigma_{\mathrm{SH}}\rho_{\mathrm{NM}}(t_{\mathrm{NM}})$ should vary $\propto \rho_{\mathrm{NM}}(t_{\mathrm{NM}})$ and therefore ξ_{DL}^{j} also depends on the NM resistivity and hence, in this study, on its thickness due to strong interfacial scattering.

An alternative approach is to consider the spin torque efficiency *per unit applied electric field*, determined directly from the HR measurement as

$$\xi_{\mathrm{DL}}^{E} = \frac{2e}{\hbar} \mu_0 M_s (t_{\mathrm{FM}} - t_{\mathrm{FM}}^{\mathrm{dead}}) H_{\mathrm{L}} / E. \qquad (2.3)$$

The dependence of ξ_{DL}^{E} on Pt thickness is shown in Fig. 2.1(d) and is consistent with the functional form in Eq. (2.2) with a prefactor that does not depend on t_{Pt}, which indicates that the intrinsic SHE, or perhaps the side-jump mechanism, is indeed predominant in Pt. Then assuming that (i) the DL torque is entirely due to the SHE of the Pt, (ii) the interface is well ordered, and (iii) SBF is the dominant cause for T_{int} < 1, we can expect, approximately, [24,25]

$$\xi_{\mathrm{DL}}^{E}(t_{\mathrm{Pt}}) = \frac{2e}{\hbar} \sigma_{\mathrm{SH}} \left(1 - \mathrm{sech}(t_{\mathrm{Pt}} / \lambda_s)\right) \left(1 + \frac{\tanh(t_{\mathrm{Pt}} / \lambda_s)}{2\lambda_s \rho_{\mathrm{Pt}} G_r}\right)^{-1}, \qquad (2.4)$$

where G_r is the real part of the spin mixing conductance $G^{\uparrow\downarrow} = G_r + iG_i$ and we have assumed

$G_r \gg G_i$, consistent with our result that $\xi_{\mathrm{DL}} \gg \xi_{\mathrm{FL}}$. As an exercise, if we fit the ξ_{DL}^{E} data shown in Fig. 2.1(d) to equation (2.4) using a fixed value $\rho_{\mathrm{bulk}} = 15\,\mu\Omega\cdot\mathrm{cm}$, the resistivity in the midst of a thick Pt film, and $G_r = 0.59\times10^{15}\ \Omega^{-1}\mathrm{m}^{-2}$ as theoretically calculated for the Pt/Co interface [24], we obtain an "effective" spin diffusion length $\lambda_s^{\mathrm{eff}} = 2.0 \pm 0.1\,\mathrm{nm}$ and $\sigma_{\mathrm{SH}} = (10.5 \pm 0.3)\times10^{5}\,[\hbar/2e]\,\Omega^{-1}\cdot\mathrm{m}^{-1}$ or $\theta_{\mathrm{SH}} = \rho_{\mathrm{bulk}}\sigma_{\mathrm{SH}} = 0.16 \pm 0.01$, consistent with previous estimations [28,31]. The choice of G_r may change the estimation of σ_{SH} but has a very weak effect on λ_s^{eff}. The existence of a SML would introduce a constant factor < 1 to the right hand side of equation (2.4), thus would increase the estimated σ_{SH} but would not affect λ_s^{eff}. (We note that this analysis neglects any possible negative SHE from the 1 nm Ta layer (see the discussion in the Supplemental Information (SI).) We account for the maximum possible effect of any SH torque from the Ta underlayer within the experimental uncertainties indicated in Fig. 2.1(c,d)).

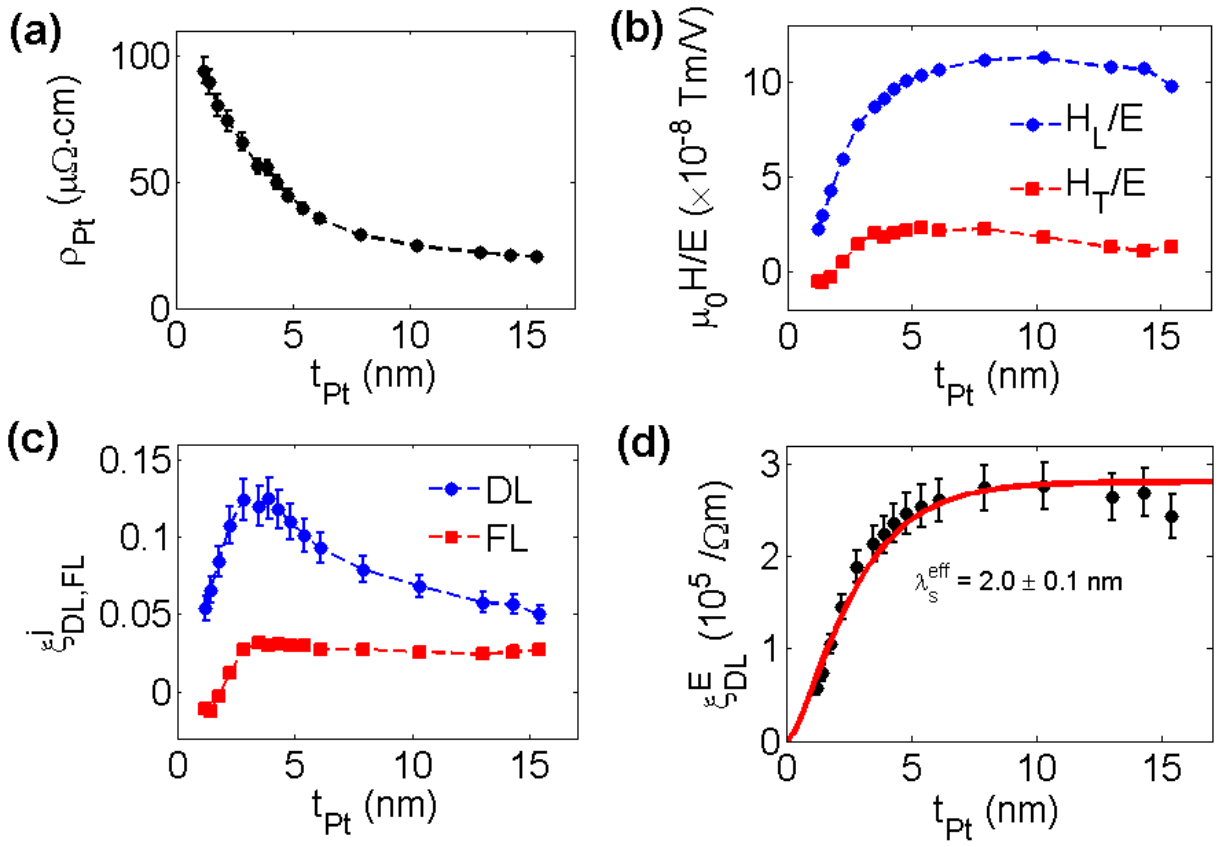

Figure 2.1: (a) Resistivity of Pt in Ta(1)/Pt/Co(1), **(b)** SH torque-induced longitudinal (circles) and transverse (squares) equivalent fields per unit applied electric field, **(c)** damping-like (circles) and field-like (squares) SH torque efficiency per unit applied current density, and **(d)** damping-like SH torque efficiency per unit applied electric field as functions of Pt thickness. The solid line in (d) shows the fitted result to equation (4) from which the *effective* spin diffusion length is estimated to be $\lambda_s^{\text{eff}} = 2.0 \pm 0.1\,\text{nm}$. The broken lines in other plots connect the data points.

Although λ_s^{eff} indicates the scale of the Pt thickness for which the spin current flowing to the FM/NM interface begins to saturate, it is only a phenomenological number since both thickness-independent ρ_{Pt} and λ_s are assumed in Eq. (2.4). In a more realistic approach, given the non-uniformity of resistivity across the layer, both q_{SH} and λ_s will vary with location within the Pt film. In particular, since the E-Y mechanism [49,50] is expected to be the dominant spin scattering process in Pt, we should have $l_s \mu 1/r_{\text{Pt}}$. Hence λ_s near the Pt interfaces (where ρ_{Pt} is large) should be smaller than in the bulk. This means that the effective $\lambda_s^{\text{eff}} = 2.0$ nm obtained above from the simplified equation (2.4) yields an underestimate of λ_s within the bulk of the Pt film.

We have found that it is possible to go beyond this type of approximate treatment and perform, using a simple rescaling, a quantitative calculation of the spin torque (including SBF) even for a heavy-metal layer with a nonuniform resistivity and spin diffusion length, as long as (a) the intrinsic mechanism of the SHE dominates spin current generation and (b) the E-Y mechanism dominates spin relaxation. Assuming that these two conditions hold, we can then use the experimental values of $\xi_{\text{DL}}^{E}(t_{\text{Pt}})$ and $\rho_{\text{Pt}}(t_{\text{Pt}})$ to obtain an estimate for the value of $\lambda_s \rho_{\text{Pt}}$.

We first assume, as an exercise, that the thickness-dependence of Pt resistivity is due only to surface scattering at the Pt/Co interface. From the series of $\rho_{\text{Pt}}(t_{\text{Pt}}^n)$ as a function of Pt thickness presented in Fig. 2.1(a), we divide each of the Pt films into a series of adjacent "slices" of thickness l^i each of which has a different, but uniform, resistivity ρ_{Pt}^i and spin diffusion length $\lambda_s{}^i$. These divisions lead to the distribution of $r_{\text{Pt}}(z)$ as shown in Fig. 2.2(b), where the *z*-axis points normal to the layers with *z* = 0 starting at the Pt/Co interface. As fully discussed in SI, the spin transmission through the *i*-th slice is identical to that for an "effective" slice having a fixed spin diffusion length

λ_s^0, resistivity ρ_{Pt}^0 and a rescaled effective thickness $L^i = l^i \rho_{\mathrm{Pt}}^i / \rho_{\mathrm{Pt}}^0$ so that $\lambda_s^i \rho_{\mathrm{Pt}}^i = \lambda_s^0 \rho_{\mathrm{Pt}}^0$ which holds under the E-Y mechanism. Thus a Pt layer of thickness $t_{\mathrm{Pt}}^n = \sum_{i=1}^n l^i$ (a combination of *n* slices) with non-uniform resistivity and spin diffusion length is equivalent to a uniform "effective" Pt film having a thickness $T_{\mathrm{Pt}}^n = \sum_{i=1}^n L^i$, as schematically depicted in Fig. 2.2(a) for the case of a single interface. The same result can be obtained by the same manner when also including the second interface, i.e., although Fig. 2.2(a) changes in a way that $\rho_{\mathrm{Pt}}(t_{\mathrm{Pt}})$ has a minimum somewhere in the midst of the Pt, Fig. 2.2(b) and the consequent analysis would not change (see SI). Since the "effective" layers are chosen to have constant resistivity ρ_{Pt}^0 (we choose $15\ \mu\Omega\cdot\mathrm{cm}$) and spin diffusion length λ_s^0, we can fit the ξ_{DL}^E data versus the rescaled thickness T_{Pt} to Eq. (2.4), just substituting T_{Pt} instead of t_{Pt}. One important factor we need to consider is the location of the Pt/Co interface, which is not necessarily at $z = 0$. This is because a few atomic layers of Pt at each of the interfaces may be intermixed with the adjacent material, and/or in the case of the Pt/Co interface magnetized by the proximity effect [58]. This can result in a small offset t_{off} because the thickness of the first slice is smaller than its nominal value. This effect seems to be apparent in Fig. 2.1(d) where the fitted line (which goes through the origin) does not fit the data particularly well in the thin Pt region. We address this issue in our analysis by replacing T_{Pt} in the right hand side of equation (2.4) by $T_{\mathrm{Pt}} - T_{\mathrm{off}}$ where T_{off} is the location of the FM/NM interface and is estimated from the fitting.

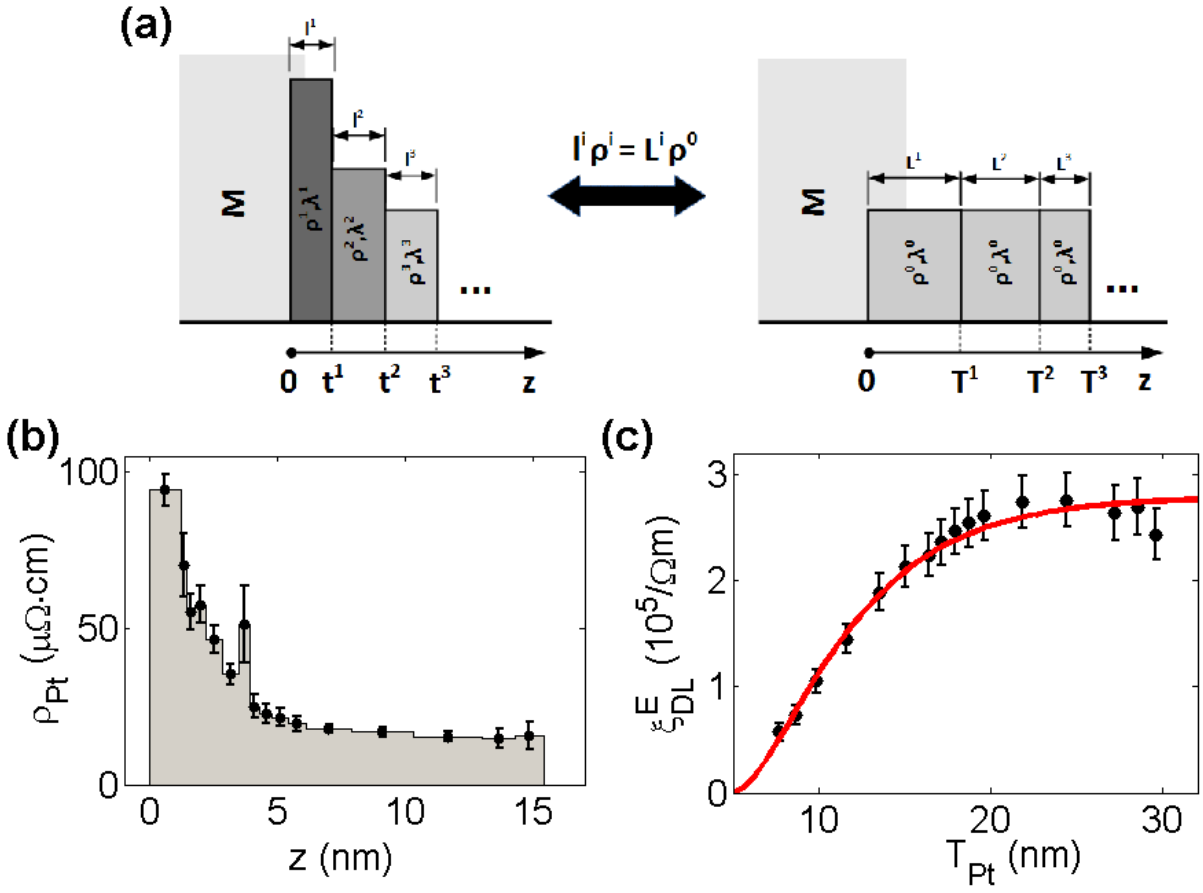

Figure 2.2: Estimation of spin diffusion length within the E-Y mechanism. **(a)** Schematic illustration of the "slicing" and "rescaling" process in which a non-uniform layer t_{Pt}^n is scaled into a uniform one T_{Pt}^n. See full description in the main text. **(b)** The distribution of Pt local resistivity with location *z*, extracted from the experimental Ta/Pt/Co data in Fig. 2.1(a). The points represent the local resistivity of each "slice". **(c)** Damping-like spin torque efficiency per unit applied electric field versus "effective" thickness T_{Pt}. The solid line shows the fitted result from which the spin diffusion length of Pt at $\rho_{\mathrm{Pt}}^0 = 15\,\mu\Omega\mathrm{cm}$ is estimated to be $\lambda_s^0 = 5.1 \pm 0.5\,\mathrm{nm}$.

The fitted result of the "effective" Pt layers with three free parameters σ_{SH}, λ_s^0 and T_{off} is shown in Fig. 2.2(c). We obtain $\lambda_s^0 = 5.1 \pm 0.5$ nm for $\rho_{Pt}^0 = 15$ μΩcm, or more generally we have $\lambda_s \rho_{Pt} = (0.77 \pm 0.08) \times 10^{-15}\ \Omega \cdot m^2$; $T_{off} = 4.9 \pm 0.3$ nm for the "effective" Pt thickness offset which corresponds to $t_{off} = 0.8 \pm 0.1$ nm in the original, un-scaled thickness; and $\sigma_{SH} = (5.9 \pm 0.2) \times 10^5\ [\hbar / 2e]\ \Omega^{-1} m^{-1}$ independent of ρ_{Pt}, if no SML is present. If we use a somewhat higher $G_r = 1.07 \times 10^{15}\ \Omega^{-1} m^{-2}$ as calculated including spin orbit effects for the Py/Pt interface [47] then $\sigma_{SH} = (4.5 \pm 0.1) \times 10^5\ [\hbar / 2e]\ \Omega^{-1} \cdot m^{-1}$, again a lower bound. We reiterate that the existence of SML would increase the estimated σ_{SH} but negligibly affect our determination of λ_s^0. As a final check of this analysis we note the requirement of the E-Y mechanism that the spin relaxation time τ_s be longer than the momentum scattering time τ_m. It has been reported that the mean free path l_{mfp} in Pt can be estimated from $l_{mfp}[m] \approx 8 \times 10^{-16} / \rho_{Pt}\ [\Omega \cdot m]$ [59]. Thus we have $\tau_{sf} / \tau_m = 3(\lambda_s / l_{mfp})^2 \approx 3\left[\lambda_s \rho_{Pt} / \left(8 \times 10^{-16}\right)\right]^2 = 2.8$, which is consistent with the E-Y spin scattering mechanism being dominant in Pt.

We now discuss our results in relation with previous results in the literature. First, as noted above, previous ST-FMR and ISHE studies on in-plane magnetized (IPM) Pt/Py bilayers [38,40,44] did not yield a peak in the apparent damping-like spin torque efficiency as a function of t_{Pt} such as reported here. These previous analyses also reported a short $\lambda_s \approx 1.4$ nm as determined by RT ST-FMR, or alternatively by ISHE, on Py/Pt [38,40,44] and $\lambda_s \approx 2.1$ nm for $Co_{75}Fe_{25}$/Pt [45], in the same range as $\lambda_s^{eff} = 2.0$ nm. These differences with our results can be explained by a weaker thickness dependence of the resistivity for multilayers made from different

materials and the neglect of any field-like torque in the analysis. See SI for further discussion on these points.

An alternative approach to estimate λ_s is to measure the t_{Pt} dependence of Gilbert magnetic damping in bilayer samples, and such a study has recently reported $\lambda_s = 0.5 \pm 0.3$ nm [42]. Fast saturation of the damping at very thin Pt thicknesses has also been observed previously [22,37,38]. However, Liu *et al*. [47] have recently pointed out that this very rapid attenuation is likely due to strong SML at the FM/Pt interface, and used a first principles calculation and data [60] from this measurement method to obtain $\lambda_s \approx 5.5$ nm, or more generally $\lambda_s \rho_{Pt} = (0.61 \pm 0.02) \times 10^{-15}\ \Omega \cdot m^2$. On the other hand, a longer $\lambda_s \approx 8.0$ nm has been reported [21,22] from ISHE experiments on Py/Pt at RT. However, these latter works did not consider SML or spin backflow at the FM-NM interface which would reduce their estimated values, as pointed out by Jiao *et al*. [43]. Rojas-Sanchez *et al*. [23] performed similar measurement on Co/Pt and, after taking SML into account, reported $\lambda_s = 3.4 \pm 0.4$ nm and $\lambda_s \rho_{Pt} = (0.59 \pm 0.06) \times 10^{-15}\ \Omega \cdot m^2$. These experiments did not consider the non-uniformity of the local resistivity $\rho_{Pt}(t_{Pt})$ and its effect on $I_s(t_{Pt})$, and thus underestimated the value of $\lambda_s \rho_{Pt}$. A very high value $\lambda_s = 11 \pm 2$ nm has been determined from a low temperature, 3-10 K, study of spin pumping in lateral spin valves [39,41] for samples having $\rho_{Pt} = 12\ \mu\Omega \cdot cm$, or $\lambda_s \rho_{Pt} = 1.32 \times 10^{-15}\ \Omega \cdot m^2$. However, Isasa *et al.* used a similar lateral spin value technique and reported $\lambda_s \rho_{Pt} = (0.85 \pm 0.08) \times 10^{-15}\ \Omega \cdot m^2$ at 10 K and $(0.79 \pm 0.87) \times 10^{-15}\ \Omega \cdot m^2$ at RT [57], while measurements using current-perpendicular to the plane studies of Py-based exchange biased spin valves [26] at 4.2 K have reported $\lambda_s \rho_{Pt} = (0.59 \pm 0.25) \times 10^{-15}\ \Omega \cdot m^2$ [37] and

$(0.72 \pm 0.13) \times 10^{-15}\ \Omega \cdot \mathrm{m}^2$ [46]. All of these latter results are in reasonable agreement with our result $\lambda_s \rho_{\mathrm{Pt}} = (0.77 \pm 0.08) \times 10^{-15}\ \Omega \cdot \mathrm{m}^2$.

In summary, we have observed a strong dependence on t_{Pt} for the damping-like SH torque efficiency per unit applied current density for perpendicularly-magnetized Pt/Co bilayer structures, with a peak value $\xi^j_{\mathrm{DL}} = 0.12$ at $t_{\mathrm{Pt}} = 2.8 - 3.9$ nm, while the spin torque efficiency per unit applied electric field exhibits a monotonic increase with increasing Pt thickness and saturates for $t_{\mathrm{Pt}} > 5$ nm. We interpret this behavior as an indication that the intrinsic SHE being the dominant SHE mechanism in Pt, perhaps in combination with side-jump scattering, so that the SH conductivity is independent of mean free path while the SH torque efficiency per unit current density is enhanced by an increased $\rho_{\mathrm{Pt}}(t_{\mathrm{Pt}})$ associated with interfacial scattering. By assuming the E-Y mechanism for spin scattering, which implies that $\lambda_s \propto 1/\rho_{\mathrm{Pt}}$ so that λ_s is also non-uniform, we obtain $\lambda_s \rho_{\mathrm{Pt}} = (0.77 \pm 0.08) \times 10^{-15}\ \Omega \cdot \mathrm{m}^2$. With this result we can apply SBF analysis to our direct measurements of ξ^E_{DL} for this PMA system using $G_r = 0.59 \times 10^{15}\ \Omega^{-1}\mathrm{m}^{-2}$ [24], and obtain $\sigma^{\mathrm{Pt}}_{\mathrm{SH}} = (5.9 \pm 0.2) \times 10^5\ [\hbar / 2e]\ \Omega^{-1} \cdot \mathrm{m}^{-1}$, with this being a lower bound as it is made with the assumption that there is no significant SML at our Pt/Co interfaces.

This work seems to resolve the controversy regarding the differences in the value of λ_s for Pt as obtained from various spin Hall and other experiments, and demonstrates that the spin Hall efficiency of Pt can be enhanced by increasing its resistivity, as expected when the intrinsic SHE is dominant.

We thank Y. Ou, C.-F. Pai and S. Emori for fruitful discussions, G. E. Rowlands for technical support and F. Guo for commenting on the manuscript. This work was supported in part by the Samsung Electronics Corporation, by the NSF/MRSEC program (DMR-1120296) through, the

Cornell Center for Materials Research, and by ONR. We also acknowledge support from the NSF (Grant No. ECCS-0335765) through use of the Cornell Nanofabrication Facility/National Nanofabrication Infrastructure Network.

SUPPLEMENTAL INFORMATION

2.S1. Discussion of the details of the rescaling analysis

2.S1(a) For one interface

In the main text, we treat the non-uniform $\rho_{\rm Pt}(t_{\rm Pt}^n)$ by dividing each the Pt layer with thickness $t_{\rm Pt}^n$ into *n* slices of thickness l^i and uniform resistivity $\rho_{\rm Pt}^i$ so that

$$\frac{t_{\rm Pt}^n}{\rho_{\rm Pt}(t_{\rm Pt}^n)} = \sum_{i=1}^{n} \frac{l^i}{\rho_{\rm Pt}^i}. \qquad (2.S1)$$

For the case of one interface between Pt and another metal layer (M), the process is illustrated in Fig. 2.2(a)-(b) in the main text. To account for the variation of $\lambda_s^{\,i}$ from slice to slice, let us consider the transmission of spin current through the *i*-th layer. For a simple drift-diffusion model [61], let $\mu_s(z)$ be the spin potential satisfying the diffusion equation $\nabla^2\mu_s(z) = \mu_s(z)/(\lambda_s^i)^2$, and $j_s(z) = j_{\rm SHE} - \nabla\mu_s(z)/\rho^i$ be the local spin current, where $j_{\rm SHE} = \sigma_{\rm SH}\cdot E$ is the SHE-induced spin current which is constant, the same for all slices, since the applied electric field is the same in all slices and $\sigma_{\rm SH}$ is independent of resistivity if the intrinsic SHE mechanism dominates. Elementary calculus shows that the relation of $\{\, j_s(z)\,,\,\mu_s(z)\,\}$ at the two surfaces $z = z_1, z_2$ of the *i*-th slice can be expressed as [48]

$$\begin{pmatrix} j_s(z_1) - j_{SHE} \\ \mu_s(z_1) \end{pmatrix} = \Pi(l^i/\lambda_s^i, \lambda_s^i\rho^i)\cdot\begin{pmatrix} j_s(z_2) - j_{SHE} \\ \mu_s(z_2) \end{pmatrix}, \qquad (2.S2)$$

where

$$\Pi(\alpha,\beta) \equiv \begin{pmatrix} \cosh\alpha & (\sinh\alpha)/\beta \\ (\sinh\alpha)\cdot\beta & \cosh\alpha \end{pmatrix} \qquad (2.S3)$$

is the spin transmission matrix of the *i*-th slice. Since $\Pi(l^i/\lambda_s^i, \lambda_s^i\rho^i)$ depends only on

$\lambda_s^i \rho_{\mathrm{Pt}}^i$=constant (E-Y mechanism) and l^i / λ_s^i, the calculation for the *i*-th slice is identical to that for an "effective" slice having a fixed spin diffusion length λ_s^0, resistivity ρ_{Pt}^0 and a rescaled effective thickness $L^i = l^i \rho_{\mathrm{Pt}}^i / \rho_{\mathrm{Pt}}^0$ so that $\lambda_s^i \rho_{\mathrm{Pt}}^i = \lambda_s^0 \rho_{\mathrm{Pt}}^0$ which holds under the E-Y mechanism. Thus a Pt layer of thickness $t_{\mathrm{Pt}}^n = \sum_{i=1}^n l^i$ (a combination of *n* slices) with non-uniform resistivity and spin diffusion length is equivalent to a uniform "effective" Pt film having a thickness

$$T_{Pt}^n = \sum_{i=1}^n L^i = \sum_{i=1}^n l^i \rho_{\mathrm{Pt}}^i / \rho_{\mathrm{Pt}}^0 . \qquad (2.S4)$$

The analysis using this scaling process performed in the main text assumed the surface scattering occurred at only the Pt/Co interface. If the surface scattering at the Ta/Pt interface is a major contributor to the increase of ρ_{Pt} in the thin Pt region the slicing process will result in a distribution of ρ_{Pt} that is horizontally opposite to Fig. 2.2(b). Since the spin transmission matrix $\Pi(l / \lambda_s, \lambda_s \rho)$ defined by Eq. (2.S3) is *commutative within the E-Y mechanism*, i.e. if $\lambda_s^1 \rho^1 = \lambda_s^2 \rho^2$ then

$$\Pi(l^1 / \lambda_s^1, \lambda_s^1 \rho^1) \cdot \Pi(l^2 / \lambda_s^2, \lambda_s^2 \rho^2) = \Pi(l^2 / \lambda_s^2, \lambda_s^2 \rho^2) \cdot \Pi(l^1 / \lambda_s^1, \lambda_s^1 \rho^1), \qquad (2.S5)$$

we can interchange any two adjacent slices without affecting the spin transmission through the two slices. As a result, the slices can be rearranged in an arbitrary order and therefore the same result will be obtained whether the interfacial scattering occurs predominately at either the Ta/Pt or the Pt/Co interface.

2.S1(b) For two interfaces

We now prove that the rescaling process would yield the same result for the case where the surface scattering occurs at two interfaces. The slicing process still follows relation (2.S1) but the location of the *(i+1)*-th slice is not at the far end of the *i*-th slice as in the case of one interface,

instead it is somewhere in the midst of the *i*-th slice. To model this difference, we notice that

$$\Pi((l_1+l_2)/\lambda_s, \lambda_s\rho) = \Pi(l_1/\lambda_s, \lambda_s\rho)\cdot\Pi(l_2/\lambda_s, \lambda_s\rho) \qquad (2.S6)$$

which allows us to further divide the *i*-th slice into two thinner slices with thickness l_{L}^i and l_{R}^i (*not* necessarily the same) so that $l^i = l_{\mathrm{L}}^i + l_{\mathrm{R}}^i$, between which the *(i+1)*-th slice is located. The "slicing" process is carried out in the same manner for the next slices and illustrated in Fig. 2.S1(a)-(c). The resulted distribution of ρ_{Pt} with location is now different from the case of one interface in that ρ_{Pt} is minimum somewhere in the midst of Pt layer. However, after rescaling the slices by the same rule $L_{\mathrm{L(R)}}^i = l_{\mathrm{L(R)}}^i \rho_{\mathrm{Pt}}^i / \rho_{\mathrm{Pt}}^0$, as illustrated in Fig. 2.S1(d), the original Pt layer of thickness t_{Pt}^n and non-uniform resistivity becomes a uniform layer of fixed ρ_{Pt}^0 and thickness

$$T_{Pt}^n = \sum_{i=1}^{n}(L_{\mathrm{L}}^i + L_{\mathrm{R}}^i) = \sum_{i=1}^{n}(l_{\mathrm{L}}^i + l_{\mathrm{R}}^i)\rho_{\mathrm{Pt}}^i / \rho_{\mathrm{Pt}}^0 = \sum_{i=1}^{n} l^i \rho_{\mathrm{Pt}}^i / \rho_{\mathrm{Pt}}^0 \qquad (2.S7)$$

which is the same as (2.S4). Therefore, the rescaling process yields the same final result for both cases of one (either Ta/Pt or Pt/Co) and two interfaces.

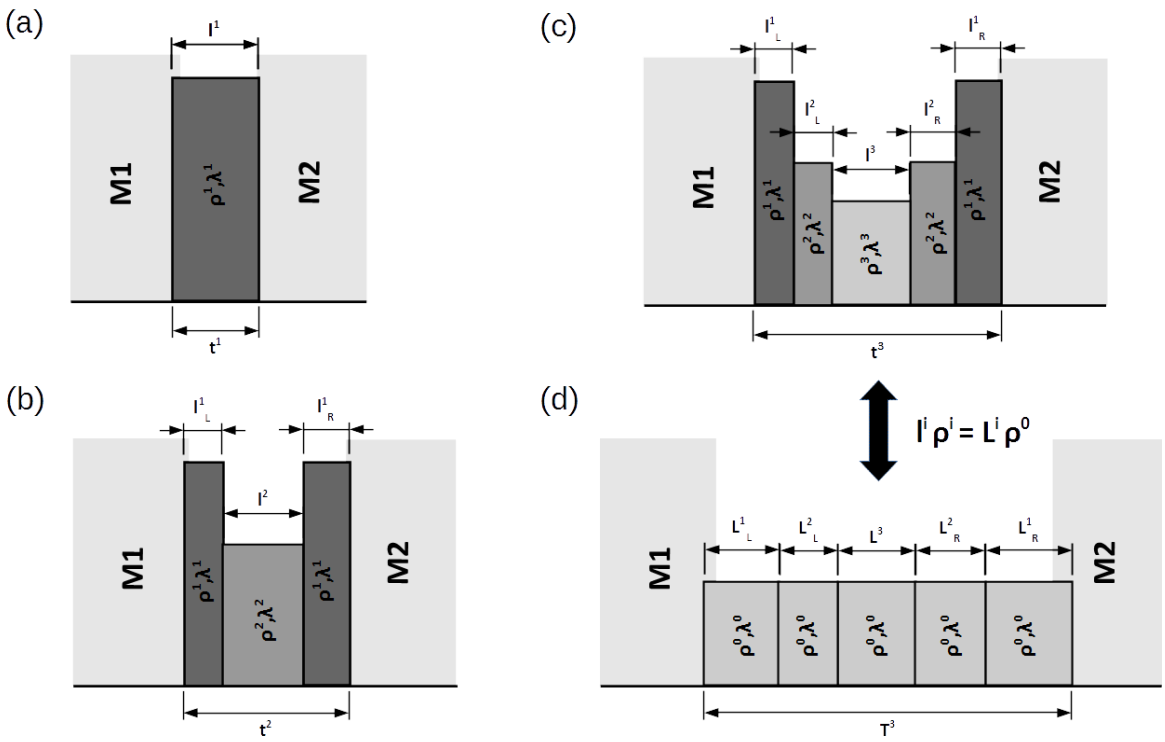

Figure 2.S1. Illustration of the scaling process for two interfaces: **(a)-(c)** Illustration of the "slicing" process in which the *(i+1)*-th slice is placed in the midst of the *i*-th slice. **(d)** Result of the rescaling process (shown for $n = 3$).

2.S2. Discussion of previous SHE measurements on Py/Pt bilayers

Here we discuss the previously reported determinations of spin diffusion length λ_s using spin torque ferromagnetic resonance (ST-FMR) measurement [38,40,45] and inverse spin Hall effect (ISHE) [44] with changing thickness of Pt layer. First, we note that previous ST-FMR and ISHE studies on in-plane magnetized (IPM) Pt/Py bilayers [38,40,44] did not yield a peak in the apparent damping-like spin torque efficiency ξ^j_{FMR} as a function of t_{Pt} such as reported here. Second, those early works estimated a short estimated spin diffusion length $\lambda_s \approx 1.4\,\mathrm{nm}$. These discrepancies with our results can be attributed to two main causes:

i. The neglecting of any possible field-like torque in the analysis.

ii. The weaker thickness dependence of the average electrical resistivity of the Pt layers.

2.S2(a) Effect of a field-like torque in ST-FMR measurement

In many ST-FMR measurements of NM/FM bilayers, a torque efficiency ξ^j_{FMR} is determined by the ratio of the symmetric and anti-symmetric components of the FMR lineshape. If no significant field-like spin transfer torque effect is present, the anti-symmetric component is due to only the Oersted field from the electric current flowing in the NM layer. In that ideal case, $\xi^j_{\mathrm{FMR}} = \xi^j_{\mathrm{DL}}$. However, if a significant field-like torque ξ_{FL} is present, the anti-symmetric component of ST-FMR lineshape is the combined effect of both the Oersted field and ξ_{FL}. Thus in a more general case, ξ^j_{FMR} can be expressed as [29]

$$\frac{1}{\xi^j_{\mathrm{FMR}}} = \frac{1}{\xi^j_{\mathrm{DL}}}\left(1+\frac{\hbar}{e}\frac{\xi^j_{\mathrm{FL}}}{\mu_0 M_s t^{\mathrm{eff}}_{\mathrm{FM}} t_{\mathrm{NM}}}\right) \qquad (2.S8)$$

where $t^{\mathrm{eff}}_{\mathrm{FM}}$ is the effective thickness of the FM layer and t_{NM} is the NM thickness. Of course, both ξ^j_{DL} and ξ^j_{FL} can be thickness dependent, as demonstrated in the main text. Therefore the

determination of ξ^j_{DL} from ξ^j_{FMR} is not straightforward.

To illustrate the effect of field-like torque on the thickness dependence of ξ^j_{FMR}, we attempt to estimate ξ^j_{DL} from the values of ξ^j_{FMR} in Ref. [38], using the value $\xi^j_{FL} = +0.024$ which was recently estimated for Py(2.5)/Pt(4) (Py = $Ni_{80}Fe_{20}$, thickness in nanometer) [34] . For the purpose of this discussion we assume ξ^j_{FL} to be independent of t_{Pt}. Using equation (2.S8), ξ^j_{DL} is estimated and is shown in Fig. 2.S2(a) as a function of t_{Pt}. A peak in ξ^j_{DL} is clearly seen about $t_{Pt} = 2-3$ nm , which is similar in location to the result (Fig. 2.1 (c)) described in the main text, but less pronounced in amplitude due to the lower variation of $r_{Pt}(t_{Pt})$ in the Pt/Py bilayers.

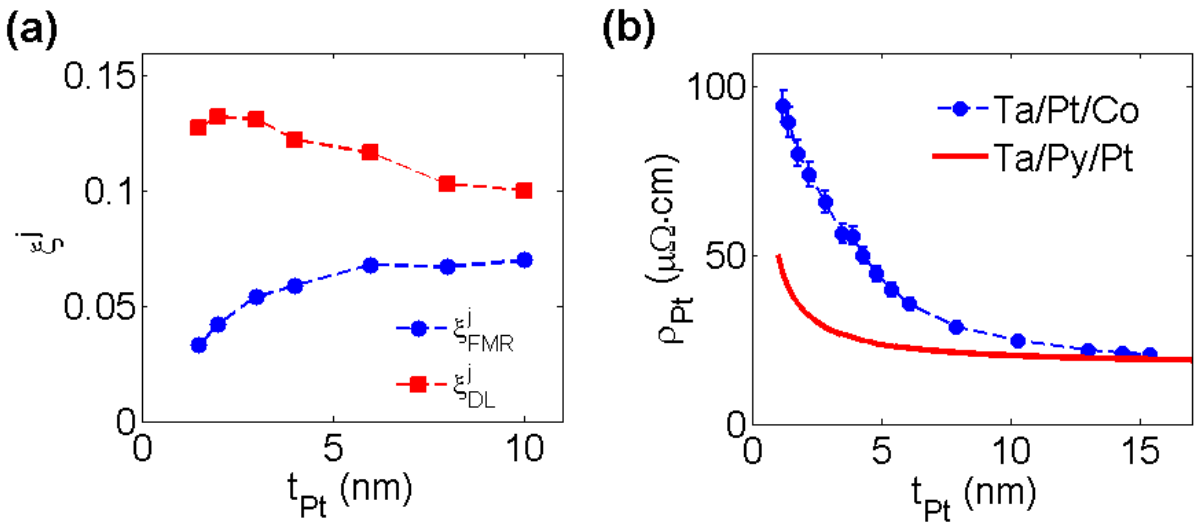

Figure 2.S2. **(a)** ξ^j_{FMR} determined from ST-FMR measurements on Py/Pt, taken from Ref. [38], and the estimated ξ^j_{DL} using equation (S8) with $\xi^j_{\mathrm{FL}} = +0.024$ reported by Ref. [34]. A small peak in ξ^j_{DL} is seen about $t_{\mathrm{Pt}} = 2-3\,\mathrm{nm}$. **(b)** Pt resistivity in *substrate*/Ta(1)/Pt/Co(1) multilayers (points) and *substrate*/Ta(3)/Py(3)/Pt multilayers (solid line, estimated in Ref. [48]) as functions of t_{Pt}. The dashed lines connect the data points.

2.S2(b) Thickness dependence of resistivity

Most experimental studies on the SHE and ISHE so far have assumed a uniform electrical resistivity ρ, thus a constant spin Hall angle. In a more realistic situation, the resistivity is non-uniform due to surface scattering when the film is very thin, comparable to its mean free path. As discussed in the main text, in the intrinsic spin Hall effect (SHE), which was shown to be dominant in Pt, the spin Hall angle is proportional to the resistivity. In multilayers having strong surface scattering at Pt interfaces, ξ_{DL}^{j} depends on both the relative magnitude of the Pt thickness to its spin diffusion length *and* the electrical resistivity ρ_{Pt}, and thus may exhibit a peak as in our study. However in the earlier bilayer studies [38,40,44,45] only one surface of the Pt layer was adjacent to a metal, a rather thick and relatively low resistivity Py layer, while the other surface was either an oxide (e.g., SiO_2 or AlO_x) or simply exposed to air. These differences substantially reduce the diffusive surface scattering contributions to the Pt resistivity compared to that which occurs in our *substrate*/Ta(1)/Pt/Co(1) trilayer structures, and thus while $\rho_{Pt}^{Py/Pt}(t_{Pt})$ still varies with t_{Pt} in the thin limit, the variation is less strong than for $\rho_{Pt}^{Ta/Pt/Co}(t_{Pt})$.

Fig. 2.S2(b) shows ρ_{Pt} for our *substrate* | Ta(1) | Pt | Co(1) samples (points) and for *substrate* | Ta(3) | Py(3) | Pt structure (solid line) which was estimated in Ref. [48]. It is clearly seen that ρ_{Pt} in Ta/Pt/Co has a stronger t_{Pt} dependence, which is due to stronger surface scattering with Ta and Co layers than Py/Pt. This weaker thickness dependence of ρ_{Pt} in Py/Pt bilayer contributes to the absence of a peak in ξ_{DL}^{j} as reported by Ref. [38,40,45]. Nevertheless, as long as there is increased scattering at the Pt/FM interface and the E-Y spin scattering mechanism is dominant, then any analysis which assumes a constant $\lambda_s(t_{Pt})$ will result in an underestimate of its "bulk" value. This explains the short $\lambda_s \approx 1.4\,\text{nm}$ as determined by RT ST-FMR on

Py/Pt [38,40,44] and $\lambda_s \approx 2.1\,\text{nm}$ for $Co_{75}Fe_{25}$/Pt [45], in the same range as $\lambda_s^{\text{eff}} = 2.0 \pm 0.1\,\text{nm}$ that we obtained by assuming a constant λ_s in fitting to Eq. (2.4).

2.S3. Effect of 1 nm Ta seeding layer

The multilayers in our study were grown on oxidized Si substrates with 1 nm Ta seeding layer. Due to the strong bonding of Ta ions to oxide surfaces and to the strong metallic bonding that occurs between Ta and most transition metals, a thin Ta seeding layer is known to be effective for serving as a strong adhesion and smoothing layer, reducing the grain size of the upper layer, as discussed in details in Ref. [51], and is widely used in spintronics studies [29,34,48] and applications. To minimize the spin torque contributions from the Ta seeding layer, its thickness was chosen to be low, 1 nm. The resistivity of the 1 nm Ta seed layer was $560\,\mu\Omega\cdot\mathrm{cm}$ as determined by a 4-probe resistance measurement of a multilayer stack consisting of substrate/Ta(1)/MgO(1)/Ta(1, oxidized cap). To examine the effect of the 1 nm Ta seeding layer in our multilayers, we measured the averaged resistivity of Pt thin films sputtered directly on the substrate and compared to films deposited on a 1 nm Ta seeding layer (after subtracting of the contribution from the 1 nm Ta layer). The results are shown on Fig. 2.S3 along with the averaged resistivity of Pt in the multilayers in our study (which is shown on Fig. 2.1(a) in the main text). It is clear from Fig. 2.S3 that the Pt film when deposited onto a bare oxide substrate (red) is very resistive when its average thickness is less than 2.5 nm, with the resistivity rising very quickly with decreasing thickness below this point, while for thicker Pt films on SiO_2 the resistivity is slightly less than when deposited on Ta. This behavior is directly attributable a comparably large grain size in the Pt films deposited on oxide that is due to the lack of strong adhesion between the Pt atoms and the oxide surface, which leads to less than full coverage of the surface in the less than 2.5 nm thickness range. The resistivity of Pt film deposited on a 1 nm Ta seeding layer (blue) is much lower in the thin regime, indicating the role of the Ta seeding layer in smoothing the surface and reducing Pt grain size. Finally, the Pt resistivity in the Ta/Pt/Co multilayer used in our study

is very similar to that of Ta/Pt sample, indicating that the diffusive scattering at Ta/Pt interface is dominant in increasing Pt resistivity in thin Pt regime.

Next, we estimate the contribution to the spin torques in the Co layer from the 1 nm Ta seeding layer. It has been shown that high resistivity beta-phase Ta has a negative spin Hall angle [19] whose magnitude is about 0.11 - 0.15. The strength of the contribution of the current in the Ta layer to the spin torque on the Co will depend on whether the SHE in Ta is intrinsic or extrinsic:

Case 1: If the dominant mechanism of SHE in Ta is intrinsic and/or side-jump then the spin Hall conductivity of Ta is constant, independent of Ta thickness and resistivity. Taking the values reported in Ref. [19], we can estimate

$$\sigma_{\mathrm{SH}}^{\mathrm{Ta}} = (\hbar / 2e) \cdot \theta_{\mathrm{SH}}^{\mathrm{Ta}} / \rho_{\mathrm{Ta}} \approx -0.79 \times 10^{5} [\hbar / 2e]\, \Omega^{-1} \cdot \mathrm{m}^{-1} \quad \text{(2.S9)}$$

Case 2: If the dominant mechanism for SHE in Ta is skew-scattering then the spin Hall angle $\theta_{\mathrm{SH}}^{\mathrm{Ta}}$ is constant, independent of Ta thickness and resistivity. Since the measured resistivity of our 1 nm Ta seeding layer $\approx 560\ \mu\Omega \cdot \mathrm{cm}$ is much higher than that reported for the 8 nm Ta layer in Ref. [19], the value of the spin Hall conductivity $\sigma_{\mathrm{SH}}^{\mathrm{Ta}}$ of the 1 nm Ta layer will be about 3 times smaller than the value in (2.S9).

Thus we only need to consider Case 1. To estimate the maximum spin current from the Ta layer that reaches the Pt/Co interface, we consider the $t_{\mathrm{Pt}} = 1.2\ \mathrm{nm}$ sample (smallest Pt thickness) and assume that all the spin current from the Ta layer flows through the Pt layer without attenuation. The ratio of the spin currents generated by the Ta and Pt layer is, approximately,

$$\frac{j_s^{\mathrm{Ta}}}{j_s^{\mathrm{Pt}}} \sim \frac{\sigma_{\mathrm{SH}}^{\mathrm{Ta}}}{\sigma_{\mathrm{SH}}^{\mathrm{Pt}}} \times \frac{t_{\mathrm{Ta}}}{t_{\mathrm{Pt}}} \approx -0.12\,. \quad \text{(2.S10)}$$

This introduces an error of about $0.06 \times 10^{5}\ / \Omega\mathrm{m}$ to the first data point in Fig. 2.1(d) shown in the

main text. In reality, the error caused by the Ta seeding layer will be smaller due to the spin attenuation in the Pt layer.

The above estimated (maximum) error caused by the 1 nm Ta seeding layer was included in estimating the uncertainty for the data points shown in Fig. 2.1(c, d) and Fig. 2.2(b) in the main text. The fitted values reported in the main text were obtained by a weighted fitting technique that takes into account the uncertainty of the data points.

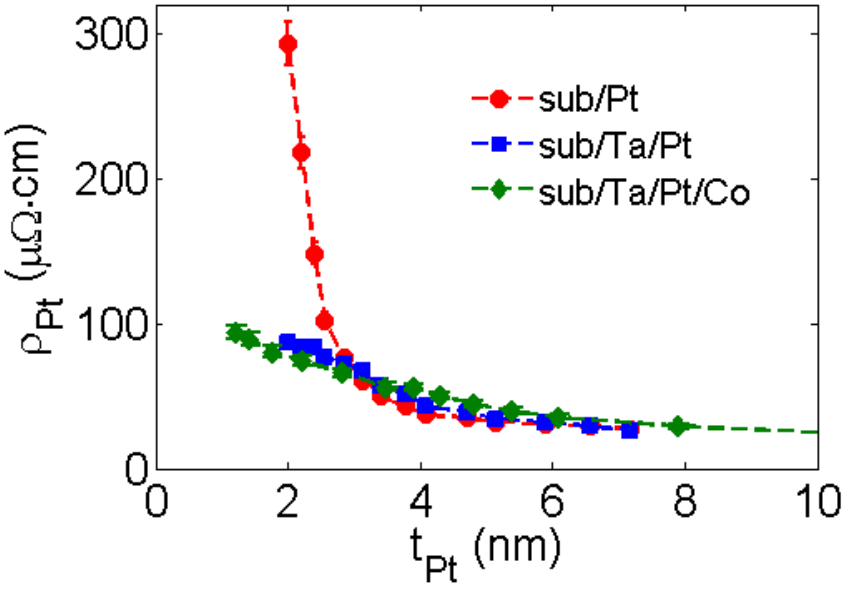

Figure 2.S3: Averaged resistivity of Pt in Pt thin films grown directly on Si/SiO_2 substrate (red), on 1 nm Ta seeding layer (blue) and in our samples in the main text (green) versus Pt thickness.

REFERENCES

[1] M. I. Dyakonov and V. I. Perel, Phys. Leters **35A**, 459 (1971).

[2] J. Hirsch, Phys. Rev. Lett. **83**, 1834 (1999).

[3] S. Zhang, Phys. Rev. Lett. **85**, 393 (2000).

[4] C.-F. Pai, L. Liu, Y. Li, H. W. Tseng, D. C. Ralph, and R. A. Buhrman, Appl. Phys. Lett. **101**, 122404 (2012).

[5] L. Liu, C.-F. Pai, D. C. Ralph, and R. A. Buhrman, Phys. Rev. Lett. **109**, 186602 (2012).

[6] V. E. Demidov, S. Urazhdin, H. Ulrichs, V. Tiberkevich, A. Slavin, D. Baither, G. Schmitz, and S. O. Demokritov, Nat. Mater. **11**, 1028 (2012).

[7] V. E. Demidov, H. Ulrichs, S. V Gurevich, S. O. Demokritov, V. S. Tiberkevich, A. N. Slavin, A. Zholud, and S. Urazhdin, Nat. Commun. **5**, 3179 (2014).

[8] T. Jungwirth, J. Wunderlich, and K. Olejník, Nat. Mater. **11**, 382 (2012).

[9] P. P. J. Haazen, E. Murè, J. H. Franken, R. Lavrijsen, H. J. M. Swagten, and B. Koopmans, Nat. Mater. **12**, 299 (2013).

[10] N. Okamoto, H. Kurebayashi, T. Trypiniotis, I. Farrer, D. A. Ritchie, E. Saitoh, J. Sinova, J. Mašek, T. Jungwirth, and C. H. W. Barnes, Nat. Mater. **13**, 932 (2014).

[11] D. Bhowmik, L. You, and S. Salahuddin, Nat. Nanotech. **9**, 59 (2013).

[12] D. M. Bromberg, D. H. Morris, L. Pileggi, and J.-G. Zhu, IEEE Trans. Magn. **48**, 3215 (2012).

[13] S. Urazhdin, V. E. Demidov, H. Ulrichs, T. Kendziorczyk, T. Kuhn, J. Leuthold, G.

Wilde, and S. O. Demokritov, Nat. Nanotech. **9**, 509 (2014).

[14] G. Vignale, J. Supercond. Nov. Magn. **23**, 3 (2010).

[15] A. Hoffmann, IEEE Trans. Magn. **49**, 5172 (2013).

[16] R. Karplus and J. M. Luttinger, Phys. Rev. **95**, 1154 (1954).

[17] L. Berger, Phys. Rev. B **2**, 4559 (1970).

[18] J. Smit, Physica **24**, 39 (1958).

[19] L. Liu, C.-F. Pai, Y. Li, H. W. Tseng, D. C. Ralph, and R. A. Buhrman, Science **336**, 555 (2012).

[20] J. Kim, J. Sinha, M. Hayashi, M. Yamanouchi, S. Fukami, T. Suzuki, S. Mitani, and H. Ohno, Nat. Mater. **12**, 240 (2013).

[21] H. Nakayama, K. Ando, K. Harii, T. Yoshino, R. Takahashi, Y. Kajiwara, K. Uchida, Y. Fujikawa, and E. Saitoh, Phys. Rev. B **85**, 144408 (2012).

[22] Z. Feng, J. Hu, L. Sun, B. You, D. Wu, J. Du, W. Zhang, A. Hu, Y. Yang, D. M. Tang, B. S. Zhang, and H. F. Ding, Phys. Rev. B **85**, 214423 (2012).

[23] J.-C. Rojas-Sánchez, N. Reyren, P. Laczkowski, W. Savero, J.-P. Attané, C. Deranlot, M. Jamet, J.-M. George, L. Vila, and H. Jaffrès, Phys. Rev. Lett. **112**, 106602 (2014).

[24] P. M. Haney, H.-W. Lee, K.-J. Lee, A. Manchon, and M. D. Stiles, Phys. Rev. B **87**, 174411 (2013).

[25] Y.-T. Chen, S. Takahashi, H. Nakayama, M. Althammer, S. Goennenwein, E. Saitoh, and G. Bauer, Phys. Rev. B **87**, 144411 (2013).

[26] W. Park, D. Baxter, S. Steenwyk, I. Moraru, W. Pratt, and J. Bass, Phys. Rev. B **62**, 1178 (2000).

[27] L. Liu, T. Moriyama, D. C. Ralph, and R. A. Buhrman, Phys. Rev. Lett. **106**, 036601 (2011).

[28] M.-H. Nguyen, C.-F. Pai, K. X. Nguyen, D. A. Muller, D. C. Ralph, and R. A. Buhrman, Appl. Phys. Lett. **106**, 222402 (2015).

[29] C.-F. Pai, Y. Ou, L. H. Vilela-Leão, D. C. Ralph, and R. A. Buhrman, Phys. Rev. B **92**, 064426 (2015).

[30] L. Liu, C.-T. Chen, and J. Z. Sun, Nat. Phys. **10**, 561 (2014).

[31] W. Zhang, W. Han, X. Jiang, S.-H. Yang, and S. S. P. Parkin, Nat. Phys. **11**, 496 (2015).

[32] X. Fan, J. Wu, Y. Chen, M. J. Jerry, H. Zhang, and J. Q. Xiao, Nat. Commun. **4**, 1799 (2013).

[33] X. Fan, H. Celik, J. Wu, C. Ni, K.-J. Lee, V. O. Lorenz, and J. Q. Xiao, Nat. Commun. **5**, 3042 (2014).

[34] T. Nan, S. Emori, C. T. Boone, X. Wang, T. M. Oxholm, J. G. Jones, B. M. Howe, G. J. Brown, and N. X. Sun, Phys. Rev. B **91**, 214416 (2015).

[35] T. D. Skinner, M. Wang, A. T. Hindmarch, A. W. Rushforth, A. C. Irvine, D. Heiss, H. Kurebayashi, and A. J. Ferguson, Appl. Phys. Lett. **104**, 62401 (2014).

[36] K. Garello, I. M. Miron, C. O. Avci, F. Freimuth, Y. Mokrousov, S. Blügel, S. Auffret, O. Boulle, G. Gaudin, and P. Gambardella, Nat. Nanotech. **8**, 587 (2013).

[37] H. Kurt, R. Loloee, K. Eid, W. P. Pratt, and J. Bass, Appl. Phys. Lett. **81**, 4787 (2002).

[38] L. Liu, R. A. Buhrman, and D. C. Ralph, arXiv:**1111.**3702 (2011).

[39] M. Morota, Y. Niimi, K. Ohnishi, D. H. Wei, T. Tanaka, H. Kontani, T. Kimura, and Y. Otani, Phys. Rev. B **83**, 174405 (2011).

[40] K. Kondou, H. Sukegawa, S. Mitani, K. Tsukagoshi, and S. Kasai, Appl. Phys. Express **5**, 73002 (2012).

[41] Y. Niimi, D. Wei, H. Idzuchi, T. Wakamura, T. Kato, and Y. Otani, Phys. Rev. Lett. **110**, 016805 (2013).

[42] C. T. Boone, H. T. Nembach, J. M. Shaw, and T. J. Silva, J. Appl. Phys. **113**, 153906 (2013).

[43] H. Jiao and G. E. W. Bauer, Phys. Rev. Lett. **110**, 217602 (2013).

[44] W. Zhang, V. Vlaminck, J. E. Pearson, R. Divan, S. D. Bader, and A. Hoffmann, Appl. Phys. Lett. **103**, 242414 (2013).

[45] A. Ganguly, K. Kondou, H. Sukegawa, S. Mitani, S. Kasai, Y. Niimi, Y. Otani, and A. Barman, Appl. Phys. Lett. **104**, 072405 (2014).

[46] H. Y. T. Nguyen, W. P. Pratt, and J. Bass, J. Magn. Magn. Mater. **361**, 30 (2014).

[47] Y. Liu, Z. Yuan, R. J. H. Wesselink, A. A. Starikov, and P. J. Kelly, Phys. Rev. Lett. **113**, 207202 (2014).

[48] C. T. Boone, J. M. Shaw, H. T. Nembach, and T. J. Silva, J. Appl. Phys. **117**, 223910 (2015).

[49] R. J. Elliott, Phys. Rev. **96**, 266 (1954).

[50] Y. Yafet, Solid State Phys. **14**, 1 (1963).

[51] J. M. Shaw, H. T. Nembach, T. J. Silva, S. E. Russek, R. Geiss, C. Jones, N. Clark, T. Leo, and D. J. Smith, Phys. Rev. B **80**, 184419 (2009).

[52] A. F. Mayadas and M. Shatzkes, Phys. Rev. B **1**, 1382 (1970).

[53] F. Warkusz, Electrocompon. Sci. Technol. **5**, 99 (1978).

[54] H. D. Liu, Y. P. Zhao, G. Ramanath, S. P. Murarka, and G. C. Wang, Thin Solid Films **384**, 151 (2001).

[55] W. E. Bailey, S. X. Wang, and E. Y. Tsymbal, Phys. Rev. B **61**, 1330 (2000).

[56] V. Castel, N. Vlietstra, J. Ben Youssef, and B. J. Van Wees, Appl. Phys. Lett. **101**, 132414 (2012).

[57] M. Isasa, E. Villamor, L. E. Hueso, M. Gradhand, and F. Casanova, Phys. Rev. B **91**, 024402 (2015).

[58] S. Y. Huang, X. Fan, D. Qu, Y. P. Chen, W. G. Wang, J. Wu, T. Y. Chen, J. Q. Xiao, and C. L. Chien, Phys. Rev. Lett. **109**, 107204 (2012).

[59] J. Bass and W. P. Pratt, J. Phys. Condens. Matter **19**, 183201 (2007).

[60] S. Mizukami, Y. Ando, and T. Miyazaki, Phys. Rev. B **66**, 104413 (2002).

[61] P. C. Van Son, H. Van Kempen, and P. Wyder, Phys. Rev. Lett. **58**, 2271 (1987).

CHAPTER 3

Enhanced Spin Hall Torque Efficiency in $Pt_{100-x}Al_x$ and $Pt_{100-x}Hf_x$ Alloys Arising from the Intrinsic Spin Hall Effect

Minh-Hai Nguyen[1], Mengnan Zhao[1], D. C. Ralph[1,2], R. A. Buhrman[1]

[1]*Cornell University, Ithaca, New York 14853, USA*

[2]*Kavli Institute at Cornell, Ithaca, New York 14853, USA*

(Published: Applied Physics Letters **108**, 242407 on 14 June 2016)

ABSTRACT

We report that the spin Hall torque generated by Pt can be enhanced substantially by alloying with Al or Hf. We observe damping-like spin torque efficiency per unit applied current density as high as $\xi^j_{\mathrm{DL}} = 0.23 \pm 0.02$, nearly twice the maximum value reported for pure Pt. To achieve this maximum efficiency, a very thin (0.5 nm) Pt spacer layer is inserted between the alloy and the ferromagnet being manipulated, to avoid a degraded spin transparency at the alloy/ferromagnet interface.

MAIN TEXT

The spin Hall effect (SHE) [1–3] in heavy metals (HMs) has recently drawn much attention because of the potential to enable efficient manipulation of ferromagnetic (FM) layers in HM/FM heterostructures via a strong "damping-like" (DL) component of spin-transfer torque. The efficiency of this spin torque per unit applied charge current density in the HM, ξ^j_{DL}, can be characterized as $\xi^j_{\mathrm{DL}} = \theta_{SH} T_{\mathrm{int}}$, where $\theta_{\mathrm{SH}} \equiv (2e/\hbar) j_{\mathrm{SHE}} / j_e$ is the spin Hall angle describing the relative strength of the SHE-induced spin current density within the HM (j_{SHE}) to the applied charge current density (j_e), and $T_{\mathrm{int}} \leq 1$ is a transparency factor for the spin current to be transmitted across the HM/FM interface to apply a torque to the FM. Previous studies have found large spin-torque efficiencies from the pure heavy metals Pt (ξ^j_{DL} = 0.06-0.12 [4–6]; varying because T_{int} depends on the FM used [7,8]), beta-phase Ta ($\xi^j_{\mathrm{DL}} \geq 0.11$ [9]) and beta-phase W ($\xi^j_{\mathrm{DL}} \geq 0.3$ [10]), and also in the alloys Cu(Bi) [11], Cu(Ir) [12,13], Cu(Pb) [14], Au(W) [15] and AuCu [16]. The SHE in the pure materials is thought to arise from an intrinsic band structure effect [17,18], in which case increased scattering in the HM should cause θ_{SH} to increase proportionally with the electrical resistivity ρ [19,20]. As long as the interfacial spin transmission factor T_{int} changes only weakly, this suggests that ξ^j_{DL} can be beneficially enhanced by adding scattering centers to increase the electrical resistivity of the HM. Our research group has previously reported initial evidence of an enhancement in the SHE due to interface scattering in very thin Pt films [21] in which the intrinsic SHE mechanism has been shown to be dominant [17,21–24]. Here we test the prediction that increased bulk scattering should strengthen the intrinsic SHE by alloying Pt with another normal metal. To investigate whether there was a material difference on the spin Hall effect between the use of a light element dopant and a heavy

one we employed both Al and Hf as alloy components in this investigation. We find that increasing the resistivity of the Pt does increase ξ_{DL}^{j} significantly, although the rate of increase as a function of ρ is weaker than the predicted proportionality relationship. We propose that this is due, at least in part, to a decrease in T_{int} as a function of increased alloying. By using a very thin (0.5 nm) Pt spacer to engineer the interface between the alloy and the adjacent FM layer to maximize both the interfacial spin transparency and the perpendicular magnetic anisotropy (PMA), we obtain a maximum efficiency of $\xi_{DL}^{j} = 0.23 \pm 0.02$, nearly twice the previous record for Pt samples.

Our samples consist of Ta(1) | $Pt_{100-x}X_x$ (4 or 6) | Co(1) | MgO(2) | Ta(1) (X = Al or Hf) multilayers sputter-deposited on oxidized Si substrates in a base pressure of $\approx 4.0 \times 10^{-8}$ Torr. Here the numbers in parentheses are the thicknesses in nm and x (= 0 – 20) is the atomic % concentration of the impurities. The Ar gas pressure during sputtering was 3.5 mTorr for Pt deposition and 2.0 mT for other materials. The 1 nm Ta seeding layer results in a smoother multilayer [25] and enhances the PMA of the Co. The film thicknesses, averaged over the area of the films, were estimated from sputter-deposition rates that were calibrated by measuring the thicknesses of thick ~50 nm films by a contact stylus profilometer, which resulted in an uncertainty of less than 5%. The Pt alloy films were grown by co-sputtering with varied power, and with shutter control for x < 5%. We estimated the concentration of the Al or Hf from the calibrated deposition rates. In setting the thicknesses of the Pt alloy layers, we utilized our previous work [21] that has shown that the effective spin diffusion length of a thin layer of Pt in a Ta/Pt/Co system is about 2.0 nm, therefore a 4 nm or 6 nm Pt layer is sufficiently thick to provide a maximum spin torque efficiency. The as-deposited samples exhibit PMA with coercivity of > 0.2 T. The saturation magnetization is $M_s = (1.08 \pm 0.05) \times 10^6$ A/m with an apparent "magnetic dead layer" of

$t_{\mathrm{FM}}^{\mathrm{dead}} = 0.26 \pm 0.04\,\mathrm{nm}$ [8]. The multilayer stacks were patterned into $5\,\mu\mathrm{m} \times 60\,\mu\mathrm{m}$ Hall bars by photolithography and ion milling.

We determined the sheet conductance of the films by 4-probe resistance measurements on a set of microbars of varying width, length and probe spacing, which minimized errors due to sample geometry and reduced the statistical measurement error to below 1%. Thus the main source of error comes from the uncertainty of film thicknesses, which is about 5%. The averaged resistivity of the HM layer $\rho_{\mathrm{PtX}}^{\mathrm{avg}}$ was determined by subtracting the sheet conductance of a separately fabricated Ta(1) | Co(1) | MgO(2) | Ta(1) stack from that of our samples containing the HM layer. By the same manner, we estimated the averaged resistivity of the 1 nm Ta seeding layer to be $\approx 560\,\mu\Omega \cdot \mathrm{cm}$ which is much higher than that of the $Pt_{100-x}X_x$ layer (see Fig. 3.2(a)). Moreover, the Ta seeding layer is separated from the $Pt_{100-x}X_x$ /Co interface by $\geq 4\,\mathrm{nm}$, therefore its spin torque contribution is negligible and will be ignored in our analysis (detailed discussion of this point can be found in the Supplemental Information of Ref. [21]).

The averaged resistivity of 4 nm, 6 nm, and 50 nm $Pt_{100-x}X_x$ films are shown in Fig. 3.2(a) as a function of alloy concentration x for X = Al and Hf. We use the 50 nm films to approximate bulk properties. The resistivities for all three series increase almost linearly with the alloy concentration. The upward shift from the 50 nm to 6 nm, and from 6 nm to 4 nm series indicates strong diffusive interface scattering [21]. Notice that for the highest concentration of Al and Hf, the $Pt_{100-x}X_x$ averaged resistivity is about 2 times higher than that of pure Pt (x = 0) for X = Al and 3.5 times higher for X = Hf. If the interface transparency of the $Pt_{100-x}X_x$ alloys is the same for $0 \leq x \leq 20$ and the SHE is due to an intrinsic mechanism, we would then expect to achieve about 2 times higher θ_{SH} and ξ_{DL}^{j} for $Pt_{100-x}\,Al_x$ and 3.5 times higher for $Pt_{100-x}\,Hf_x$ compared to pure Pt.

We measured the DL spin torque efficiencies of these PMA samples at room temperature by

the harmonic response technique [26,8] with the same alternating voltage amplitude (4 V) applied to the Hall bars in all measurements, corresponding to an alternating electric field of constant magnitude $E = 67$ kV/m . Typical first- and second-harmonic responses, taken from the Pt(6)/Co(1) sample, are shown in Fig. 3.1. For in-plane field sweeps, the field magnitude was 0.05 - 0.2 T depending on the perpendicular anisotropy of the sample, without assistant out-of-plane field. The anisotropy field was determined from the first-harmonic response as

$$H_{\text{an}} = \left| V_{\text{AHE}} \Big/ \frac{\partial^2 V_{\varpi}}{\partial H_{\text{L(T)}}^2} \right|^{1/2} \tag{3.1}$$

where V_{AHE} is the anomalous Hall voltage which is determined from the field-swiching behavior shown in Fig. 3.1(a). The current-induced longitudinal and transverse effective fields were determined as

$$\Delta H_{\text{L(T)}} = -2 \frac{\partial V_{2\varpi}}{\partial H_{\text{L(T)}}} \Big/ \frac{\partial^2 V_{\varpi}}{\partial H_{\text{L(T)}}^2} . \tag{3.2}$$

Here we neglect any contribution from the thermoelectric effect [27] which has been shown to be very small in Pt/Co PMA and in-plane systems. We have also determined that there is negligible contribution from the transverse magnetoresistance effect (the net effect of the anisotropy and spin Hall magnetoresistance) to this measurement. To account for device variation, each data point is the average from two repeated measurements on devices at different locations on the same wafer and the deviation is included in the error bar on the data point. From the measured spin torque-induced longitudinal equivalent field ΔH_{L}, the spin torque efficiencies per unit average electric current density ξ_{DL}^{j} in the $Pt_{100-x}X_x$ layer is determined as

$$\xi_{\text{DL}}^{j} = \frac{2e}{\hbar} \mu_0 M_s (t_{\text{FM}} - t_{\text{FM}}^{\text{dead}}) \cdot \Delta H_{\text{L}} \,/\, j_e^{avg} \tag{3.3}$$

where $j_e^{avg} = E / \rho_{PtX}^{avg}$. The resultant values for the DL spin torque efficiencies are plotted versus Al and Hf concentration in Fig. 3.2(b).

Fig. 3.2(b) clearly shows that ξ_{DL}^{j} increases with increasing alloy concentration (resistivity). In particular, we achieved an increase from $\xi_{DL}^{j} \approx 0.10$ for pure Pt in these samples to $\xi_{DL}^{j} = 0.14 \pm 0.01$ for $Pt_{80}Al_{20}$ (for both 4 nm and 6 nm samples) and $\xi_{DL}^{j} = 0.16 \pm 0.01$ for 6 nm $Pt_{100-x}Hf_x$ with x = 10 - 15. These results are higher than any reported previously for pure Pt/FM bilayers [4–8], demonstrating the effective role of alloying in increasing the resistivity and consequently enhancing the spin Hall angle of $Pt_{100-x}X_x$. However Figs. 3.1(a) and (b) also show that the increase in ξ_{DL}^{j} is weaker than proportional to ρ_{PtX}^{avg}, the prediction for the intrinsic spin Hall effect under the assumption there are no detrimental consequences of the alloying.

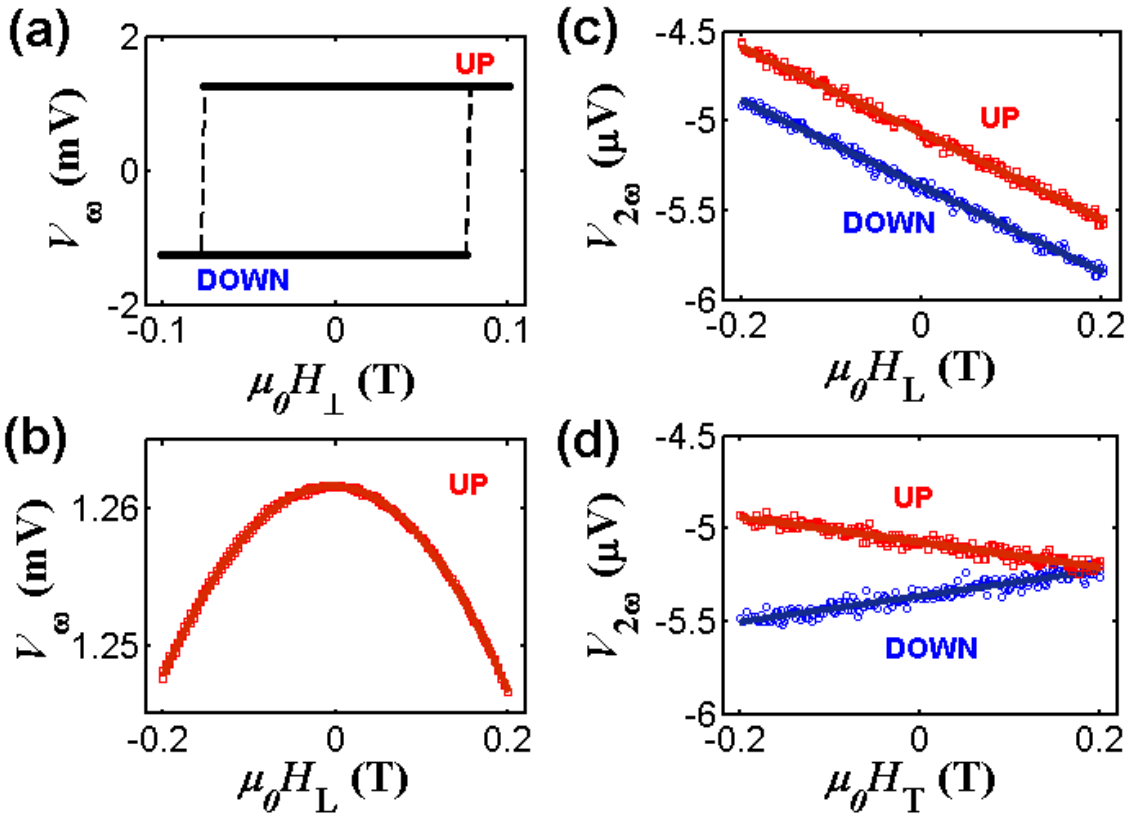

Figure 3.1: Typical first- and second-harmonic transverse voltages versus sweeping external field ***H***, taken from the Pt(6)/Co(1) sample. (a) Field-switching behavior when ***H*** is swept perpendicularly to the sample plane. The dashed line connects the data points. (b) First-harmonic response when ***H*** is swept along the current direction. (c, d) Second-harmonic response when ***H*** is swept along (c) and transverse (d) to the current. The solid lines in (b, c, d) show the fitted results.

A more convenient way to investigate the results is to consider the spin torque efficiency per applied electric field defined as

$$\xi_{\mathrm{DL}}^{E} \equiv (2e/\hbar)\, j_{\mathrm{SHE}} T_{\mathrm{int}} / E = \sigma_{\mathrm{SH}} T_{\mathrm{int}} = \xi_{\mathrm{DL}}^{j} / \rho \qquad (3.4)$$

which is expected to have little dependence on the NM resistivity, provided that the intrinsic and/or side-jump SHE is dominant for Pt, because in these cases the spin Hall conductivity $\sigma_{\mathrm{SH}} \equiv (2e/\hbar)\, j_{\mathrm{SHE}} / E = \theta_{\mathrm{SH}} / \rho$ is an intrinsic property of the NM. If we make the additional assumption that the spin transparency of the Pt alloy/Co interface is determined solely by a diffusive spin backflow effect [28,29] then the thickness- and resistivity-dependent $\xi_{\mathrm{DL}}^{E}(\rho_{\mathrm{PtX}}, t_{\mathrm{PtX}})$ should given by [21]

$$\xi_{\mathrm{DL}}^{E}(\rho_{\mathrm{PtX}}, t_{\mathrm{PtX}}) = \sigma_{\mathrm{SH}} \left(1 - \mathrm{sech}(t_{\mathrm{PtX}} / \lambda_{\mathrm{s}})\right) \left(1 + \frac{\tanh(t_{\mathrm{PtX}} / \lambda_{\mathrm{s}})}{2\lambda_{\mathrm{s}} \rho_{\mathrm{PtX}} G_{r}}\right)^{-1} \qquad (3.5)$$

where G_r is the real part of the spin mixing conductance [29] and where we assume the its imaginary counterpart is negligible, and λ_s is the spin diffusion length which varies inversely with resistivity within the Elliott-Yafet spin scattering mechanism [30,31]. It is then readily understood from Eq. (3.5) that in the ideal case of constant spin Hall conductivity and constant interface transparency there should be a slight initial increase of the calculated ξ_{DL}^{E} with increasing alloy concentration due to changes in the effective spin diffusion length as a function of $r_{\mathrm{PtX}}^{\mathrm{avg}}$, with the ratio of the spin diffusion length to the HM layer thickness determining the degree to which the calculated value of ξ_{DL}^{E} approaches the saturated value. This predicted small increase in ξ_{DL}^{E} is opposite to what is observed, as ξ_{DL}^{E} decreases with increasing alloy concentration by as much as 30% for $Pt_{100-x}Al_x$ and 40% for $Pt_{100-x}Hf_x$ as shown in Fig. 3.2(c).

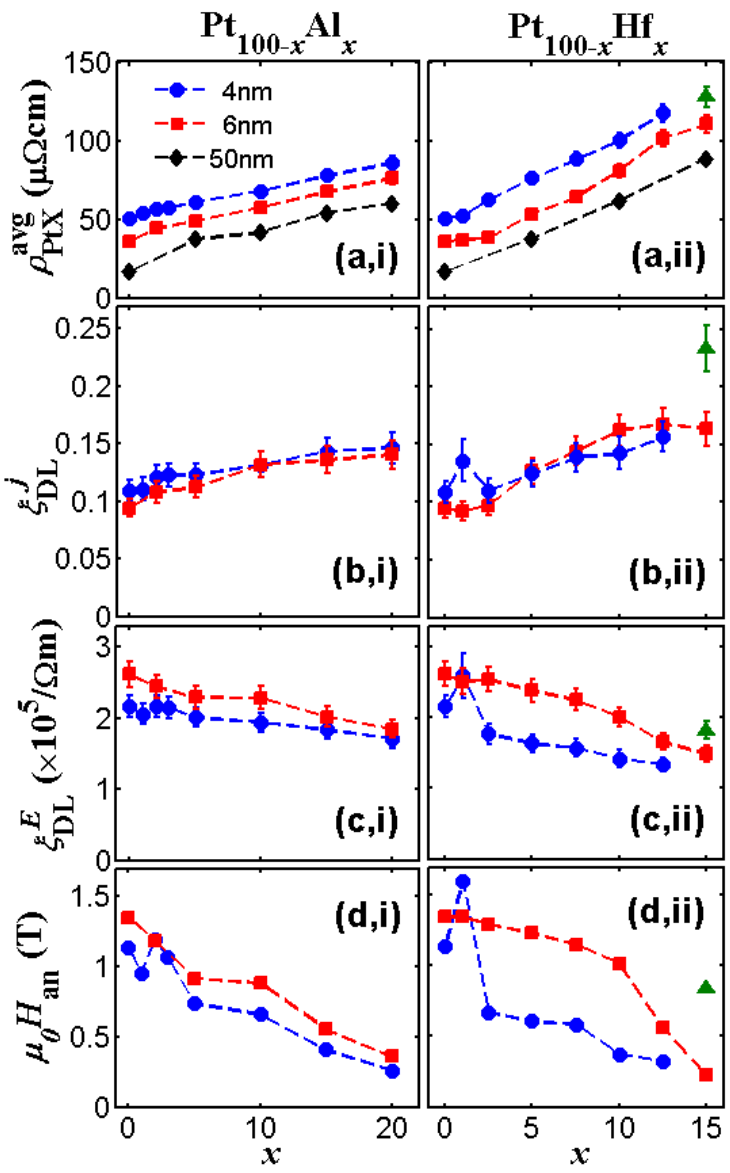

Figure 3.2: The averaged resistivity **(a)** of the 4 nm (blue circles), 6 nm (red squares), and 50 nm (black diamonds) HM films; the damping-like spin torque efficiency per unit (averaged) current density **(b)** and per unit applied electric field **(c)**, and the anisotropy field **(d)** determined from harmonic response measurements of 4 nm (blue circles) and 6 nm (red squares) HM films versus alloy concentration x for **(i)** HM = $Pt_{100-x}Al_x$ and **(ii)** HM = $Pt_{100-x}Hf_x$. The green triangles in **(ii)** show the results for the $Pt_{85}Hf_{15}$(5.5)/Pt(0.5)/Co sample. The dashed lines guide the eye by connecting the data points.

Possible explanations for the experimentally observed decline of ξ_{DL}^{E} with increasing alloy concentration include: (1) a reduction in the spin current transparency T_{int} of the Pt(X)/FM interface that becomes stronger with x, and (2) a growing detrimental distortion of the band structure from that of pure Pt [32] that might lower the spin Hall conductivity of the alloy. A third possibility would be that the SHE in Pt is dominated by the skew-scattering mechanism, but in that case σ_{SH} (and therefore $\xi_{DL}^{E} = \sigma_{SH} T_{int}$) should vary inversely with ρ_{PtX} and $\xi_{DL}^{j} = \xi_{DL}^{E} \cdot \rho_{PtX}^{avg}$ should be constant. Instead we see that χ_{DL}^{j} increases, albeit sub-linearly, with ρ_{PtX}^{avg}. To examine the questions of whether alloying might impair T_{int} and whether it is possible to improve the interfacial transparency, we grew another sample with HM = $Pt_{85}Hf_{15}$(5.5) | Pt(0.5), *i.e.*, we replaced a thin 0.5 nm alloy layer next to the HM/FM interface with pure Pt. The results from the insertion layer sample are also shown in Fig. 3.2 (green triangles) and compared to Pt(6)/Co and $Pt_{85}Hf_{15}$(6)/Co samples in Table 3.1. The resistivity of the $Pt_{85}Hf_{15}$(5.5) | Pt(0.5) | Co sample, as averaged over the total 6 nm thickness of the HM layer, shows a small increase in comparison to that of $Pt_{85}Hf_{15}$/Co sample. We tentatively attribute this to additional scattering at the additional $Pt_{85}Hf_{15}$(5.5)/Pt(0.5) interface. With the addition of the Pt(0.5) insertion layer, ξ_{DL}^{E} increases from 1.5×10^{5} / Ωm for the $Pt_{85}Hf_{15}$(6)/Co sample to 1.8×10^{5} / Ωm for $Pt_{85}Hf_{15}$(5.5) | Pt(0.5) | Co which we ascribe to the improvement of the interfacial transparency. With respect to the spin torque efficiency per unit current density the Pt(0.5) insertion layer resulted in a remarkably high value $\xi_{DL}^{j} = 0.23 \pm 0.02$, about 2 times larger than that of the Pt(6)/Co bilayer. Not only is the torque efficiency per unit applied current density improved, but so is the power required for switching, even though the resistivity of the HM is increased. If J_c is the switching current density in the HM, the power dissipated in the HM for switching $J_c^2 \rho_{HM}^{avg} \propto \rho_{HM}^{avg} / \left(\xi_{DL}^{j}\right)^2 = 1/\left(\xi_{DL}^{j} \cdot \xi_{DL}^{E}\right)$ is

reduced by nearly a factor of 2, from $\approx 4.3\times10^{-5}\,\Omega$m for Pt(6)/Co to $\approx 2.4\times10^{-5}\,\Omega$m for $Pt_{85}Hf_{15}$(5.5)/Pt(0.5)/Co. These results for the $Pt_{85}Hf_{15}$(5.5) | Pt(0.5) | Co sample demonstrate that the high spin Hall conductivity of the $Pt_{85}Hf_{15}$ alloy, while it may be somewhat less than that of pure Pt, can result in a large spin torque efficiency, provided it is employed in combination with a very thin Pt spacer to at least partially restore the interfacial spin transparency to that of a simple Pt/Co interface.

Strong effects of alloying on the HM/FM interface are also evident from changes in the interfacial magnetic anisotropy. Figure 3.1(d) shows the anisotropy field, obtained from the harmonic response measurement by Eq. (3.1), versus the alloy concentration. The anisotropy field decreases quickly with increasing alloy concentration for both the Al and Hf cases, and the samples lose their PMA for alloy concentrations larger than those shown in Fig. 3.2. With the insertion of the 0.5 nm Pt spacer layer, the PMA is partially restored (Fig. 3.2(d,ii)). We conclude from these observations that the alloying has a negative effect on the HM/FM interface in a way that both significantly reduces the anisotropy field and also reduces the spin transparency of the interface. We speculate that these effects might be the result of partial segregation of the Al and Hf impurities to the interface that can be inhibited by the presence of the Pt spacer layer.

Table 3.1: The averaged resistivity (averaging over the total 6 nm thick HM layer), anisotropy field, spin torque efficiency per applied electric field and per applied current density for Pt(6)/Co, $Pt_{85}Hf_{15}$(6)/Co and $Pt_{85}Hf_{15}$(5.5)/Pt(0.5)/Co samples.

SAMPLE	Pt(6)/Co	$Pt_{85}Hf_{15}$(6)/Co	$Pt_{85}Hf_{15}$(5.5)/Pt(0.5)/Co
ρ_{HM}^{avg} ($\mu\Omega\cdot$cm)	36 ± 2	110 ± 6	128 ± 7
$\mu_0 H_{an}$ (T)	2.2	0.23	0.84
ξ_{DL}^{E} ($\times 10^5$ / Ωm)	2.6 ± 0.2	1.5 ± 0.1	1.8 ± 0.1
ξ_{DL}^{j}	0.09 ± 0.01	0.16 ± 0.01	0.23 ± 0.02

In summary, we have demonstrated a simple but effective method that utilizes the intrinsic nature of the spin Hall effect in Pt (and Pt alloys) to enhance the spin torque efficiency of Pt by alloying with either Al or Hf. The averaged resistivity of the HM layer increases almost linearly with the alloy concentration but the spin torque efficiency per unit applied electric field decreases, which we attribute at least in part to a degraded spin transparency of the HM/FM interface. The alloying also degrades the strength of interfacial magnetic anisotropy. The interfacial spin transparency and the PMA can both be significantly restored by the insertion of a very thin (0.5 nm) pure Pt layer between the alloy and FM layers. We have achieved large spin torque efficiencies per unit current density of 0.14 for $Pt_{80}Al_{20}$/Co, 0.16 for $Pt_{100-x}Hf_x$/Co (x = 10 - 15), and 0.23 ± 0.02 for $Pt_{85}Hf_{15}$(5.5)/Pt(0.5)/Co samples. These values are much higher than those previously reported for pure Pt in similar multilayer systems.

We thank T. Phung and S. Parkin of IBM for a fruitful discussion. This work was supported in part by the Samsung Electronics Corporation, by the NSF/MRSEC program (DMR-1120296) through the Cornell Center for Materials Research, and by the Office of Naval Research. We also acknowledge support from the NSF (Grant No. ECCS-1542081) through use of the Cornell Nanofabrication Facility/National Nanofabrication Infrastructure Network.

REFERENCES

[1] M. I. Dyakonov and V. I. Perel, Phys. Leters **35A**, 459 (1971).

[2] J. Hirsch, Phys. Rev. Lett. **83**, 1834 (1999).

[3] S. Zhang, Phys. Rev. Lett. **85**, 393 (2000).

[4] L. Liu, T. Moriyama, D. C. Ralph, and R. A. Buhrman, Phys. Rev. Lett. **106**, 036601 (2011).

[5] L. Liu, C.-T. Chen, and J. Z. Sun, Nat. Phys. **10**, 561 (2014).

[6] M.-H. Nguyen, C.-F. Pai, K. X. Nguyen, D. A. Muller, D. C. Ralph, and R. A. Buhrman, Appl. Phys. Lett. **106**, 222402 (2015).

[7] W. Zhang, W. Han, X. Jiang, S.-H. Yang, and S. S. P. Parkin, Nat. Phys. **11**, 496 (2015).

[8] C.-F. Pai, Y. Ou, L. H. Vilela-Leão, D. C. Ralph, and R. A. Buhrman, Phys. Rev. B **92**, 064426 (2015).

[9] L. Liu, C.-F. Pai, Y. Li, H. W. Tseng, D. C. Ralph, and R. A. Buhrman, Science **336**, 555 (2012).

[10] C.-F. Pai, L. Liu, Y. Li, H. W. Tseng, D. C. Ralph, and R. A. Buhrman, Appl. Phys. Lett. **101**, 122404 (2012).

[11] Y. Niimi, Y. Kawanishi, D. H. Wei, C. Deranlot, H. X. Yang, M. Chshiev, T. Valet, A. Fert, and Y. Otani, Phys. Rev. Lett. **109**, 156602 (2012).

[12] Y. Niimi, M. Morota, D. H. Wei, C. Deranlot, M. Basletic, A. Hamzic, A. Fert, and Y. Otani, Phys. Rev. Lett. **106**, 126601 (2011).

[13] A. Fert and P. M. Levy, Phys. Rev. Lett. **106**, 157208 (2011).

[14] Y. Niimi, H. Suzuki, Y. Kawanishi, Y. Omori, T. Valet, A. Fert, and Y. Otani, Phys. Rev. B **89**, 054401 (2014).

[15] P. Laczkowski, J.-C. Rojas-Sánchez, W. Savero-Torres, H. Jaffrès, N. Reyren, C. Deranlot, L. Notin, C. Beigné, A. Marty, J.-P. Attané, L. Vila, J.-M. George, and A. Fert, Appl. Phys. Lett. **104**, 142403 (2014).

[16] L. K. Zou, S. H. Wang, Y. Zhang, J. R. Sun, J. W. Cai, and S. S. Kang, Phys. Rev. B **93**, 014422 (2016).

[17] T. Tanaka, H. Kontani, M. Naito, T. Naito, D. Hirashima, K. Yamada, and J. Inoue, Phys. Rev. B **77**, 165117 (2008).

[18] H. Kontani, T. Tanaka, D. S. Hirashima, K. Yamada, and J. Inoue, Phys. Rev. Lett. **102**, 016601 (2009).

[19] A. Hoffmann, IEEE Trans. Magn. **49**, 5172 (2013).

[20] G. Vignale, J. Supercond. Nov. Magn. **23**, 3 (2010).

[21] M.-H. Nguyen, D. C. Ralph, and R. A. Buhrman, Phys. Rev. Lett. **116**, 126601 (2016).

[22] G. Guo, S. Murakami, T.-W. Chen, and N. Nagaosa, Phys. Rev. Lett. **100**, 096401 (2008).

[23] M. Morota, Y. Niimi, K. Ohnishi, D. H. Wei, T. Tanaka, H. Kontani, T. Kimura, and Y. Otani, Phys. Rev. B **83**, 174405 (2011).

[24] M. Isasa, E. Villamor, L. E. Hueso, M. Gradhand, and F. Casanova, Phys. Rev. B **91**, 024402 (2015).

[25] J. M. Shaw, H. T. Nembach, T. J. Silva, S. E. Russek, R. Geiss, C. Jones, N. Clark, T. Leo, and D. J. Smith, Phys. Rev. B **80**, 184419 (2009).

[26] J. Kim, J. Sinha, M. Hayashi, M. Yamanouchi, S. Fukami, T. Suzuki, S. Mitani, and H. Ohno, Nat. Mater. **12**, 240 (2013).

[27] C. O. Avci, K. Garello, M. Gabureac, A. Ghosh, A. Fuhrer, S. F. Alvarado, and P. Gambardella, Phys. Rev. B **90**, 224427 (2014).

[28] Y.-T. Chen, S. Takahashi, H. Nakayama, M. Althammer, S. Goennenwein, E. Saitoh, and G. Bauer, Phys. Rev. B **87**, 144411 (2013).

[29] P. M. Haney, H.-W. Lee, K.-J. Lee, A. Manchon, and M. D. Stiles, Phys. Rev. B **87**, 174411 (2013).

[30] R. J. Elliott, Phys. Rev. **96**, 266 (1954).

[31] Y. Yafet, Solid State Phys. **14**, 1 (1963).

[32] T. Mizoguchi and N. Arakawa, Phys. Rev. B **93**, 041304(R) (2016).

CHAPTER 4

Enhancement of the Anti-Damping Spin Torque Efficacy of Platinum by Interface Modification

Minh-Hai Nguyen[1], Chi-Feng Pai[1], Kayla X. Nguyen[1],

David A. Muller[1,2], D. C. Ralph[1,2], R. A. Buhrman[1]

[1]*Cornell University, Ithaca, New York 14853, USA*

[2]*Kavli Institute at Cornell, Ithaca, New York 14853, USA*

(Published: Applied Physics Letters **106**, 222402 on 2 June 2015)

ABSTRACT

We report a strong enhancement of the efficacy of the spin Hall effect (SHE) of Pt for exerting anti-damping spin torque on an adjacent ferromagnetic layer by the insertion of ≈ 0.5 nm layer of Hf between a Pt film and a thin, ≤ 2 nm, $Fe_{60}Co_{20}B_{20}$ ferromagnetic layer. This enhancement is quantified by measurement of the switching current density when the ferromagnetic layer is the free electrode in a magnetic tunnel junction. The results are explained as the suppression of spin pumping through a substantial decrease in the effective spin-mixing conductance of the interface, but without a concomitant reduction of the ferromagnet's absorption of the SHE generated spin current.

MAIN TEXT

The experimental determination that a current density J_e flowing through certain high-atomic-number metals can generate a quite substantial transverse spin current density J_s through the spin Hall effect (SHE) [1–3] has been a major factor in the recent focus on the study of spin-orbit interaction effects in heavy metal - ferromagnet (HM|FM) thin film multilayer systems. The fraction of this spin current that is absorbed by the ferromagnetic film generates a spin transfer torque on the FM, characterized by a spin-torque efficiency $\xi_{\mathrm{SH}} \equiv \left(2e/\hbar\right) J_s^{\mathrm{absorbed}} / J_e \leq \theta_{\mathrm{SH}} \equiv \left(2e/\hbar\right) J_s / J_e$, where θ_{SH} is the "internal" spin Hall angle. For anti-damping spin-torque (ST) excitation, the mechanism by which the spin Hall torque can achieve magnetic manipulation using the least possible current, the critical current density scales $\propto \alpha / \xi_{\mathrm{SH}}$ and the write energy $\propto \left(\alpha / \xi_{\mathrm{SH}}\right)^2 \rho$, where a is the Gilbert damping of the FM|HM bilayer and r is the electrical resistivity of the HM. Large ST efficiencies have been measured for Pt, beta-phase or amorphous Ta, and beta-phase W films: $\xi_{\mathrm{SH}}^{\mathrm{Pt}} = 0.04 - 0.09$ [4–6], $\xi_{\mathrm{SH}}^{\beta-\mathrm{Ta}} \approx 0.12$ [7] and $\xi_{\mathrm{SH}}^{\beta-\mathrm{W}} \approx 0.3$ [8]. The large values of ξ_{SH} for β-Ta and β-W, together with the relatively small values of damping for thin β-Ta and β-W|FM bilayers has enabled low-current ST switching and ST microwave excitation of the free electrode of nanoscale magnetic tunnel junctions (MTJs) [8], demonstrating the feasibility of the SHE for three-terminal memory device and ST nano-oscillator applications [9–11] as well as new classes of spin logic circuits [12–17]. However, the high resistivity of β-Ta and β-W, $\geq 180\ \mu\Omega\cdot\mathrm{cm}$, can be problematic when the write energy and device heating are important considerations. While the lower resistivity of Pt films, $r_{\mathrm{Pt}} \gg 20\ \mu\Omega\times\mathrm{cm}$ for isolated films (which can be different from the averaged resistivity of thin Pt having adjoining metal layers of high resistivity) (see Supplemental Information - SI), makes Pt seemingly more attractive for energy-

efficient ST devices, the smaller value of ξ_{SH} for Pt and a much higher damping for FM|Pt bilayers [4,7] greatly diminishes the effectiveness of anti-damping ST for Pt devices.

Recent works [18–20] have shown strong and complicated effects of a thin insertion layer on the spin orbit torques in HM|FM systems. Here we report that a thin, ≈ 0.5 nm , Hf layer inserted between a Pt film and a thin $Fe_{60}Co_{20}B_{20}$ (FeCoB) layer causes large reductions in both the current density and write energy needed for ST switching. The presence of the Hf reduces the Gilbert damping a by more than a factor of two by suppressing spin pumping, and at the same time results in $\xi_{SH}^{Pt|Hf} \approx 0.12$, approximately 2 times higher than the spin torque efficiency reported with $Pt|Ni_{81}Fe_{19}$ bilayers. Pt|Hf|FeCoB is therefore a preferred SHE structure for use in anti-damping ST applications. Our work suggests that there may be additional opportunities for the enhancement of spin Hall torque effects through the further optimized modification of HM|FM interfaces.

Understanding the consequences of the Hf insertion layer requires an analysis of the processes contributing to magnetic damping and spin transmission at an HM|FM interface. The phenomenon of spin pumping, which is typically analyzed via use of the drift-diffusion equation, [21] increases the magnetic damping a in HM|FM structures compared to α_0, the intrinsic damping parameter in the absence of the HM, because the precession of the FM magnetization leads to a loss of spin angular momentum in the HM [22] resulting in:

$$\alpha = \alpha_0 + \frac{\gamma \hbar^2}{2e^2 M_s t_{FM}} G_{eff}^{\uparrow\downarrow}. \qquad (4.1)$$

Here $\gamma = 1.76 \times 10^{11}$ HzT^{-1} is the gyromagnetic ratio, M_s is the saturation magnetization of the FM, t_{FM} is the thickness of the FM layer, and $G_{eff}^{\uparrow\downarrow}$ is the "effective spin-mixing conductance" of the HM|FM interface. $G_{eff}^{\uparrow\downarrow}$ can be expressed in terms of the bare spin mixing conductance of the

interface $G^{\uparrow\downarrow}$ (here we are assuming that $\left|\mathrm{Re}\,G^{\uparrow\downarrow}\right| >> \left|\mathrm{Im}\,G^{\uparrow\downarrow}\right|$ [23]), and the spin conductance of the HM layer, $G_{\mathrm{ext}} \equiv \tanh(t_{\mathrm{HM}} / \lambda_{\mathrm{s}}) / (2\rho_{\mathrm{HM}}\lambda_{\mathrm{s}})$, as [23–26]

$$G_{\mathrm{eff}}^{\uparrow\downarrow} = \frac{G^{\uparrow\downarrow}}{1 + G^{\uparrow\downarrow} / G_{\mathrm{ext}}} . \tag{4.2}$$

Pt has a relatively large value of $G_{\mathrm{eff}}^{\text{-}-}$ and is therefore a good "spin sink", since the typical resistivity of Pt films, $\rho_{\mathrm{Pt}} \approx 20 - 25\,\mu\Omega\cdot\mathrm{cm}$ in combination with a spin attenuation length $\lambda_{\mathrm{s}}^{\mathrm{Pt}} \approx 1.2 - 1.4\,\mathrm{nm}$ [27,28] results in $G_{\mathrm{ext}} \approx 1.8\times10^{15}\ \Omega^{-1}\mathrm{m}^{-2}$ (assuming $t_{\mathrm{HM}} >> \lambda_{\mathrm{s}}$), while the bare mixing conductance of common Pt|FM interfaces is usually of a similar value, *e.g.* $G^{\uparrow\downarrow} \approx 1.2\times10^{15}\ \Omega^{-1}\mathrm{m}^{-2}$ has been reported [28] for Pt|Py (Py=$Ni_{81}Fe_{19}$). Consequently, $G_{\mathrm{eff}}^{\uparrow\downarrow}$ for Pt|FM bilayers is considerably higher, $\geq 0.7\times10^{15}\ \Omega^{-1}\mathrm{m}^{-2}$, than that found, for example, for the *β*-W|FeCoB system, $0.16\times10^{15}\ \Omega^{-1}\mathrm{m}^{-2}$ [29]. When t_{FM} is small, as it must be in ST devices, the large value of $G_{\mathrm{eff}}^{\uparrow\downarrow}$ causes a large increase in a above a_0 for Pt|FM bilayers (*e.g.*, more than a factor of 4 for a 1.8 nm FeCoB layer, see below). This greatly reduces the efficacy of Pt for anti-damping ST applications, although the SHE of Pt is still quite effective for driving the displacement of domain walls in perpendicularly magnetized free layers where the increased damping is not an issue [30,31].

Turning to the spin torque efficiency ξ_{SH}, this is of course affected by the net interfacial spin transmissivity in the opposite direction, that is by the extent to which spin currents generated by the SHE in the HM are transmitted through the HM|FM interface to exert a spin torque on the FM. The drift-diffusion analysis for this situation [23,24] indicates that unless $\mathrm{Re}\,G^{\uparrow\downarrow} >> G_{\mathrm{ext}}$ there will be substantial spin back-flow from the interface, which reduces the efficiency of the SHE

(relative to the internal spin Hall angle, θ_{SH}) in exerting a damping-like spin torque on the FM:

$$\xi_{SH} = \theta_{SH} \times \frac{G^{\uparrow\downarrow} \tanh\left(\frac{t_{HM}}{2\lambda_s}\right)\tanh\left(\frac{t_{HM}}{\lambda_s}\right)}{G^{\uparrow\downarrow} + G_{ext}} = \theta_{SH} \times \frac{G_{eff}^{\uparrow\downarrow}}{G_{ext}} \tanh\left(\frac{t_{HM}}{2\lambda_s}\right)\tanh\left(\frac{t_{HM}}{\lambda_s}\right). \quad (4.3)$$

This reduction can be quite significant. For example, applying the analysis above to the Pt|Py interface yields $\xi_{SH} \approx 0.25\ \theta_{SH}^{Pt}$ indicating that the lower bound of $\xi_{SH} \approx 0.05$ as established by the ST ferromagnetic resonance (ST-FMR) study of Pt|Py bilayers of Liu *et al.* [4,27] is considerably lower than the actual internal spin Hall angle of the Pt film $\theta_{SH}^{Pt} \approx 0.20$ [32]. This is similar to the result of the same analysis applied to Pt|Co and Pt|CoFe interfaces [33]. This analysis suggests that by an appropriate choice of materials and control of the interface structure, we could possibly achieve higher ST efficiencies, and indeed recent studies using different Pt|FM combinations have reported $\xi_{SH} \approx 0.1$ in some cases [32,33].

With the objective of investigating means to suppress spin-pumping and to enhance, or at least not degrade, the spin torque efficiency of Pt for MTJ switching applications, we produced ||Ta(1) | Pt(4) | Hf(t_{Hf}) | FeCoB(t_{FeCoB}) | MgO(1.6) | Ru(2) and ||Ta(1) | Pt(4) | Hf(t_{Hf}) | FeCoB(t_{FeCoB}) | MgO(1.6) | FeCoB(4) | Hf(5) | Ru(5) multilayer films (see SI) (Here || represents the thermally-oxidized Si substrate and the numbers in parentheses are thicknesses in nm). The high resistivity Ta was used for adhesion and smoothing purposes, while Hf was chosen for this investigation because initial ferromagnetic resonance studies (FMR) studies indicated a low $G_{eff}^{\uparrow\downarrow}$ for Hf|FeCoB and previous work has demonstrated that there are negligible current-induced spin-orbit torques produced at Hf|FM interfaces [34]. The Hf thickness t_{Hf} was varied in fine steps from 0.33 to 0.76 nm with a relative uncertainty of 5%, while the FeCoB layer thicknesses t_{FeCoB} were

1.6 and 1.8 nm. We also fabricated and measured control samples with $t_{Hf} = 0$ (i.e., no Hf spacer). The samples were annealed at 300 C for 30 minutes in a background pressure $< 10^{-7}$ Torr .

Since certain transition metal elements when incorporated into magnetic tunnel junction structures can be quite mobile, either during deposition and subsequent annealing steps, we investigated this possibility with respect to the Hf insertion layer by using electron energy loss spectroscopy (EELS) [35] to study the spatial-dependent composition of some of our samples in a 100 keV Nion UltraSTEM. Fig. 4.1 shows the EELS data for a $t_{FeCoB} = 1.6$ nm , $t_{Hf} = 0.5$ nm sample. Since the obtained intensity is proportional to the relative distribution of the element, it is readily seen that a portion of Hf has diffused through the FeCoB layer into the MgO layer, where it is now oxidized. By integrating over the intensity, the amount of Hf in between the Pt and FeCoB layers is estimated to be ~70% of the total amount of Hf deposited which corresponds to a thickness of ~0.35 nm for this nominal 0.5 nm Hf sample. This indicates that a thin, conformal and continuous Hf spacer of approximately two atomic layers or so in thickness is formed on the surface of Pt layer, which is consistent with the high (negative) formation enthalpy of HfPt compounds [36,37].

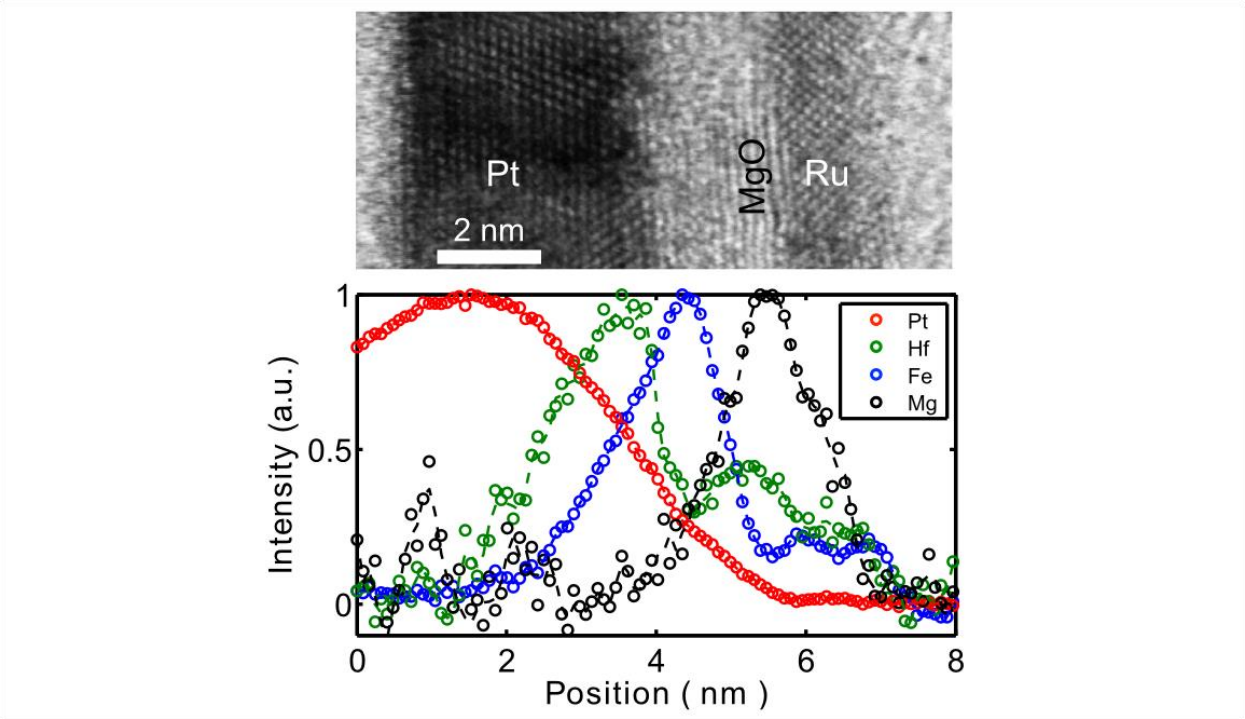

Figure 4.1. ABF-STEM (annular bright field - scanning transmission electron microscopy) image of ||Ta(1) | Pt(4) | Hf(0.5) | FeCoB(1.6) | MgO(1.6) | Ru(2) sample and the corresponding EELS line profile that shows Hf diffusion through the FeCoB into the MgO.

The magnetic properties of the FeCoB layer in the first set of multilayers were characterized by SQUID magnetometry and anomalous Hall measurements (see SI) which indicated a saturation magnetization $M_s = (1.56 \pm 0.06) \times 10^6$ A/m, and also an apparent "magnetic dead layer" thickness $t_d = 0.7 \pm 0.1$ nm. By fitting the data from measurement of the effective magnetic anisotropy energy $K_{\text{eff}} t_{\text{FeCoB}}^{\text{eff}}$ as a function of FeCoB effective thickness $t_{\text{FeCoB}}^{\text{eff}} = t_{\text{FeCoB}} - t_d$ to the standard model for the thickness dependence of the magnetic anisotropy [38]

$$K_{\text{eff}} t_{\text{FeCoB}}^{\text{eff}} = \left(K_V - (1/2)\mu_0 M_s^2 \right) t_{\text{FeCoB}}^{\text{eff}} + K_S \tag{4.4}$$

the interface and bulk anisotropy energy densities are estimated to be $K_S = 0.45 \pm 0.03$ mJ/m^2 and $K_V = 0.60 \pm 0.03$ MJ/m^3, respectively. This value of K_S is smaller than typical for Ta|FeCoB|MgO multilayers, while K_V is similar to a recent report [39].

Finally, measurements of the in-plane effective demagnetization field $\mu_0 M_{\text{eff}}$ for $t_{\text{FeCoB}} = 1.6$ nm and $t_{\text{FeCoB}} = 1.8$ nm ||Ta(1)|Pt(4)|Hf(t_{Hf})|FeCoB(t_{FeCoB})|MgO(1.6)|Ru(2) samples indicated that the insertion of a thin layer Hf at the interface of Pt and FeCoB has a significant effect on $\mu_0 M_{\text{eff}}$, with a local *minimum* at $t_{\text{Hf}} = 0.5$ nm for both series (see SI). We tentatively attribute this behavior to the role of the Hf insertion layer in both reducing the positive volume anisotropy effect from elastic strain from the underlying Pt, and in enhancing the surface anisotropy energy through reduction of strain at the FeCoB|MgO interface.

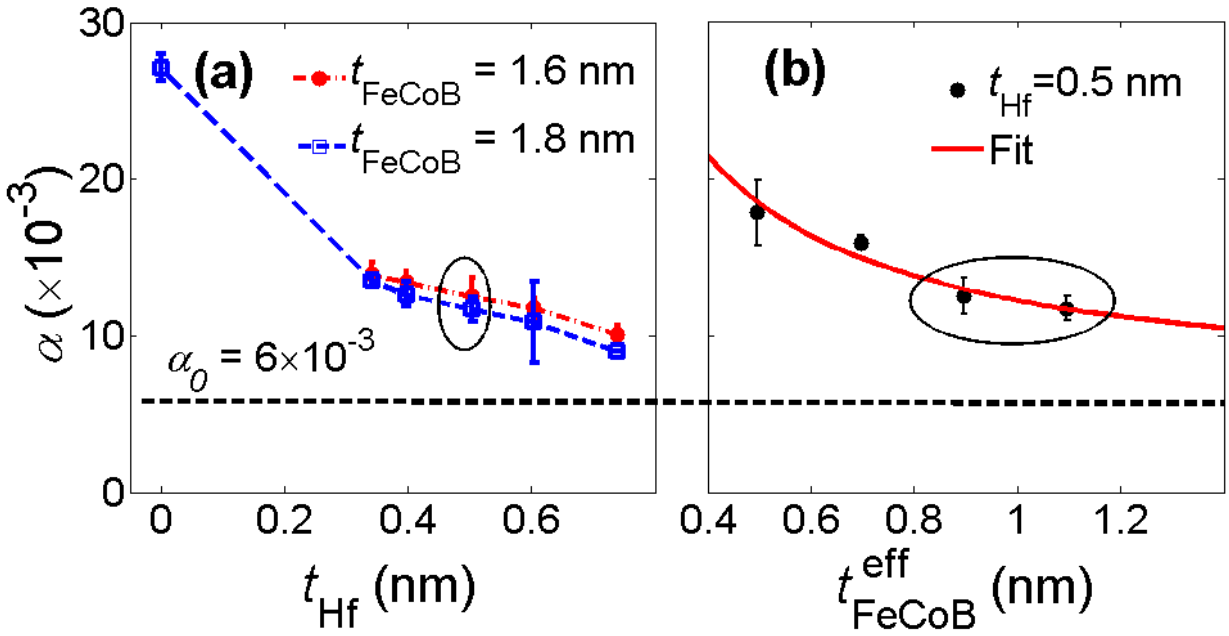

Figure 4.2. Gilbert damping parameter α of ||Ta(1) | Pt(4) | Hf(t_{Hf}) | FeCoB(t_{FeCoB}) | MgO(1.6) samples measured by frequency-dependent ST-FMR. (**a)** Damping parameter versus Hf thickness t_{Hf} for the $t_{FeCoB} = 1.6$ nm (circles) and $t_{FeCoB} = 1.8$ nm (squares) samples. The horizontal broken line indicates the fitted damping parameter (0.006) for an isolated FeCoB layer. **(b)** Damping parameter versus FeCoB effective thickness of the $t_{Hf} = 0.5$ nm samples. The solid line shows the fitting result from which the magnetic damping parameter of isolated FeCoB film is estimated. The ellipses in **(a)** and **(b)** indicate the same data points.

In Fig. 4.2(a) we show $\alpha(t_{\mathrm{Hf}})$, determined by frequency-dependent ST-FMR measurements (see SI), for the two different FeCoB thicknesses, 1.6 nm and 1.8 nm with the results clearly demonstrating that a deposited Hf layer as thin as 0.35 nm, or even less, is effective in greatly reducing the spin-pumping-induced increase in a. All of the samples with the Hf insertion layer exhibit a decrease in a by a factor of two or more compared to Pt|FeCoB(1.8 nm) with no insertion layer (also shown in Fig. 4.2(a)). We quantified the effect of the 0.5 nm Hf insertion layer on $G_{\mathrm{eff}}^{\uparrow\downarrow}$ of a series of $t_{\mathrm{Hf}} = 0.5\,\mathrm{nm}$ samples as the function of $t_{\mathrm{FeCoB}}^{\mathrm{eff}}$. Fig. 4.2(b) shows the best fit to the damping coefficient $a(t_{\mathrm{FeCoB}}^{eff})$ data (solid line in Fig. 4.2(b)) to equation (4.1) which yields $\alpha_0 \approx 0.006$ (broken line) and $G_{\mathrm{eff}}^{\uparrow\downarrow} \approx 0.24\times10^{15}\ \Omega^{-1}\mathrm{m}^{-2}$. This $G_{\mathrm{eff}}^{\uparrow\downarrow}$ value is nearly as low as the value $0.16\times10^{15}\ \Omega^{-1}\mathrm{m}^{-2}$ observed in the β-W|FeCoB system [29]. Similar measurements made on a series of $t_{\mathrm{Hf}} = 0$ control samples (see SI) yielded $G_{\mathrm{eff}}^{\uparrow\downarrow} \approx (1.1 \pm 0.1)\times10^{15}\ \Omega^{-1}\mathrm{m}^{-2}$, similar, although somewhat higher, than the previous results for Pt|$Ni_{81}Fe_{19}$, confirming the strong effectiveness of the insertion of a nominal 0.5 nm Hf layer in suppressing spin pumping, as reflected by the large reduction of $\Delta\alpha = \alpha - \alpha_0$ shown in Fig. 4.2(a).

To determine ξ_{SH} for the Pt|Hf|FeCoB trilayers we measured the ST switching current of a FeCoB free layer in a MTJ, which is the application for which we seek to improve the spin Hall efficacy [8]. To accomplish these switching current measurements, we patterned the second set of multilayers by electron beam lithography and ion milling (described in SI) into three terminal SHE-MTJ devices which consisted of elliptical FeCoB|MgO|FeCoB MTJs, typically with lateral dimensions $\approx 50\times180\ \mathrm{nm}^2$, on top of a Ta|Pt|Hf microstrip approximately 1.2 μm wide as shown schematically in Fig. 4.3(a). The magnetization of the free FM layer could be controlled either by an in-plane external field along the major axis of the tunnel junction or a direct current through Pt

layer, and the orientation of the magnetic free layer can be determined by the differential resistance of the MTJ.

Figure 3(b)-(d) show results for $t_{\mathrm{FeCoB}} = 1.6\,\mathrm{nm}$, $t_{\mathrm{Hf}} = 0.5\,\mathrm{nm}$ devices. From the field switching behavior the coercivity $\mu_0 H_c$ is determined to be about 4.5 mT and the tunneling magnetoresistance (TMR) is 80%. Figure 4.3(b) shows the current-switching behavior for a $50 \times 180\ \mathrm{nm}^2$ MTJ, 1.2 μm channel device at a ramp rate 0.0013 mA/s, for which the switching occurs at average critical currents $I_c = \pm 0.4\,\mathrm{mA}$. The switching currents at different ramp rates are shown in Fig. 4.3(c). By fitting the data to the thermally assisted spin torque switching model [40] we find that the zero-thermal-fluctuation switching current is $I_0 = 0.71 \pm 0.08\,\mathrm{mA}$ which is, considering the geometry of the device and assuming that all current flows through the comparatively low-resistivity 4 nm Pt layer, equivalent to a current density of $J_0 = (1.5 \pm 0.2) \times 10^{11}\ \mathrm{A/m^2}$. The same measurement and analysis were also performed for $t_{\mathrm{FeCoB}} = 1.6\,\mathrm{nm}$, $t_{\mathrm{Hf}} = 0.5\,\mathrm{nm}$, $70 \times 240\ \mathrm{nm}^2$ devices with different channel widths. As shown in Fig. 4.3(d), we confirmed that the switching current I_0 varies linearly with the channel width w, as expected, and that the average zero-fluctuation switching current density $J_0 = (1.6 \pm 0.1) \times 10^{11}\ \mathrm{A/m^2}$ for that series of devices is consistent with that of the $50 \times 180\mathrm{nm}^2$ MTJ, 1.2 μm-wide channel device.

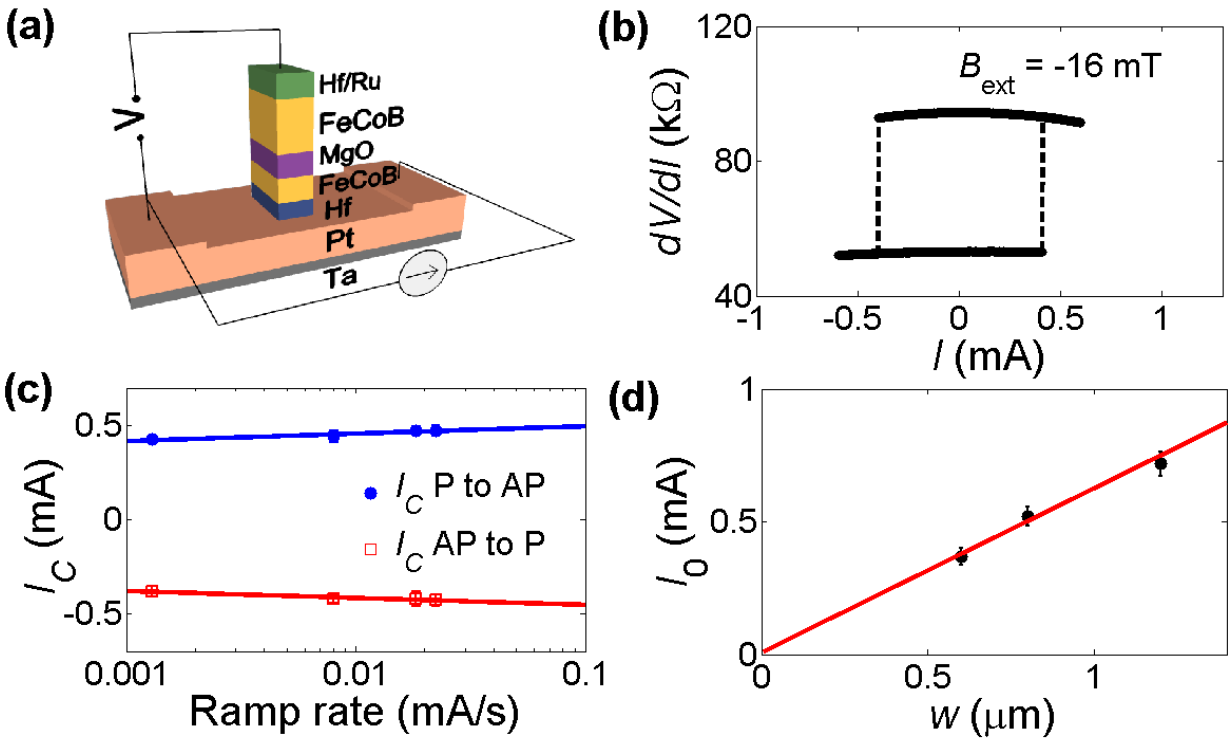

Figure 4.3. Current-induced switching behavior of ||Ta(1) | Pt(4) | Hf(0.5) | FeCoB(1.6) | MgO(1.6) | FeCoB(4) three-terminal devices. **(a)** Schematic structure of ||Ta | Pt | Hf | FeCoB | MgO | FeCoB three-terminal SHE-MTJ devices. **(b)** Differential resistance versus total current I applied to the channel at a ramp rate 0.0013 mA/s for $50 \times 180\ \mathrm{nm}^2$ MTJ with a 1.2 μm channel. The switching currents are determined to be $I_c \approx \pm 0.4\ \mathrm{mA}$. Broken lines connect the data points, indicating the magnetic switching events. **(c)** Plot of switching currents at different ramp rates of 0.0013 mA/s for a $50 \times 180\ \mathrm{nm}^2$ MTJ with a 1.2 μm channel. Solid lines show fitted results. **(d)** I_0 versus channel width w of $70 \times 240\ \mathrm{nm}^2$ devices. The linear fit (line) gives the average current density $J_0 = (1.55 \pm 0.12) \times 10^{11}\ \mathrm{A/m}^2$.

We used the results of the measurements of the switching current density J_0 as plotted in Fig. 4.4(a) as a function of t_{Hf} to calculate ξ_{SH}, using the measured values for M_{eff} and a mentioned above and the formula [8,41]

$$\xi_{\mathrm{SH}} = \frac{2e}{\hbar}\mu_0 M_s t_{\mathrm{FeCoB}}^{\mathrm{eff}} \alpha \left(H_c + \frac{M_{\mathrm{eff}}}{2} \right) / J_0 . \qquad (4.5)$$

Those latter results are plotted in Fig. 4.4(b). For $0 \le t_{\mathrm{Hf}} \le 0.6\,\mathrm{nm}$, the spin torque efficiency fluctuates about the average value $\xi_{\mathrm{SH}} = 0.10$, with a peak value $\xi_{\mathrm{SH}} = 0.12 \pm 0.02$ at both $t_{\mathrm{Hf}} = 0.0\,\mathrm{nm}$ and $t_{\mathrm{Hf}} = 0.5\,\mathrm{nm}$. While a quantitative analysis using the drift-diffusion model of these results for the spin torque efficiency of the Pt|Hf|FeCoB trilayer structures is conceptually challenging in the $t_{\mathrm{Hf}} \approx 0.5\,\mathrm{nm}$ ultrathin limit, this is less of an obvious concern for of the Pt|FeCoB bilayer samples. If we use $\rho_{\mathrm{Pt}} = 24\,\mu\Omega\cdot\mathrm{cm}$ as determined for our samples (see SI) and $\lambda_s^{\mathrm{Pt}} = 1.2$ nm [28] (determined for samples having the same electrical resistivity), we have that for the Pt layer $G_{\mathrm{ext}} = 1.7\times10^{15}\ \Omega^{-1}\mathrm{m}^{-2}$. Equations (4.2) and (4.3) then yield $G^{\uparrow\downarrow} = G_{\mathrm{ext}} G_{\mathrm{eff}}^{\uparrow\downarrow} / (G_{\mathrm{ext}} - G_{\mathrm{eff}}^{\uparrow\downarrow}) \approx 3.1\times10^{15}\ \Omega^{-1}\mathrm{m}^{-2}$ and $\chi_{\mathrm{SH}}^{\mathrm{Pt|FeCoB}} / \zeta_{\mathrm{SH}}^{\mathrm{Pt}} = 0.65$, where the latter is a considerably higher ratio than reported for a Pt|Py bilayer $\xi_{\mathrm{SH}}^{\mathrm{Pt|Py}} / \theta_{\mathrm{SH}}^{\mathrm{Pt}} = 0.25$ [32], which signifies that our Pt|FeCoB interface has a significantly higher spin current transmissivity. With $\chi_{\mathrm{SH}}^{\mathrm{Pt|FeCoB}} / \zeta_{\mathrm{SH}}^{\mathrm{Pt}} = 0.65$ the high spin torque efficiency $\chi_{\mathrm{SH}}^{\mathrm{Pt|FeCoB}} = 0.12 \pm 0.02$ obtained from the switching measurements indicates that $\theta_{\mathrm{SH}}^{\mathrm{Pt}} = 0.18 \pm 0.03$, quite consistent with the spin Hall angle values recently reported from analyzes of experiments on Pt|Py, Pt|Co and Pt|CoFe systems [32,33].

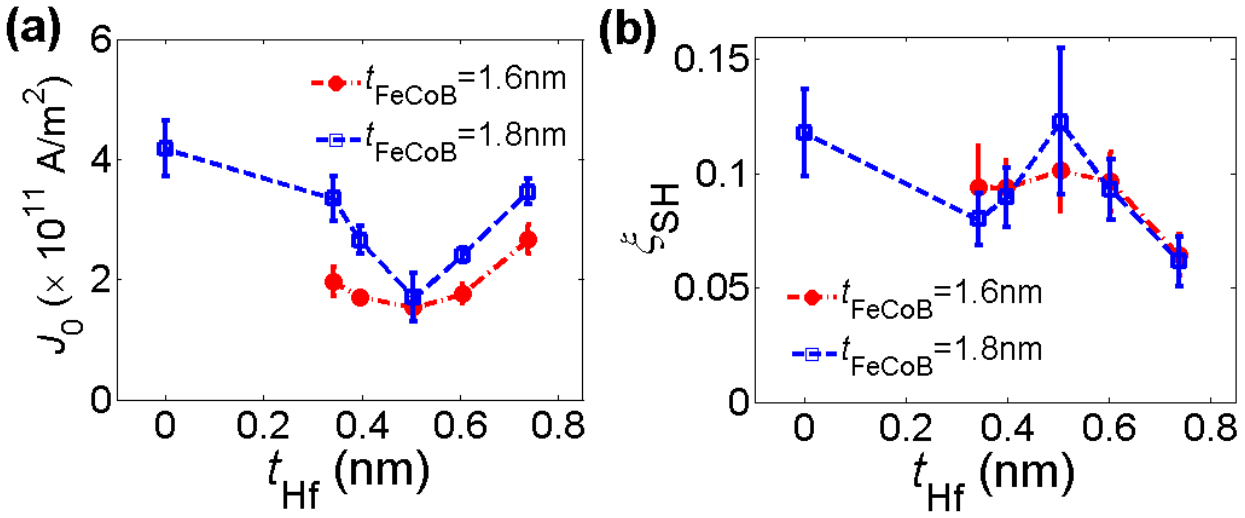

Figure 4.4. **(a)** Switching current density J_0 and **(b)** spin Hall torque efficiency ξ_{SH} versus Hf thickness for $t_{FeCoB} = 1.6$ nm (circles) and $t_{FeCoB} = 1.8$ nm (squares) samples. J_0 achieves a minimum at $t_{Hf} = 0.5$ nm. Within the uncertainty, $\xi_{SH} \approx 0.10$ for $t_{Hf} < 0.6$ nm with local maxima ≈ 0.12 at $t_{Hf} = 0$ and 0.5 nm, but then decreases for thicker Hf spacer. Dashed lines connect the data points to guide the eye.

Returning to the results from the devices with the Hf insertion layer, while the substantial decrease in ξ_{SH} when t_{Hf} is increased from 0.6 nm to 0.76 nm is perhaps qualitatively consistent with an increased attenuation of the spin current by a thicker Hf layer [34], the lack of significant variation of ξ_{SH} for $0 \leq t_{Hf} \leq 0.6\,\text{nm}$ is quite surprising in light of the strong suppression of spin pumping, which represents a factor of 4 reduction of $G_{eff}^{\uparrow\downarrow}$ by a Hf insertion only one to two atomic layers thick. Within the drift-diffusion analysis the most straightforward explanation for this spin pumping reduction is that the spin mixing conductance $G_{Hf|FeCoB}^{\uparrow\downarrow} << G_{Pt|FeCoB}^{\uparrow\downarrow}$, with the alternative being that the Hf layer has a very low spin conductance, $1/(2\rho_{Hf}\lambda_s^{Hf})$, together with $t_{Hf} \geq \lambda_s^{Hf}$. In light of the measured $\chi_{SH}(t_{Hf})$ results (Fig. 4.4(b)) there are fundamental challenges for both explanations. A low $G^{\uparrow\downarrow}$ will enhance the back flow of the spin current from the Hf|FeCoF interface, lowering ξ_{SH} as implied by equation (4.3). This could be counteracted if G_{ext} is also lowered by a similar degree by the Hf insertion, but since the experimental evidence is that Hf has no significant SHE a low $G_{ext,\,Hf}$ would also result in a strong attenuation of the spin current from the Pt before it reaches the Hf|FeCoB interface (see SI). Another possible explanation could be that the Hf insertion results in a decreased $G_{ext,\,Pt}$, or an enhanced θ_{SH}^{Pt}, through intermixing, but the similarity of the averaged resistivity of the Pt layer with and without the Hf insertion, together with results of experiments with PtHf alloys that will be reported elsewhere, appear to make this alternative explanation unlikely. Given these contradictions between the spin pumping and spin backflow (spin accumulation) predictions of the drift-diffusion equation and the results reported here, we tentatively conclude that with the very thin layers that are employed in this system, where interfacial scattering is a dominant factor, drift-diffusion simply does not provide an adequate understanding of the essential spin transport details. To achieve that, a Boltzmann equation

analysis of the interfacial spin transmissivity and a more detailed description of the electronic structure of the interface is likely to be required.

In summary, we have maintained a high spin torque efficiency $\xi_{SH} = 0.12 \pm 0.02$ in Pt|FeCoB based three terminal SHE-MTJ devices, while substantially reducing the effect of spin pumping in increasing the damping of the thin FeCoB free layer. We have achieved this by introducing a thin, nominally 0.5 nm, Hf layer between the Pt SHE layer and the FeCoB. This reduced the magnetic damping to $\alpha \approx 0.012$ without significantly changing the spin torque efficiency and thus subsequently lowered the SHE switching current density to $\approx 1.6 \times 10^{11}$ A/m^2. This value is approximately a factor of 2 lower than achieved previously in similar Ta|$Co_{40}Fe_{40}B_{20}$ SHE-MTJ devices having much higher resistivity. The decrease in the damping can be attributed to a suppression of spin pumping brought about by a large reduction of the effective spin mixing conductance $G_{\text{eff}}^{\uparrow\downarrow}$ of Pt|Hf|FeCoB compared to Pt|FM but in a way that does not reduce the absorption of spin current at the FM interface. Although further theoretical investigation is necessary for a complete explanation and optimally to guide further improvements, the experimental determination that Pt|Hf|FeCoB samples can provide high spin torque efficiency together with an electrical resistivity much less than for β-Ta and β-W, demonstrates clearly that Pt|Hf provides an attractive alternative to those materials for anti-damping SHE torque logic devices for which impedance and low excitation power are important criteria.

The authors thank J. Park, Y. Ou of Cornell University; C. T. Boone of NIST; and L. H. V. Leão of Federal University of Pernambuco (Brazil) for fruitful discussions. We thank S. Parkin of IBM Almaden Research Center for sharing a manuscript reporting a related study prior to publication. This work was supported in part by the NSF/MRSEC program (DMR-1120296) through the Cornell Center for Materials Research, ONR, and the Samsung Electronics

Corporation. We also acknowledge support from the NSF (Grant ECCS-0335765) through use of the Cornell Nanofabrication Facility/National Nanofabrication Infrastructure Network. A patent application has been filed on behalf of the authors regarding technology applications of some of the findings reported here.

SUPPLEMENTAL INFORMATION

4.S1. Sample Preparation

The multilayer films were produced by DC sputtering (radio frequency sputtering for the MgO layer) from 2-inch planar magnetron sources onto thermally-oxidized Si substrates in a sputter system with a base pressure $< 4\times10^{-8}$ Torr. The target to substrate separation was approximately 18 cm. This separation together with an oblique orientation of the target to the substrate resulted in a low deposition rate of ≈ 0.01 nm/s (Pt: 0.017 nm/s, Hf: 0.021 nm/s, FeCoB: 0.0077 nm/s) with DC sputtering conditions of 2 mTorr Ar and 30 watts power. The multilayer stacks ||Ta(1) | Pt(4) | Hf(t_{Hf}) | FeCoB(t_{FeCoB}) | MgO(1.6) | Ru(2) that were used for ST-FMR, anomalous Hall, and SQUID magnetometry measurements were patterned into 10×20 μm^2 microstrips by photolithography. The stacks ||Ta(1) | Pt(4) | Hf(t_{Hf}) | FeCoB(t_{FeCoB}) | MgO(1.6) | FeCoB(4) | Hf(5) | Ru(5) that were used for current-induced switching experiments were patterned into 3-terminal SHE-MTJ devices [7,8] which consisted of an elliptical FeCoB|MgO|FeCoB MTJ of typical size $\approx 50\times180$ nm^2 on top of a Hf|Pt|Ta channel of width $0.6-1.2$ μm (see Fig. 4.3(a) in the main text) by electron-beam lithography. The films were etched by an ion mill equipped with a mass spectroscopy system for endpoint detection. The samples were annealed at 300 C for 30 minutes in a vacuum tube furnace with a background pressure $<10^{-7}$ Torr.

4.S2. Measurements

The damping parameters were measured by the frequency-dependent spin torque ferromagnetic resonance [4] (ST-FMR) technique in which an external magnetic field was applied in-plane at a 45° angle with respect to the $10\times 20\,\mu m^2$ microstrip. A radio frequency signal of power 12 dBm and frequency 5-10 GHz was applied to the microstrip and the DC output signal was detected through a bias-tee by a lock-in amplifier. From the frequency f dependence of the linewidth Δ, the damping coefficient was calculated from the linear fit as $\alpha = (\gamma / 2\pi)\mathrm{d}\Delta / \mathrm{d}f$ (Fig. S1(a)) where $\gamma = 1.76\times 10^{11}$ Hz·T^{-1} is the gyromagnetic ratio.

The demagnetization fields were determined by anomalous Hall measurement with an applied magnetic field swept up to 1.5 T perpendicular to the sample plane as shown in Fig. 4.S1(b). The film magnetizations were measured by SQUID magnetometry with an in-plane magnetic field.

The current-switching measurement on the three-terminal devices was performed by applying an external magnetic field from a Helmholtz electric magnet parallel to the major axis of the nanopillar to null out the average dipole field on the thin free layer from the thicker, fixed layer. A swept direct current was applied through the Pt channel. The tunnel junction was connected in series with a 10 MΩ resistor and a lock-in amplifier was used to measure its total differential resistance.

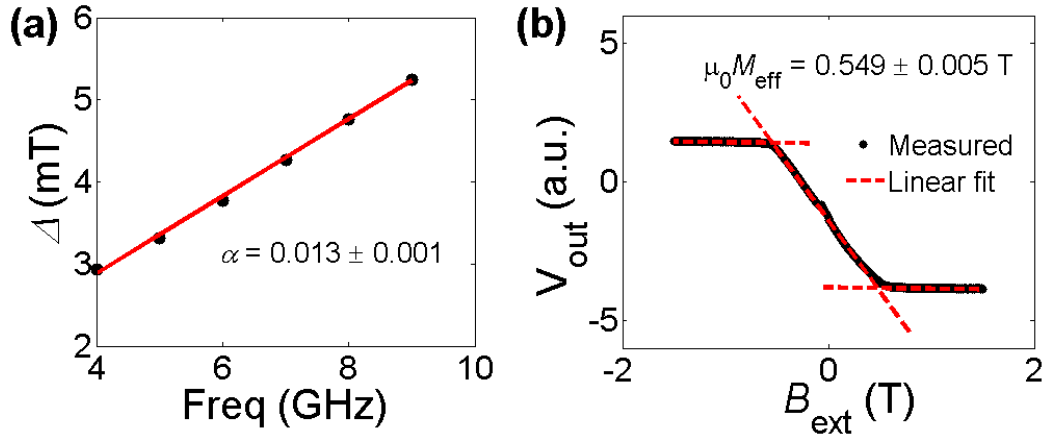

Figure 4.S1. (a) Determination of the Gilbert magnetic damping coefficient $\alpha = (\gamma / 2\pi)\mathrm{d}\Delta / \mathrm{d}f$ from the linear behavior of the line width Δ versus frequency f of a ||Ta(1) | Pt(4) | Hf(0.5) | FeCoB(1.6) | MgO(1.6) | Ru(2) sample by frequency-dependent ST-FMR measurement. **(b)** Determination of the effective demagnetization field of the same sample from the intersections of fitted lines to the variation of the anomalous Hall voltage as a function of the perpendicular applied magnetic field $\boldsymbol{B}_{\mathrm{ext}}$.

4.S3. Magnetic properties of Pt|Hf|FeCoB structure

The magnetic properties of the FeCoB layer in the first set of multilayers were characterized by SQUID magnetometry and anomalous Hall measurements (see 4.S2). In Fig. 4.S2(a) we show the thickness dependence of the FeCoB magnetic moment (per unit area). The linear fit indicates that the saturation magnetization $M_s = (1.56 \pm 0.06)$ ´ 10^6 A/m, and also that the FM has an apparent "magnetic dead layer" thickness $t_d = 0.7 \pm 0.1$ nm. In Fig. 4.S2(b) we plot the effective magnetic anisotropy energy $K_{\text{eff}} t_{\text{FeCoB}}^{\text{eff}}$ as a function of $t_{\text{FeCoB}}^{\text{eff}}$ for $t_{\text{Hf}} = 0.5$ nm, where $t_{\text{FeCoB}}^{\text{eff}} = t_{\text{FeCoB}} - t_d$ is the FeCoB effective thickness. Below $t_{\text{FeCoB}}^{\text{eff}} = 0.5$ nm, the magnetic anisotropy transitions from in-plane to out-of-plane. By fitting the data to the standard model for the thickness dependence of the magnetic anisotropy [38]

$$K_{\text{eff}} t_{\text{FeCoB}}^{\text{eff}} = \left(K_V - (1/2)\mu_0 M_s^2 \right) t_{\text{FeCoB}}^{\text{eff}} + K_S \qquad (4.S1)$$

the interface and bulk anisotropy energy densities are estimated to be $K_S = 0.45 \pm 0.03$ mJ/m^2 and $K_V = 0.60 \pm 0.03$ MJ/m^3, respectively. This value of K_S is smaller than typical for Ta|FeCoB|MgO multilayers, while K_V is similar to a recent report [39].

The in-plane effective demagnetization field $\mu_0 M_{\text{eff}}$ for $t_{\text{FeCoB}} = 1.6$ nm and $t_{\text{FeCoB}} = 1.8$ nm ||Ta(1)|Pt(4)|Hf(t_{Hf})|FeCoB(t_{FeCoB})|MgO(1.6)|Ru(2) samples are shown in Fig. 4.S2(c). From these data it is clear that the insertion of a thin layer Hf at the interface of Pt and FeCoB has a significant effect on $\mu_0 M_{\text{eff}}$, with a local *minimum* at $t_{\text{Hf}} = 0.5$ nm for both series. We tentatively attribute this behavior to the role of the Hf insertion layer in both reducing the positive volume anisotropy effect from elastic strain from the underlying Pt, and in enhancing the surface anisotropy energy through reduction of strain at the FeCoB|MgO interface.

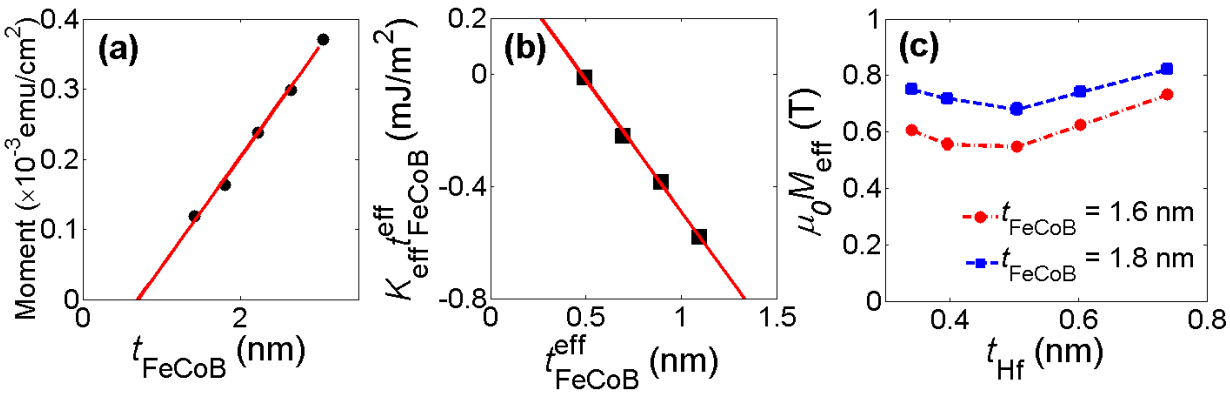

Figure 4.S2. (a) Magnetic moment per unit area versus FeCoB thickness of $t_{\mathrm{Hf}} = 0.5\,\mathrm{nm}$ samples. From the linear fits (line), the saturation magnetization and thickness of the "dead layer" of FeCoB are $1.56 \pm 0.06 \times 10^6$ A/m and $0.7 \pm 0.1\,\mathrm{nm}$. **(b)** Magnetic anisotropy energy as a function of FeCoB effective thickness $t_{\mathrm{FeCoB}}^{\mathrm{eff}}$. From the linear fit (line), the interface and bulk anisotropy energy densities are $0.45 \pm 0.03\,\mathrm{mJ/m^2}$ and $0.60 \pm 0.03\,\mathrm{MJ/m^3}$, respectively. **(c)** Effective demagnetization field $\mu_0 M_{\mathrm{eff}}$ versus Hf thickness t_{Hf} of $t_{\mathrm{FeCoB}} = 1.6\,\mathrm{nm}$ (circles) and $t_{\mathrm{FeCoB}} = 1.8\,\mathrm{nm}$ samples (squares). Broken lines connect the data points.

4.S4. Properties of the Pt|FeCoB control sample

From the vibrating sample magnetometry measurement on ||Ta(1) | Pt(4) | FeCoB(t_{FeCoB}) | MgO(1.6) | Ru(2) annealed samples, the saturation magnetization was determined to be $M_s = (1.0 \pm 0.1) \times 10^6$ A/m with no apparent magnetic dead layer. The same structure was patterned into microstrips used for frequency-dependent ST-FMR measurement from which the Gilbert magnetic damping parameter was determined, as shown in Fig. 4.S3. As reported in the main text the best fit to the spin pumping prediction yielded $G_{\mathrm{eff}}^{\uparrow\downarrow} = (1.1 \pm 0.1) \times 10^{15}\ \Omega^{-1}\mathrm{m}^{-2}$ with the damping parameter for isolated FeCoB be 0.005 ± 0.001 which is consistent with that obtained in Fig. 4.2(b) (main text).

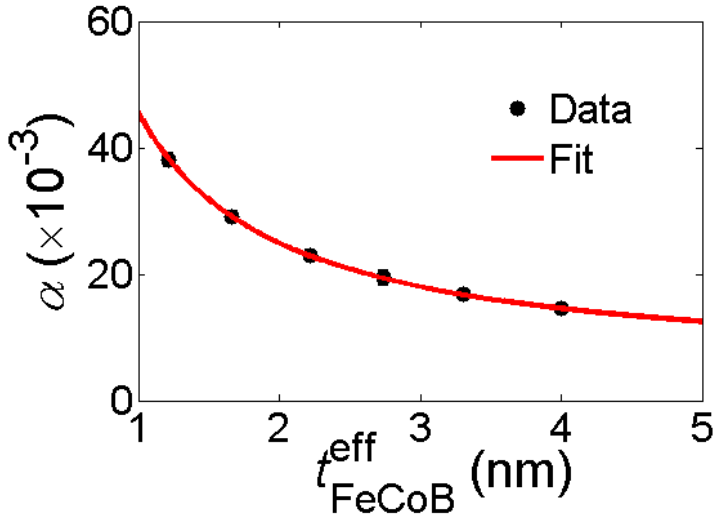

Figure 4.S3. Magnetic damping parameter versus FeCoB thickness of the control samples.

4.S5. Resistivity measurements

The resistance of a film of a comparatively good metal, such as Pt, when placed between two much higher resistivity layers, such as either Ta and FeCoB, or Ta and Hf|FeCoB, begins, once the middle film's thickness is reduced to the order of twice its "bulk" elastic mean free path l, to be determined by diffusive scattering at the interfaces and within the adjoining layers. This effect can be modeled with the Fuchs-Sondheimer formulation [42]. Since l_{Pt} in our films is ~ 2 nm, while that of the other adjoining metals are considerably shorter, interfacial scattering plays an important role in determining the electrical properties of the spin Hall structure, and also must be taken into proper consideration when considering the flow of the spin current from the bulk of the Pt layer to the Pt|Hf|FeCoB interface. From the viewpoint of the electrical energy required to effect a requisite spin transfer torque on the ferromagnetic free layer, what matters of course is the resistance per square $R_{\square,SH}$ of the spin Hall nanostrip, which we find to be $R_{\square,SH} \approx 120\Omega/\square$ for an annealed ||Ta(1) | Pt(4) | Hf(0.5) | FeCoB(2) multilayer. This result can be alternatively expressed in terms of an averaged Pt resistivity $\overline{\rho}_{Pt} = R_{\square,SH} t_{Pt} = 50\ \mu\Omega\cdot\text{cm}$ for $t_{Pt} = 4$ nm. If a thinner Pt layer is used, $\overline{r}_{Pt}$ will be higher due to the interfacial scattering, shorter effective mean free path. Finally we note that there was approximately a 10% increase in $\overline{r}_{Pt}$ upon annealing our structures, which we take as indicative of enhanced diffusive scattering at the interface due to some additional intermixing, or perhaps the formation of a thicker PtHf bimetallic layer at the interface.

Of course when considering the flow of a net spin population generated by the SHE within the Pt to the interface $\overline{r}_{Pt}$ is not the proper quantity to employ in determining that spin conductance if $\overline{r}_{Pt}$ is determined largely by scattering close to or at the interface. Instead we measured the "differential resistivity" of the Pt as evaluated from the derivative of the conductance versus Pt thickness for $t_{Pt} > 3\text{nm}$ in Ta(1) | Pt(x) | Hf(0.5) | CoFeB multilayers which yielded a "bulk"

resistivity $\rho_{Pt} \approx 20\,\mu\Omega\cdot\mathrm{cm}$. Similar measurements where the Hf thickness was varied yielded a bulk Hf resistivity $r_{Hf} \approx 80\,\mu\Omega\cdot\mathrm{cm}$ for $t_{Hf} \approx 2\,\mathrm{nm}$. These were the values used in our drift-diffusion analysis of the spin pumping and spin Hall torque experimental results. Of course the fact that in these experiments the thickness of the Pt spin Hall metal is only comparable to the bulk mean free path l_{Pt}, together with the fact that the spin attenuation length, $\lambda_s^{Pt} \approx 1.2-1.4$ nm, as determined by previous work [27,28], is less than l_{Pt} brings into question any prediction that is based on a drift-diffusion analysis.

4.S6. Drift-Diffusion Analysis

4.S6(a) Spin pumping effect

If we put aside the question raised above as to the applicability of a drift-diffusion treatment of a system where the thickness of a normal metal layer component is of of the order of its mean free path, or less in the case of the one or two atomic layer thick Hf insertion layer, and where the spin attenuation length of one of the metals is apparently less than its mean free path, we can employ the trilayer spin pumping model of Boone *et al* [25] to consider how an insertion layer can result in a reduction of G_{ext}. This drift-diffusion based model predicts

$$G_{\text{ext}} = \frac{G_{\text{Hf}}}{2}\left[\frac{G_{\text{Hf}}\coth\left(t_{\text{Pt}}/\lambda_s^{\text{Pt}}\right)+G_{\text{Pt}}\coth\left(t_{\text{Hf}}/\lambda_s^{\text{Hf}}\right)}{G_{\text{Hf}}\coth\left(t_{\text{Pt}}/\lambda_s^{\text{Pt}}\right)\coth\left(t_{\text{Hf}}/\lambda_s^{\text{Hf}}\right)+G_{\text{Pt}}}\right], \tag{4.S2}$$

where $G_{\text{Hf}} \equiv 1/(\rho_{\text{Hf}}\lambda_s^{\text{Hf}})$ and $G_{\text{Pt}} \equiv 1/(\rho_{\text{Pt}}\lambda_s^{\text{Pt}})$. For Pt and Hf thin films with $\rho_{\text{Pt}} = 20\ \mu\Omega\cdot\text{cm}$ and $\rho_{\text{Hf}} = 80\ \mu\Omega\cdot\text{cm}$, the spin attenuation lengths have been reported to be $\lambda_s^{\text{Pt}} = 1.4\ \text{nm}$ [27,28] and $\lambda_s^{\text{Hf}} = 1.5\ \text{nm}$ [34] respectively. A calculation using these parameters in equation (S1) indicates that that G_{ext} can be only slightly reduced by a Hf insertion layer with $t_{\text{Hf}} < 1$ nm. Thus the low effective spin-mixing conductance $G_{\text{eff}}^{\uparrow\downarrow} \approx 0.24\times10^{15}\ \Omega^{-1}\text{m}^{-2}$ measured at $t_{\text{Hf}} \approx 0.5\,\text{nm}$ cannot be achieved without substantially reducing the bare spin-mixing conductance $G^{\uparrow\downarrow}$. However, a low $G^{\uparrow\downarrow}$ will enhance the back flow of the spin current from the Hf|FeCoB interface, lowering ξ_{SH}. Alternatively if we use a much different pair of parameters for the Hf layer, a higher resistivity ρ_{Hf} and a shorter spin attenuation length λ_s^{Hf} in equation (4.S2) this would result in a lower G_{ext}. However since the experimental evidence is that Hf has no significant SHE and thus that the spin current has to originate within the Pt, a shorter λ_s^{Hf} would also result in a strong attenuation of the

spin current before it reaches the Hf|FeCoB interface as discussed below.

4.S6(b) Attenuation of the spin current in a trilayer structure

Within the context of the drift-diffusion analysis [23] of the spin back-flow in a trilayer structure, Equation (4.3) in the main text is modified to be:

$$\xi_{SH}(t_{Hf}) = \theta_{SH}^{Pt} \times \frac{2\left[\cosh\left(t_{Pt}/\lambda_s^{Pt}\right)-1\right]}{\frac{\cosh\left(t_{Pt}/\lambda_s^{Pt}\right)\sinh\left(t_{Hf}/\lambda_s^{Hf}\right)}{\rho_{Hf}\lambda_s^{Hf}} + \frac{\cosh\left(t_{Hf}/\lambda_s^{Hf}\right)\sinh\left(t_{Pt}/\lambda_s^{Pt}\right)}{\rho_{Pt}\lambda_s^{Pt}}} \times G_{eff}^{\uparrow\downarrow}(t_{Hf}) \quad . (4.S3)$$

The rapid decrease of damping a that we find with our samples as a function of increasing t_{Hf}, as shown in Fig. 4.2(a) of the main text, implies the same degree of reduction in $G_{eff}^{\uparrow\downarrow}$, from Equation (4.S3) we should expect an even more rapid reduction in ξ_{SH}. This expectation is not in accord with the approximately constant level of the observed ξ_{SH} for $t_{Hf} \le 0.5\,\text{nm}$ as shown in Fig. 4.4 of the main text. We conclude that the drift-diffusion analysis of the spin back-flow is simply not even approximately applicable to this spin Hall effect system with a very thin Hf insertion layer, perhaps due to dominance of interfacial processes, rather than bulk scattering, on the spin transport. As mentioned in the main text it appears that a more appropriate Boltzmann analysis of the interfacial spin transmissivity and a more detailed treatment of the electronic structure of the interfaces is likely to be required to understand this beneficial effect of the thin Hf insertion layer in enhancing the anti-damping spin torque efficiency of the Pt spin Hall effect.

REFERENCES

[1] M. I. Dyakonov and V. I. Perel, Phys. Leters **35A**, 459 (1971).

[2] J. Hirsch, Phys. Rev. Lett. **83**, 1834 (1999).

[3] A. Hoffmann, IEEE Trans. Magn. **49**, 5172 (2013).

[4] L. Liu, T. Moriyama, D. C. Ralph, and R. A. Buhrman, Phys. Rev. Lett. **106**, 036601 (2011).

[5] A. Ganguly, K. Kondou, H. Sukegawa, S. Mitani, S. Kasai, Y. Niimi, Y. Otani, and A. Barman, Appl. Phys. Lett. **104**, 072405 (2014).

[6] L. Liu, C.-T. Chen, and J. Z. Sun, Nat. Phys. **10**, 561 (2014).

[7] L. Liu, C.-F. Pai, Y. Li, H. W. Tseng, D. C. Ralph, and R. A. Buhrman, Science **336**, 555 (2012).

[8] C.-F. Pai, L. Liu, Y. Li, H. W. Tseng, D. C. Ralph, and R. A. Buhrman, Appl. Phys. Lett. **101**, 122404 (2012).

[9] L. Liu, C.-F. Pai, D. C. Ralph, and R. A. Buhrman, Phys. Rev. Lett. **109**, 186602 (2012).

[10] V. E. Demidov, S. Urazhdin, H. Ulrichs, V. Tiberkevich, A. Slavin, D. Baither, G. Schmitz, and S. O. Demokritov, Nat. Mater. **11**, 1028 (2012).

[11] V. E. Demidov, H. Ulrichs, S. V Gurevich, S. O. Demokritov, V. S. Tiberkevich, A. N. Slavin, A. Zholud, and S. Urazhdin, Nat. Commun. **5**, 3179 (2014).

[12] T. Jungwirth, J. Wunderlich, and K. Olejník, Nat. Mater. **11**, 382 (2012).

[13] P. P. J. Haazen, E. Murè, J. H. Franken, R. Lavrijsen, H. J. M. Swagten, and B. Koopmans, Nat. Mater. **12**, 299 (2013).

[14] N. Okamoto, H. Kurebayashi, T. Trypiniotis, I. Farrer, D. A. Ritchie, E. Saitoh, J. Sinova, J. Mašek, T. Jungwirth, and C. H. W. Barnes, Nat. Mater. **13**, 932 (2014).

[15] D. Bhowmik, L. You, and S. Salahuddin, Nat. Nanotech. **9**, 59 (2013).

[16] D. M. Bromberg, D. H. Morris, L. Pileggi, and J.-G. Zhu, IEEE Trans. Magn. **48**, 3215 (2012).

[17] S. Urazhdin, V. E. Demidov, H. Ulrichs, T. Kendziorczyk, T. Kuhn, J. Leuthold, G. Wilde, and S. O. Demokritov, Nat. Nanotech. **9**, 509 (2014).

[18] X. Fan, H. Celik, J. Wu, C. Ni, K.-J. Lee, V. O. Lorenz, and J. Q. Xiao, Nat. Commun. **5**, 3042 (2014).

[19] R. Lo Conte, E. Martinez, A. Hrabec, A. Lamperti, T. Schulz, L. Nasi, L. Lazzarini, R. Mantovan, F. Maccherozzi, S. S. Dhesi, B. Ocker, C. H. Marrows, T. A. Moore, and M. Kläui, Phys. Rev. B **91**, 014433 (2015).

[20] G. Chen, T. Ma, A. T. N'Diaye, H. Kwon, C. Won, Y. Wu, and A. K. Schmid, Nat. Commun. **4**, 2671 (2013).

[21] Y. Tserkovnyak, A. Brataas, and G. Bauer, Phys. Rev. Lett. **88**, 117601 (2002).

[22] M. Polianski and P. Brouwer, Phys. Rev. Lett. **92**, 026602 (2004).

[23] P. M. Haney, H.-W. Lee, K.-J. Lee, A. Manchon, and M. D. Stiles, Phys. Rev. B **87**, 174411 (2013).

[24] Y.-T. Chen, S. Takahashi, H. Nakayama, M. Althammer, S. Goennenwein, E. Saitoh, and G. Bauer, Phys. Rev. B **87**, 144411 (2013).

[25] C. T. Boone, H. T. Nembach, J. M. Shaw, and T. J. Silva, J. Appl. Phys. **113**, 153906 (2013).

[26] P. Deorani and H. Yang, Appl. Phys. Lett. **103**, 232408 (2013).

[27] L. Liu, R. A. Buhrman, and D. C. Ralph, arXiv:**1111.**3702 (2011).

[28] W. Zhang, V. Vlaminck, J. E. Pearson, R. Divan, S. D. Bader, and A. Hoffmann, Appl.

Phys. Lett. **103**, 242414 (2013).

[29] Y. Li, Interfacial Effects in FeCoB Based Magnetic Tunnel Junctions and Spin Hall Effect Bi-Layer Structures. PhD Dissertation, Cornell University, 2014.

[30] S. Emori, U. Bauer, S.-M. Ahn, E. Martinez, and G. S. D. Beach, Nat. Mater. **12**, 611 (2013).

[31] E. Martinez, S. Emori, and G. S. D. Beach, Appl. Phys. Lett. **103**, 072406 (2013).

[32] W. Zhang, W. Han, X. Jiang, S.-H. Yang, and S. S. P. Parkin, Nat. Phys. **11**, 496 (2015).

[33] C.-F. Pai, Y. Ou, L. H. Vilela-Leão, D. C. Ralph, and R. A. Buhrman, Phys. Rev. B **92**, 064426 (2015).

[34] C.-F. Pai, M.-H. Nguyen, C. Belvin, L. H. Vilela-leão, D. C. Ralph, and R. A. Buhrman, Appl. Phys. Lett. **104**, 082407 (2014).

[35] D. A. Muller, L. F. Kourkoutis, M. Murfitt, J. H. Song, H. Y. Hwang, J. Silcox, N. Dellby, and O. L. Krivanek, Science **319**, 1073 (2008).

[36] O. Levy, G. L. W. Hart, and S. Curtarolo, Acta Mater. **58**, 2887 (2010).

[37] W. Xing, X. Q. Chen, D. Li, Y. Li, C. L. Fu, S. V. Meschel, and X. Ding, Intermetallics **28**, 16 (2012).

[38] M. T. Johnson, P. J. H. Bloemen, F. J. A. Den Broeder, and J. J. de Vries, Reports Prog. Phys. **59**, 1409 (1996).

[39] M. Hayashi, M. Yamanouchi, S. Fukami, J. Sinha, S. Mitani, and H. Ohno, Appl. Phys. Lett. **100**, 192411 (2012).

[40] E. B. Myers, F. J. Albert, J. C. Sankey, E. Bonet, R. A. Buhrman, and D. C. Ralph, Phys. Rev. Lett. **89**, 196801 (2002).

[41] J. Z. Sun, Phys. Rev. B **62**, 570 (2000).

[42] F. Warkusz, Electrocompon. Sci. Technol. **5**, 99 (1978).

CHAPTER 5

Nanosecond Reversal of Three-Terminal Spin Hall Effect Memory Devices at Cryogenic Temperatures

Minh-Hai Nguyen[1,2,*], Graham E. Rowlands[2,*], Sriharsha V. Aradhya[1], Colm A. Ryan[2], D. C. Ralph[1,3], R. A. Buhrman[1], Thomas A. Ohki[2]

[1] *Cornell University, Ithaca, New York 14853, USA*

[2] *Raytheon BBN Technologies, Cambridge, MA 02138, USA*

[3] *Kavli Institute at Cornell, Ithaca, New York 14853, USA*

[*] *These authors contribute equally to this work*

ABSTRACT

Cryogenic computers promise to reduce the overall power consumption by greatly lowering the dissipated energy of conducting lines and devices. The three-terminal magnetic tunnel junction (3T-MTJ) devices, powered by the strong spin Hall effect of the channel, is a possible candidate for cryogenic memory due to its nonvolitality and low switching power. We report nanosecond fast and reliable switching of 3T-MTJ devices having a Pt channel at a low temperature of 3.1 K. The switching pulses can be as short as 1 ns and the bit error rates as low as 10^{-7}. The results are consistent with those reported at room temperature and suggest the possibility to integrate these memory devices with superconducting logic devices.

MAIN TEXT

Spin-torque magnetoresistive memory (ST-MRAM) devices are rapidly entering the market as the next generation of memory compatible with and beyond CMOS technology [1], owing to their nonvolatility and low power consumption. These ST-MRAM devices generally have 2-terminal magnetic tunnel junctions (MTJs) which consist of two ferromagnetic (FM) layers, separated by a thin insulating tunnel barrier, one of which (reference layer) has a fixed magnetization and the magnetization of the other one (free layer) can be flipped parallel (P) or anti-parallel (AP) to that of the reference layer. In the CPP (current perpendicular to plane) configuration, a current is applied though the tunnel barrier of the MTJ to switch the magnetization of the free layer via spin transfer torque (STT). Despite many advantages over conventional memory devices, there are several shortcomings associated with this structure, such as the breakdown of the tunnel barrier during the writing process, read disturb errors and incubation delay. In recent years, another class of MRAM devices called spin-orbit torque (SOT) MRAM has been proposed. This structure, schematically illustrated in Fig. 5.1(a), has the CIP (current in the layer's plane) configuration in which a current is applied in the channel adjacent to the MTJ to switch the free layer via the spin-orbit interaction, induced either by the interfacial Rashba-Edelstein effect or the bulk spin Hall effect (SHE) [2,3] which converts a longitudinal electrical current in the channel into a transverse spin current. By separating the read and write paths, this 3-terminal geometry avoids the breakdown of the tunnel barrier and the read disturb error, and allows large room for optimization. It has been reported that the SHE in Pt [3,4], Ta [2] and W [5] is strong enough to effectively manipulate the MTJ. Thus this 3-terminal SHE-based MTJ (3T- MTJ) structure is a promising candidate for low power and fast memory in which density is not a critical factor. Previously we have demonstrated power efficient nanosecond pulse switching of the 3T- MTJ devices having a

Pt channel which can switch as fast as 1 - 2 ns and with a low bit error rate (BER) of 10^{-5} at room temperature (RT) [6].

Another important strategy to reduce the power consumption is the avoidance of heat dissipation of conducting lines and devices. It has been suggested that cryogenic computers, which consist in large part of superconducting lines and devices, can vastly reduce the power consumption despite the energy cost to cool the entire system down to cryogenic temperatures. Superconducting logic devices have been actively researched, most notably Josephson junctions and recently nanocryotron devices (nTron) [7]. However, the cryogenic computer scheme is still in need of compatible memory devices. Cryogenic temperatures impose a big challenge to many types of RT memory devices since their working mechanism may largely change at low temperatures. MRAM devices, however, are based on the spin-transfer torque and/or spin-orbit interaction which do not depend strongly on temperatures. Thus, it is of scientific and technological importance to investigate the behavior of MRAM devices at cryogenic temperatures.

In this article, we report pulse switching behavior of the 3T- MTJ devices having a Pt channel at a low temperature of 3.1 K, which is very consistent to that at RT. Similar results are obtained when we replace square pulses by triangle ones, suggesting easy integration of the 3T-MTJ structure with cryogenic devices such as the nTron.

The stack consisted of SiO_x | Ta(1) | Pt(5) | Hf(0.7) | FeCoB(1.4) | MgO | FeCoB (1.2) | Ta(0.2) | FeCoB(1.2) | FeCo(1) | Ru(0.85) | FeCo(2.5) | IrMn(7) | Ru(4) (thicknesses in nm, FeCoB = $Fe_{60}Co_{20}B_{20}$), DC and RF magnetron sputter-deposited onto thermally oxidized high-resistivity Si wafers by Canon ANELVA, Inc. Because of the thin and highly resistive 1 nm Ta layer at the bottom, used to smoothen the wafer surface, most of the electrical current in the channel flows in the 5 nm Pt layer. The thin 0.7 nm Hf spacer between the channel and the 1.4 nm FeCoB free layer

was used to reduce the Gilbert magnetic damping by lowering the enhanced damping due to spin pumping and/or spin memory loss at the Pt/FM interface [4]. The multilayer stack was patterned into 230 nm × 400 nm channels by deep-UV photolithography and 45 nm × 115 nm pillars by electron-beam lithography, etched by Ar ion milling. The devices were annealed at 300 C for 45 minutes in a vacuum of $< 10^{-6}$ Torr in the applied field on 0.15 T along the easy axis. Previously this 3T-MTJ structure demonstrated low-power, fast and reliable switching at room temperature, as reported in [6].

The sample was placed in a cryogen-free HPD cryo-probe station's chamber having a low temperature of 3.1 K, connected to the measuring equipments via microwave probes. We measured the resistance of the MTJ by flowing a small current of 3 μA through the tunnel barrier and measuring the drop voltage. An external field was applied along the easy axis of the MTJ by a superconducting magnet inside the chamber. See Supplemental Information (section 5.S1) for more details. Fig. 5.1(b) shows the magnetic hysteresis (minor) loop of the device which exhibits a TMR of about 30%, and a coercivity of 4.8 mT, about 2 times higher than that at RT.

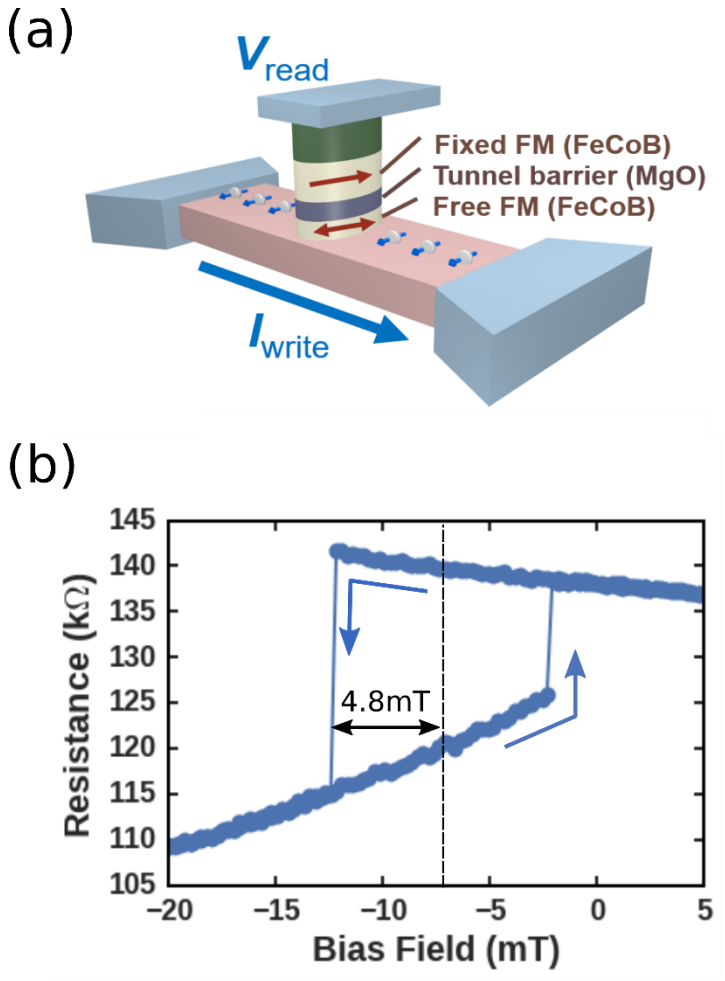

Figure 5.1: (a) Schematic of a 3T-SHE-MTJ device which consists of an MTJ atop a spin Hall channel. An electrical current is applied to the channel to switch the magnetization of the free layer and the state of the MTJ is read by measuring the drop voltage with a small current (3 μA) through the junction. (b) The field-switching behavior of the device. The TMR is about 30%. Coercivity is 4.8 mT with an offset field of -7.4 mT.

For pulse switching measurements, a series of alternate reset and switching pulses were sent to the channel of the device and the MTJ resistance was read after each pulse. Each switching probability is the expectation value over 1024 switching attempts. Fig. 5.2 shows the pulse switching phase diagram for AP to P (a) and P to AP (b) transition at an applied field of -7.4 mT (center field of the minor loop). The pulse height is the voltage drop across the channel after considering the reflection at the contact between the probe and the channel, due to the high resistance of the channel of about 1.0 kΩ. Note that in our previous work [6], such reflection at the contact pads was not taken into account. The data points on the phase diagrams are grouped into adjacent triangles by Delaunay triangulation. The color of each triangle represents the average value of its vertices (see Supplemental Information 5.S2). The results shown in Fig. 5.2 are qualitatively consistent with the expectation from the macrospin model [8,9] in which the boundary of 50% switching probability follows the relation:

$$V = V_0(1 + t_0 / t) \tag{5.1}$$

where V, t are the pulse height and duration, respectively and V_0, t_0 are constant. From the fitting of the 50% probability boundary (white areas) to the macrospin model, the characteristic parameters V_0, t_0 are estimated to be 0.81 V, 0.71 ns for AP to P and 1.0 V, 0.80 ns for P to AP. The values of t_0 are similar to those reported for devices having 335 nm channel and 1.6 nm FeCoB free layer at RT [6] but those of V_0 are about 30% lower which is attributed to narrower channel (230 nm) having the same resistance of 1.0 kΩ. Notice the deviation of the fitted line from the data points for P to AP which indicates the involvement of the Oersted field on the microspin dynamics which depends strongly on the distribution and evolution of magnetic subdomains in the free layer as discussed in Ref. [10].

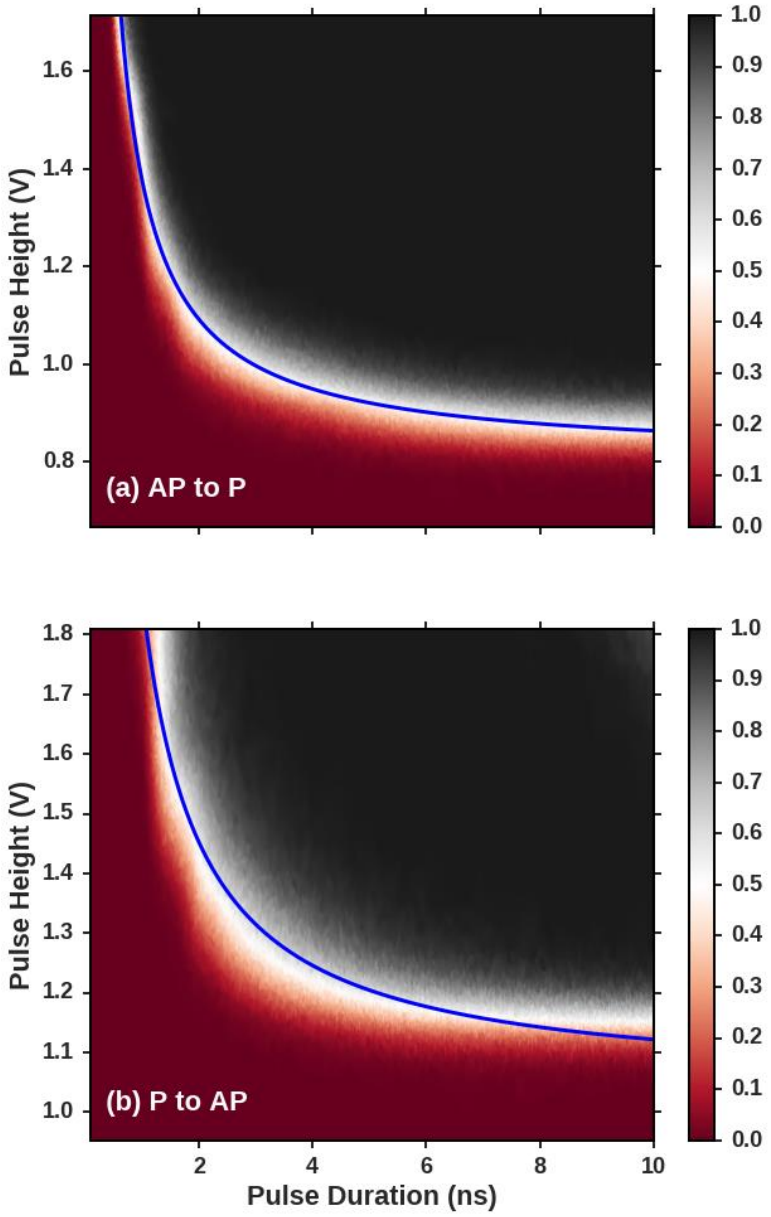

Figure 5.2: Pulse switching phase diagram for (a) AP to P and (b) P to AP at applied field -7.4 mT. The blue solid lines show fitted results to the macrospin model from which the characteristic parameters are estimated to be V_0 = 0.81 V, t_0 = 0.71 ns for AP to P and V_0 = 1.0 V, t_0 = 0.80 ns for P to AP.

The same measurement and analysis were performed for different bias fields. Fig. 5.3 shows the estimated V_0 and t_0 as functions of the bias field. The linear dependence of V_0 versus bias field can be understood by the modification of the effective energy barrier by the bias field in the spin-torque picture [11]. t_0 shows a variation with bias field of about 30% around 0.8 ns but no apparent trend. This fast switching speed, about the same as that at RT, is surprising because the thermal fluctuation at 3.1 K is much smaller than at RT, thus the device is expected to switch on average at lower speed due to the incubation delay. Together with the deviation from the macrospin model as shown in Fig. 5.2(a), it suggests the complicated switching mechanism for which we tentatively attribute to the complex domain formation of the free layer. As discussed in detail in Ref. [10], the switching speed, characterized by the critical time t_0, is strongly affected by the Oersted field generated by the current and the applied bias field, in combination with any field-like effect induced by the SHE in the bulk [12] and/or at the interface [13] of the channel, and in some cases can be below the macrospin limit of about 2 ns (due to incubation delay). Therefore, the fast switching speed that we observed at 3.1 K indicates the strong effect of the total bias field in the switching mechanism which is beyond the macrospin model.

To demonstrate the switching reliability of the sample, we performed the switching/bit error rate (BER = 1 – switching probability) measurements. Fig. 5.4 shows the BER as a function of pulse height for 3 ns and 5 ns pulse durations. For AP to P switching (negative pulse voltages), the BER can be as low as order of 10^{-7} given high enough pulse voltage and duration.

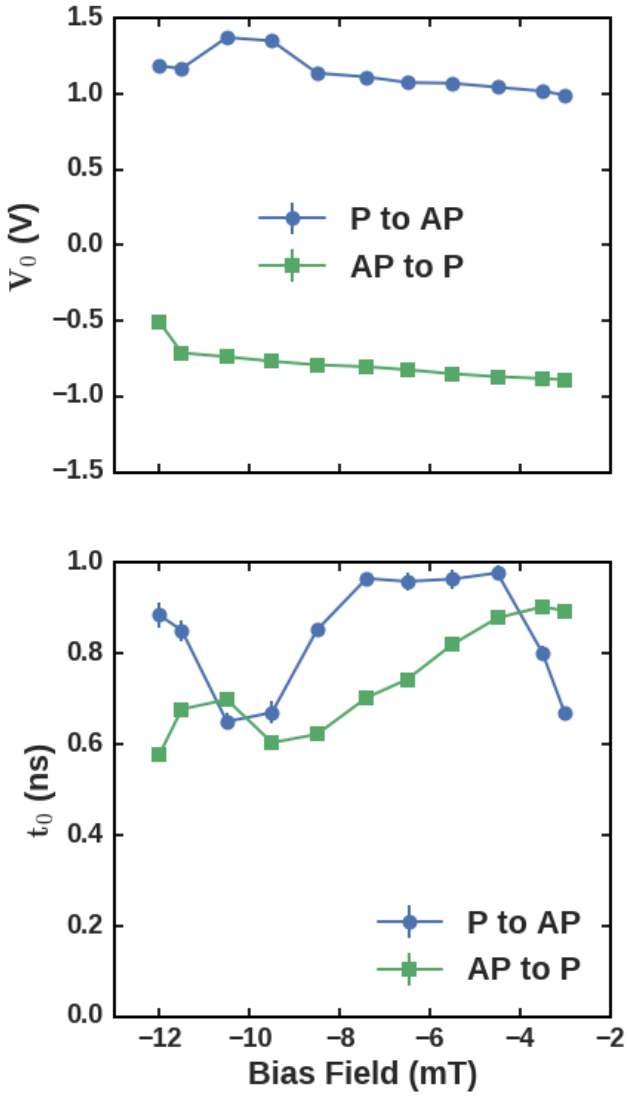

Figure 5.3: The estimated values of V_0 and t_0, estimated from fitting to the macrospin model, as functions of bias field for P to AP (blue circles) and AP to P (green squares).

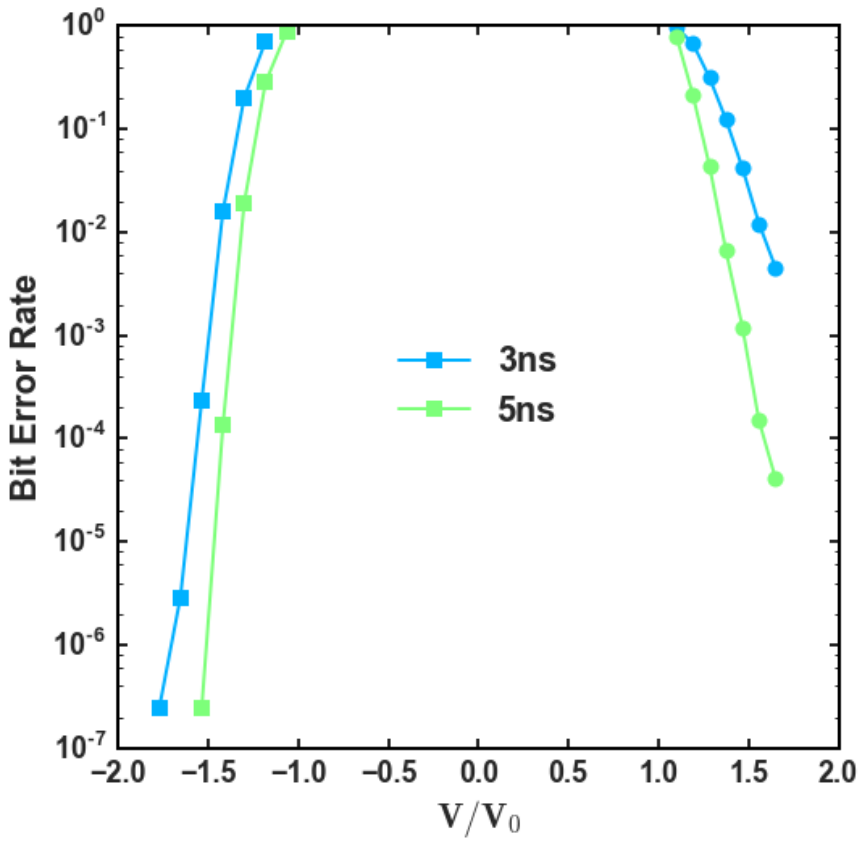

Figure 5.4: Bit error rate as a function of pulse voltage (relative to V_0) for pulse duration of 3 ns and 5 ns for AP to P (negative voltages) and P to AP (positive voltages) under the bias field = -7.4 mT.

Thus far, we have demonstrated the low-power, fast and reliable pulse switching of the 3T-SHE-MTJ devices at a low temperature of 3.1 K using square pulses. These factors are important for applications in superconducting computing prototypes in which a large amount of Joule heating can be avoided by flowing dissipationless currents through superconducting connections and devices. One of the promising candidates for superconducting gates is the nanocryotron (nTron) devices developed by McCaughan *et al*. [7]. Here we demonstrate that our 3T- MTJ devices can be readily integrated with nTron devices.

A simple way to control the writing current through the channel of the 3T-MTJ device is to have an nTron in parallel with the channel, as illustrated in Fig. 5.5(a). In normal condition (no pulses applied), the nTron device is in the superconducting state, but the 3T-MTJ device is not, therefore all the current flows through the nTron device. To switch the 3T-MTJ device, a pulse is sent to the third gate of the nTron device causing heating at the junction to break its superconducting state. Then a large amount of current flows through the channel of the 3T-MTJ device, however not as a square form but a triangle-like shape having a quick rise and slow decay. In our experiment setup, we simulate nTron-like pulses using the Keysight arbitrary waveform generator (AWG), as shown in Fig. 5.5(b). The nTron-like pulse rises very quickly to a peak value (pulse height) with a time constant of 80 ps, keeps constant for 170 ps then gradually fall down to zero as e^{-t/t_0} where t_o can be defined as its pulse duration.

The response of the 3T-MTJ device to the nTron-like pulses is shown in Fig. 5.5(c) in which the boundaries between non-switched and highly successfully switched regions are clearly formed, similarly to the results shown in Fig. 5.2. In response to the nTron-like pulses, the device switches at nearly the same range of pulse height but requires longer pulse duration, mainly due to the slow decay of the nTron-like pulses.The switching reliability of the 3T-MTJ device with nTron-like

pulses is shown in Fig. 5.5(d) for AP to P transition from which a low BER, order of 10^{-6}, is observed given high and long enough pulses. (The sample failed to the high electrical stress after this measurement so we don't have the BER data for P to AP transition. A complete set of data for a different sample will be reported elsewhere.)

In conclusion, we demonstrate that the 3T- MTJ devices with Pt channel exhibit low-current, fast and reliable square-pulse switching behavior at 3.1 K, consistent with that at RT. Moreover, the devices show similar response to nTron-like pulses, thus can be readily integrated with nTron devices in superconducting computing prototypes. These results suggest the 3T-MTJ structure can be a promising candidate for low power and fast memory at room as well as cryogenic temperatures.

The research is based upon work supported by the Office of the Director of National Intelligence (ODNI), Intelligence Advanced Research Projects Activity (IARPA), via contract W911NF-14-C0089. The views and conclusions contained herein are those of the authors and should not be interpreted as necessarily representing the official policies or endorsements, either expressed or implied, of the ODNI, IARPA, or the U.S. Government. The U.S. Government is authorized to reproduce and distribute reprints for Governmental purposes notwithstanding any copyright annotation thereon. Additionally, this work was supported by the NSF/MRSEC program (DMR-1120296) through the Cornell Center for Materials Research. This work was performed in part at the Cornell NanoScale Facility, a member of the National Nanotechnology Coordinated Infrastructure (NNCI), which is supported by the National Science Foundation (Grant ECCS-1542081).

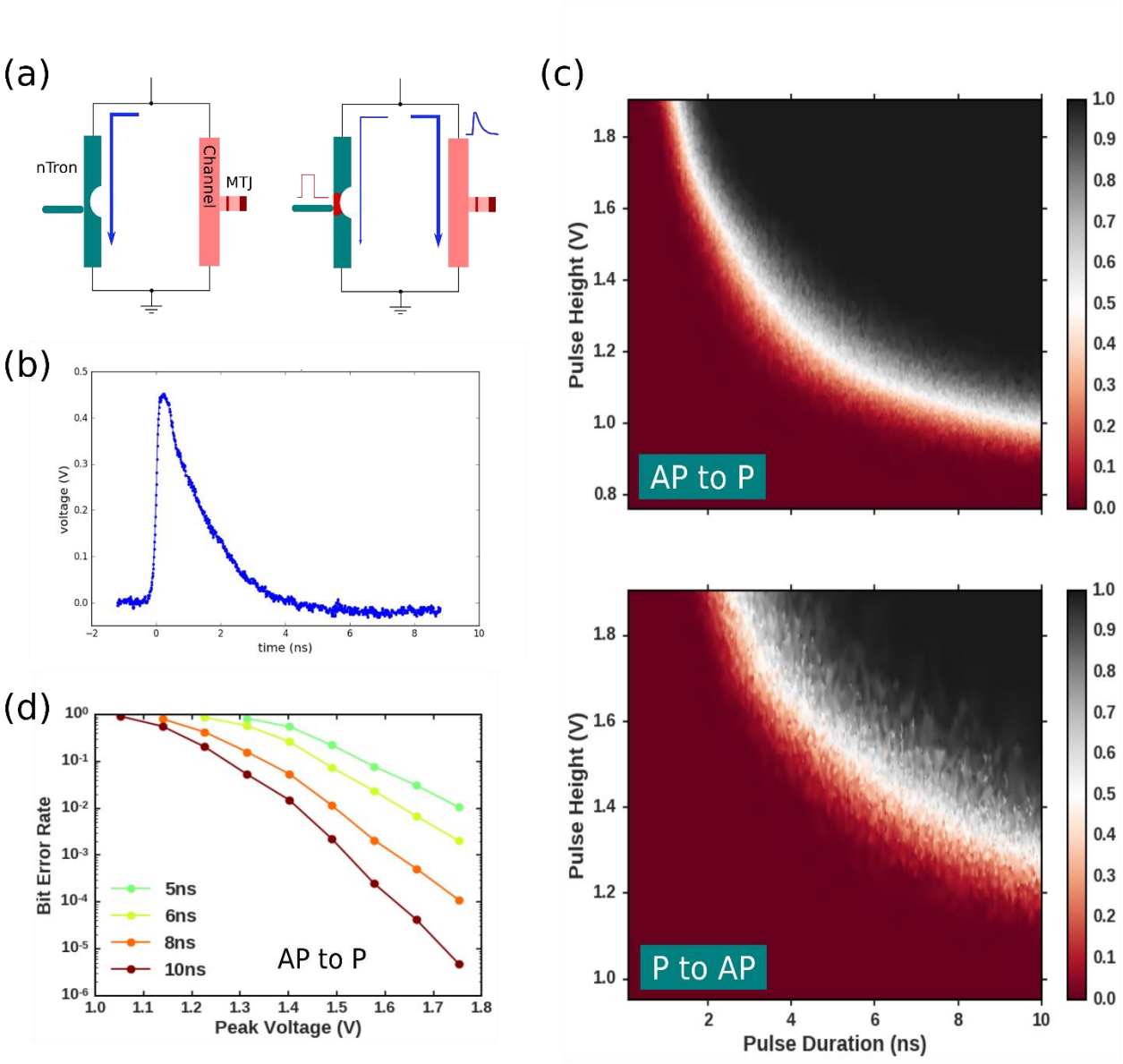

Figure 5.5: (a) Diagram of a simple writing circuit of the SHE-MTJ device using a parallel nTron device. When a square pulse is applied to the nTron's gate, a triangle-like pulse flows through the channel of the SHE-MTJ device. (b) An nTron-like waveform synthesized by the AWG, observed by an oscilloscope. The pulse duration (falling time constant) is 2 ns. (c) Switching phase diagrams of the SHE-MTJ device under the applied field of -7.4 mT, using nTron-like pulses. (d) Bit error rate as the function of nTron-like pulse's peak voltage for AP to P transition under the applied field of -7.4 mT.

SUPPLEMENTAL INFORMATION

5.S1. Experimental setup

The 3-terminal MTJ devices are placed in a HPD (High Precision Devices, Inc.) cryogen-free chamber at a temperature of 3.1 K. An external magnetic field is applied by a superconducting magnet inside the chamber, driven by an AMI 430 controller. The sample is connected to outer measuring circuit (at RT) by RF probes spatially controlled by AttoCube motors.

Fig. 5.S1 shows the diagram of the measuring circuit. The state of the MTJ is read by following a small DC current of 3 μA through the tunnel barrier by a Keithley 2400 multimeter and reading the drop voltage by an NI-DAQmx USB-6361. The read voltages are then stored in the NI-DAQ's internal buffer memory (64MB) until being collected by the computer via USB connection. A Keysight M9502A arbitrary waveform generator (AWG) is responsible for sending reset pulses to the sample's channel, switching triggers to PSPL 10070A pulse generator and reading triggers to the NI-DAQ. The reset pulses are sent through a PSPL 5865 driver amplifier, powered by an HP 6237B power supply. The switching pulses from the PSPL generator are sent through a RFMD SA2113 voltage controlled attenuator (VCA), powered and controlled by two DAC outputs of an SR865 lock-in amplifier, before being combined with the amplified reset pulses by a Marki PD0218 180^{o} hybrid. The combined pulses pass through a Pasternack PE8212 DC block before entering the sample's channel.

The pulse sequence is illustrated in Fig. 5.S2, consisting of alternative reset and switching pulses (of opposite signs) each of which is followed by a reading trigger pulse. Each pulse sequence takes about 1 ms and is repeated 1024 times for each pair of pulse height and duration. The switching probability is determined by the expectation value of the Beta-distribution of 1024 switching attempts.

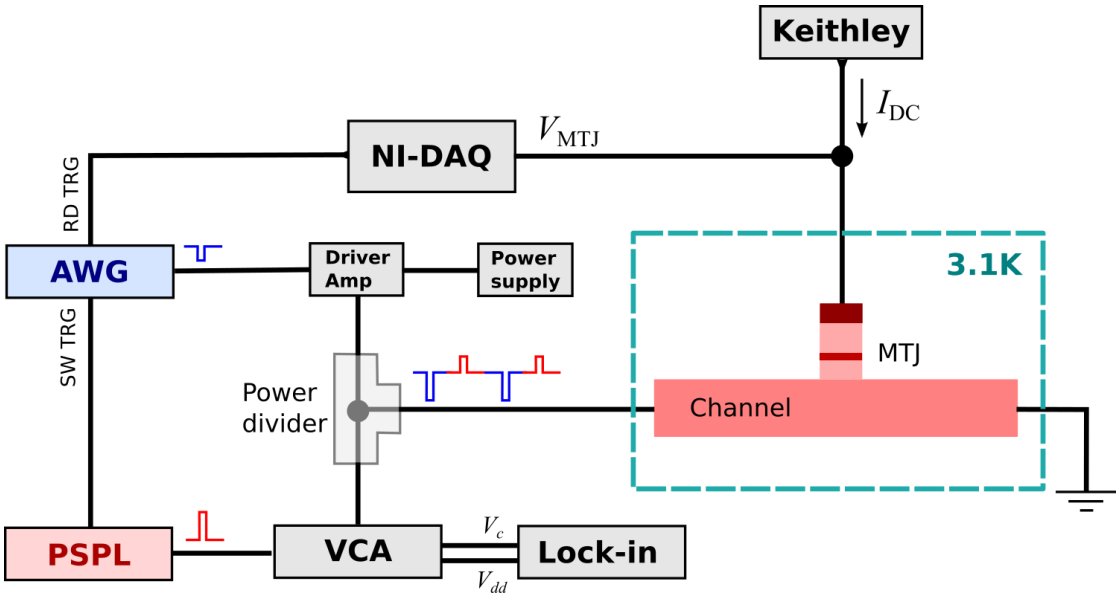

Figure 5.S1: Circuit diagram of the pulse switching measurement.

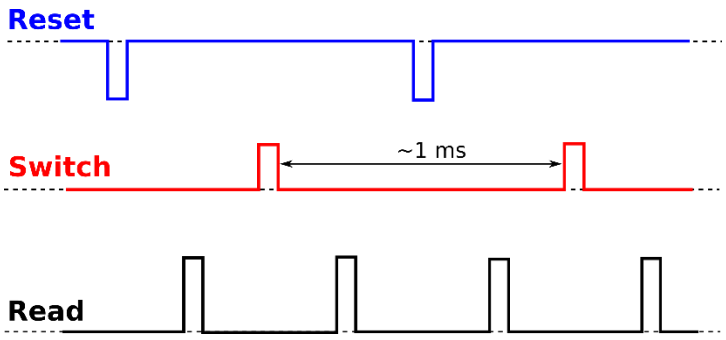

Figure 5.S2: Pulse sequence of the switching measurement, consisting of alternative reset and switching pulses with a reading trigger pulse after each one, taking about 1 ms for each switching attempt.

5.S2. Adaptive measuring method

To effectively measure switching phase diagrams on our devices, we deploy the adaptive measuring method which is illustrated by the flow chart in Fig. 5.S3. We notice that in the switching phase diagrams as shown in Fig. 5.2 (main text), the richest information gathers around the 50% switching probability boundary between the non-switched (red) at the lower left corner and near 100% switched (black) at the upper right corner. Thus it is more effective if most measuring points lie along the 50% probability boundary, instead of being distributed evenly over the *V*-*t* space. To achieve this, we carry out the experiment in multiple iterations (repetitions) after each of which the data set is collected, analyzed for determining the parameters for the next one. The effectiveness of this method is to tailor the parameters setting strategy so that the data points gather in the areas (on the parameters space) of richest information.

Assuming after one iteration we obtain a series of probability $P_i(V_i,t_i)$. To visually plot the data, we group the data points (V_i,t_i) into triangle by Delaunay triangulation, each of which is colored based on the average value of its vortices, as illustrated in Fig. 5.S4(b). We define a "weight function" $f_{i,j}=f(P_i,P_j)$ for each edge (V_i,t_i) and (V_j,t_j). For the edges whose weight meets a pre-defined criterium (in our case, 1-sigma above the average value of all edges), we add their midpoints to the list of data points to be measured in the next iterations. The finish condition is set to be the maximum number of iterations. Fig. 5.S4(b-d) shows the measuring progress during which the newly added points are located near the 50% probability boundary. Fig. 5.S4(e) shows the final result (without illustrative lines) which is identical to Fig. 5.2(a) in the main text.

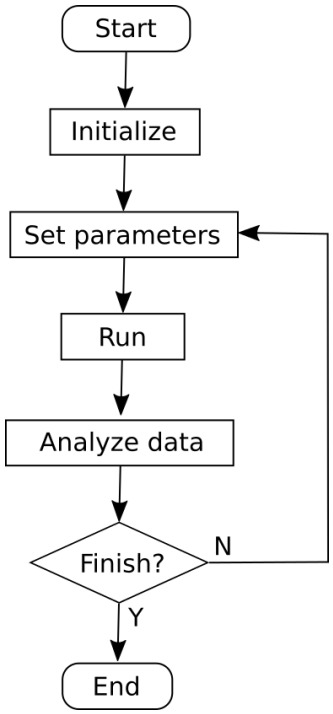

Figure 5.S3: Flow chart of the adaptive measuring automation program. The experimental data set after each run (iteration) with a given set of parameters is then analyzed for determining the parameters for the next iteration (if necessary). The finish condition and parameters setting are programmed so that the measurement effectively focuses on areas (on parameters space) with richest data.

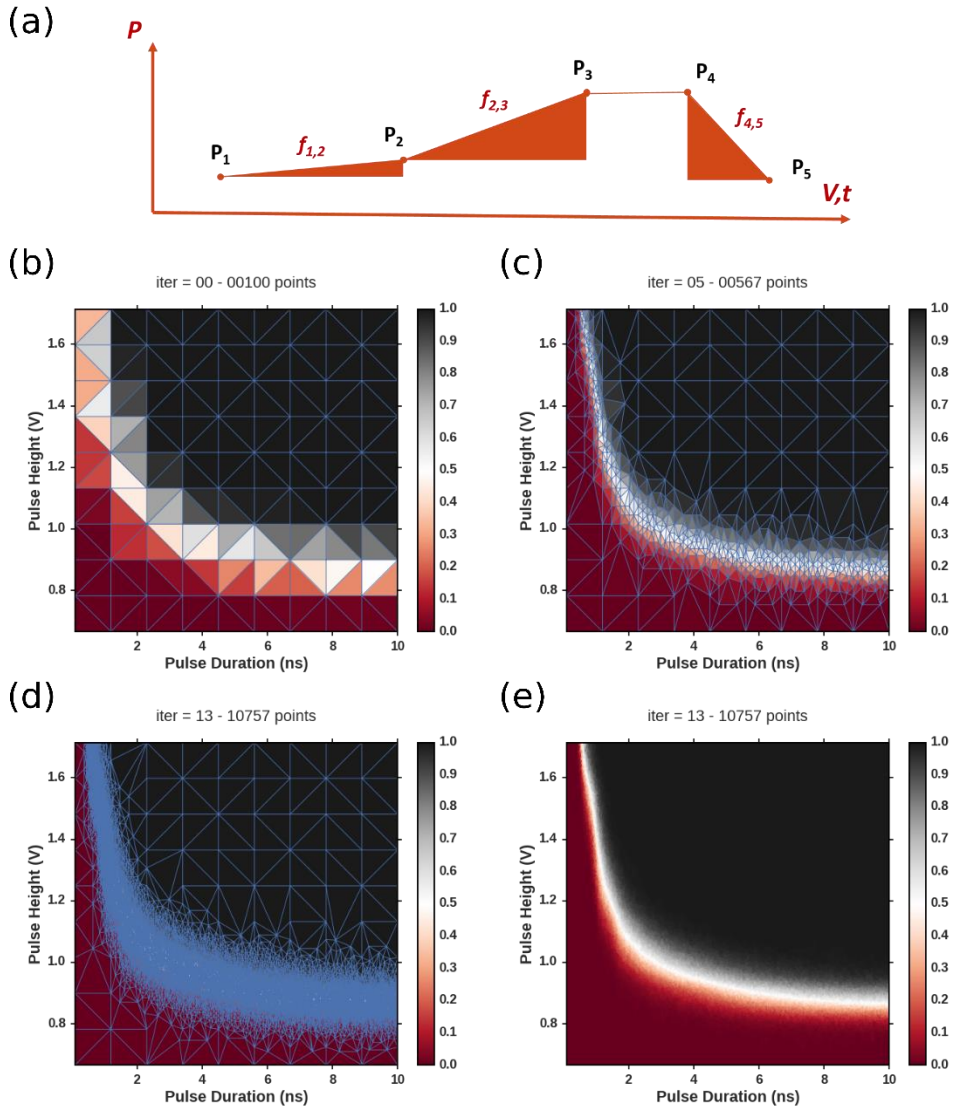

Figure 5.S4: Example of the adaptive method in measuring switching phase diagrams. (a) The weight functions is determined by the area of the "triangle" (integral) made by the switching probability and the 2 parametric axes. (b) The initial distribution of data points, evenly over the V-t space. The points are groups into non-overlapping triangles (thin lines) by Delaunay triangulation, each of which is colored based on the average value of its 3 vortices. (c) Results after 5 iterations (567 points). (d) Results after 13 iterations (10757 points) in which most data points lie along the 50% probability boundary. (e) Results as in (d) with the illustrative lines removed.

5.S3. Phase diagrams for long pulses

It is suggested [14] that the thermal stability $\Delta = E / k_B T$ (E: barrier energy, k_B: Boltzmann constant, T: temperature) of the sample can be estimated by performing switching measurements in the thermally activated regime (pulse duration ≥ 20 ns) in which the switching probability P (or read-disturb-rate in 2-terminal MTJ structure) varies with the pulse height as:

$$\ln P = \ln(t / \tau_0) - (1 - V / V_0) \cdot \Delta \qquad (5.S1)$$

for pulse height smaller than the critical voltage V_0 so that P is also very small $<10^{-2}$. For this measurement, we used a different sample from the same multilayer stacks, having a 330 nm × 600 nm channel and a 75 nm × 190 nm MTJ pillar (same aspect ratios as the channel's and the pillar's of the sample presented in the main text). The sample was annealed at 340 C for 1 hour in air under an applied field of 0.5 T. This annealing condition resulted in the good pinning of the reference layer of the MTJ as reflected by the sharp magnetic minor loop shown in Fig. 5.S5(a). The minor loop is centered at 3.0 mT, having a coercive field of 79 mT and TMR of 104% which are higher than those of the sample in the main text which was annealed in a different condition (at 300 C in vacuum under a field of 0.15 T).

The switching phase diagrams of the sample with pulse duration from 1 to 100 ns are shown in Fig. 5.S5(b). Note that the x-axis is plotted on a log scale. By fitting to the macrospin model, given by equation (5.1), to the short pulse duration (<10 ns), assuming the typical value of 1 ns for τ_0, the values of the critical voltage are estimated to be 1.3 V for AP to P and 1.0 V for P to AP, which are about 20% higher than the values estimated for the device in the main text (having 230 nm channel) which can be attributed to differences in channel geometry and resistance and device variation. We then performed switching measurements with pulses having amplitudes around V_0 and long durations, as shown in Fig. 5.S5(c). By fitting the linear part of switching probability

versus pulse height curve to equation (5.S1), the estimated values of the thermal stability factor Δ are 109 ± 12 for AP to P and 110 ± 12 for P to AP. Note that the thermal stability at RT is 44 (T = 300 K), estimated from DC switching measurements [6]. Assuming the same energy barrier in both cases, we can roughly estimate the actual temperature of our sample to be $T = 44 \times 300$ K / 110 = 120 K. This high value, compared to the ambient temperature of $T_0 = 3.1$ K, indicates a large Joule heating caused by the switching current. Note that the heating effect occurs in RT measurements as well, thus the sample's temperature can be different from the value of 300 K that we assume above.

We attempt to estimate the sample's temperature following the simple model $T(j) = T_0 + \kappa j^2$ (j: current density), where κ is a constant whose value is assumed to be 5×10^{-22} K m^4/A^2 [15] (as measured for Pt/Co multilayers). In DC measurements at RT in Ref. [6], the current density is about 2×10^{11} A/m^2, so the sample's temperature is about 340 K. In our measurements shown in Fig. 5.S6, we applied pulses with voltage from 1.0 V to 1.4 V, corresponding to current density of $6 – 8 \times 10^{11}$ A/m^2. Based on the simple model above, the sample's temperature in this case can be about 180 – 320. Thus the expected value of the sample's temperature of 44 × 340 K / 110 = 140 K, from the values of Δ above, is not unreasonable. We emphasize that these estimations of the sample's temperature are very coarse since many approximations are used. The value of the constant κ cited above depends on the particular multilayer structure and geometry which determine resistivities, current distribution and heat dissipation. Finally, the equation (5.S1) assumes constant thermal stability factor Δ, and consequently constant temperature T given the same energy barrier E, while this may hold for $T_0 = 300$ K (RT) but it may not accurately describe our results at cryogenic temperatures since $T(j)$ varies strongly with j for small T_0.

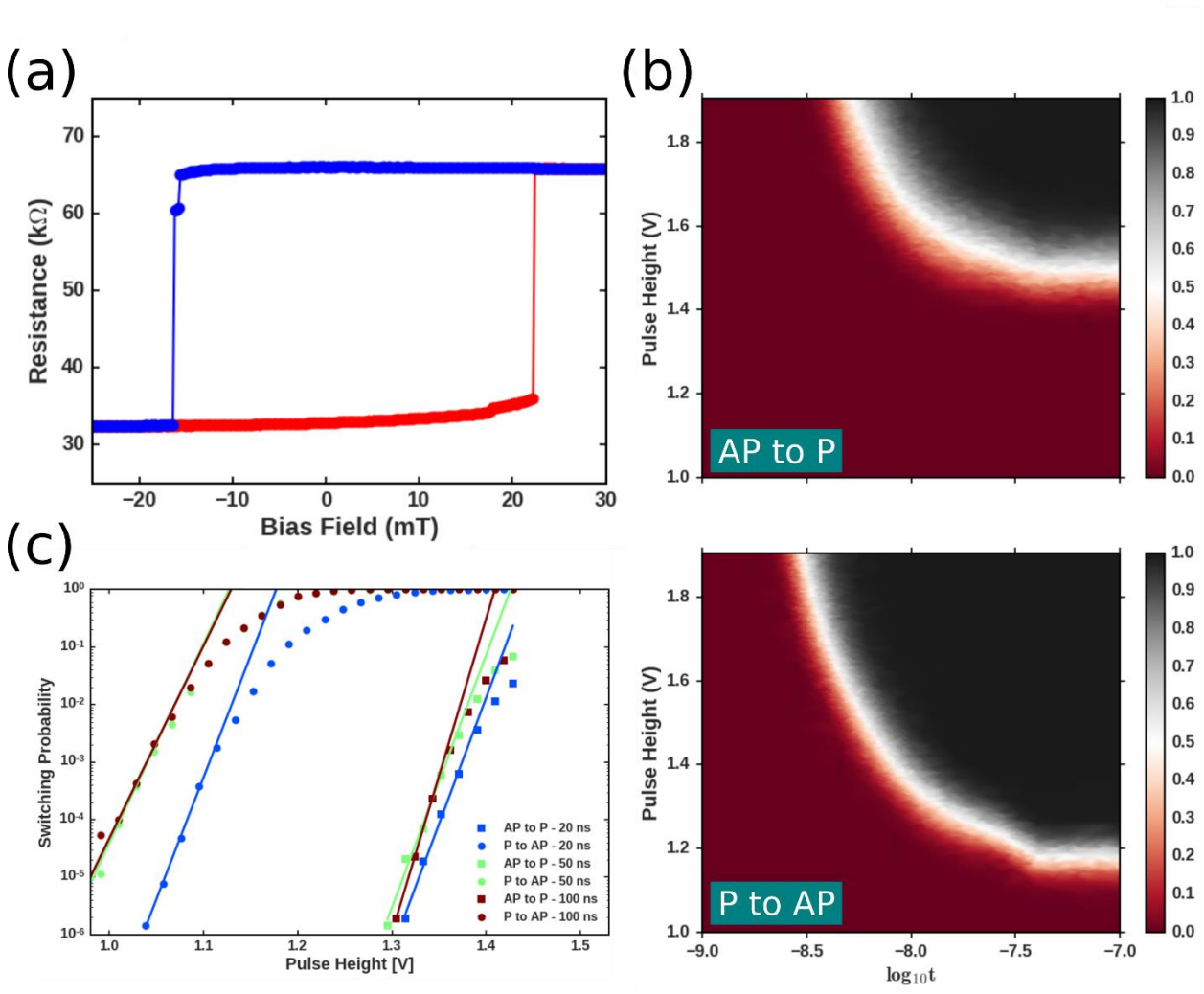

Figure 5.S5: (a) Field-switching behavior of the sample. (b) Switching phase diagrams of the SHE-MTJ devices for AP to P (top) and P to AP (bottom) transitions for pulse duration 1 – 100 ns. (c) Switching probability in log scale as a function of pulse voltage for long pulse durations for AP to P (squares) and P to AP (circles). From the linear fit to the linear part of the curves, the values of the thermal stability are estimated to be 109 ± 12 for AP to P and 110 ± 12 for P to AP.

REFERENCES

[1] A. D. Kent and D. C. Worledge, Nat. Nanotech. **10**, 187 (2015).

[2] L. Liu, C.-F. Pai, Y. Li, H. W. Tseng, D. C. Ralph, and R. A. Buhrman, Science **336**, 555 (2012).

[3] L. Liu, T. Moriyama, D. C. Ralph, and R. A. Buhrman, Phys. Rev. Lett. **106**, 036601 (2011).

[4] M.-H. Nguyen, C.-F. Pai, K. X. Nguyen, D. A. Muller, D. C. Ralph, and R. A. Buhrman, Appl. Phys. Lett. **106**, 222402 (2015).

[5] C.-F. Pai, L. Liu, Y. Li, H. W. Tseng, D. C. Ralph, and R. A. Buhrman, Appl. Phys. Lett. **101**, 122404 (2012).

[6] S. V. Aradhya, G. E. Rowlands, J. Oh, D. C. Ralph, and R. A. Buhrman, Nano Lett. **16**, 5987 (2016).

[7] A. N. McCaughan and K. K. Berggren, Nano Lett. **14**, 5748 (2014).

[8] J. Z. Sun, Phys. Rev. B **62**, 570 (2000).

[9] R. H. Koch, J. A. Katine, and J. Z. Sun, Phys. Rev. Lett. **92**, 088302 (2004).

[10] G. E. Rowlands, S. V. Aradhya, S. Shi, E. H. Yandel, J. Oh, D. C. Ralph, and R. A. Buhrman, Appl. Phys. Lett. **110**, 122402 (2017).

[11] E. B. Myers, F. J. Albert, J. C. Sankey, E. Bonet, R. A. Buhrman, and D. C. Ralph, Phys. Rev. Lett. **89**, 196801 (2002).

[12] Y. Ou, C. F. Pai, S. Shi, D. C. Ralph, and R. A. Buhrman, Phys. Rev. B **94**, 140414(R) (2016).

[13] S. Emori, T. Nan, A. M. Belkessam, X. Wang, A. D. Matyushov, C. J. Babroski, Y. Gao, H. Lin, and N. X. Sun, Phys. Rev. B **93**, 180402 (2016).

[14] R. Heindl, W. H. Rippard, S. E. Russek, M. R. Pufall, and A. B. Kos, J. Appl. Phys. **109**, 073910 (2011).

[15] O. J. Lee, L. Q. Liu, C. F. Pai, Y. Li, H. W. Tseng, P. G. Gowtham, J. P. Park, D. C. Ralph, and R. A. Buhrman, Phys. Rev. B **89**, 024418 (2014).

CHAPTER 6

Efficient Switching of 3-Terminal Magnetic Tunnel Junction Devices by the Giant Spin Hall Effect of $Pt_{85}Hf_{15}$ Alloy

Minh-Hai Nguyen[1], Shengjie Shi[1], Sriharsha V. Aradhya[1],

D. C. Ralph[1,2], R. A. Buhrman[1]

[1] *Cornell University, Ithaca, New York 14853, USA*

[2] *Kavli Institute at Cornell, Ithaca, New York 14853, USA*

ABSTRACT

The three-terminal magnetic tunnel junction (3T-MTJ) structure, powered by the strong spin Hall effect (SHE) of the channel, has demonstrated low-powered, fast and reliable switching and has become a promising candidate for magnetic memory technology. The spin torque efficiency of $Pt_{85}Hf_{15}$ alloy is reported to be about twice that of pure Pt, due to the intrinsic SHE of Pt. We report a large reduction in critical current density of the in-plane magnetized 3T-MTJ devices using a $Pt_{85}Hf_{15}$ channel, about 3 times for DC and 2 times for pulse switching, in comparison to the pure Pt counterpart. We also observe a strong linear dependence of the DC critical current on the coercive field and bias field which indicates that the switching mechanism is more complex than indicated by the macrospin spin-torque model.

MAIN TEXT

Magneto-resistive random access memories (MRAM) have drawn a great deal of attention from the electronic and spintronic community due to their inherent nonvolatility which enables long data retention and low standby power [1]. The most common MRAM type is the two-terminal magnetic tunnel junction (MTJ) structure in which an electrical current is applied through the MTJ layers to switch the magnetization of the ferromagnetic (FM) free layer parallel (P) or anti-parallel (AP) to the fixed magnetization of the FM reference layer via the spin transfer torque [2]. To avoid the breakdown of the tunnel barrier due to the writing current and the read disturb errors associated with the two-terminal geometry, recently a three-terminal MTJ (3T-MTJ) structure based on the spin Hall effect (SHE) [3–5] has been proposed [6]. In the 3T-MTJ structure, the FM free layer of the MTJ is switched by the anti-damping torque of the transverse spin current induced by the SHE of the adjacent channel. The separation of the write and read paths allows flexibility in optimizing the performance of the devices without the trade-offs required in their two-terminal counterpart. Furthermore, nanosecond fast and reliable switching of these 3T-MTJ devices has been recently demonstrated [7] and attributed to the role of the field-like torques and micromagnetic dynamics in reducing the incubation delay [8]. These advantages make the 3T-MTJ structure an attractive candidate for MRAM applications.

The critical current density of in-plane 3T-MTJ devices is proportional to the Gilbert magnetic damping α, which is the sum of the intrinsic damping of the FM layer and the enhanced damping by the spin pumping effect, and inversely proportional to the damping-like spin torque efficiency $\xi_{DL} = T_{int}\,\theta_{SH}$, where $T_{int} < 1$ is the spin transparency of the interface and θ_{SH} is the spin Hall ratio of the channel. It has been reported that interfacial engineering can effectively reduce the damping α [9,10] and improve the interfacial transparency T_{int} [11,12]. Concurrently, efforts

have been made into searching for strong SHE materials, such as Pt [13,9], β-Ta [6], β-W [14], Pd [15], their oxides [16,17] and binary alloys [18–24]. Recent evidence has shown that the intrinsic SHE, in which the spin Hall ratio scales linearly with the resistivity, is the dominant mechanism in Pt [25–29]. This opens up the opportunity to further enhance the spin Hall ratio of Pt by introducing impurities into the bulk to increase the resistivity. Previously we have demonstrated that the $Pt_{85}Hf_{15}$ alloy exhibits 2-3 times higher spin torque efficiencies, depending on the particular interface, than pure Pt in perpendicularly magnetized samples [18]. Thus it is interesting and technological important to investigate the performance of in-plane 3T-MTJ devices having a $Pt_{85}Hf_{15}$ channel.

We measure two series of 3T-MTJ devices, without and with a thin 0.7 nm Hf spacer, which have the multilayer stacks of SiO_x | Ta(1) | PtHf(6) | Hf(0 or 0.7) | FeCoB(1.4) | MgO | FeCoB(1.2) | Ta(0.2) | FeCoB(1.2) | FeCo(1) | Ru(0.85) | FeCo(2.5) | IrMn(7) | Ru(4) (thicknesses in nm, PtHf = $Pt_{85}Hf_{15}$, FeCoB = $Fe_{60}Co_{20}B_{20}$), DC and RF magnetron sputter-deposited onto thermally oxidized high-resistivity Si wafers by Canon ANELVA, Inc. The 1 nm Ta layer at the bottom provides a smooth surface for the 6 nm PtHf channel layer. The thin 0.7 nm Hf spacer between the channel and the 1.4 nm FeCoB FM free layer in one series helps reduce the magnetic damping as reported in Ref. [9]. The magnetization of the FeCoB ferromagnetic reference layer is pinned by the IrMn layer atop the FM/Ru/FM synthetic antiferromagnetic structure. The stacks are patterned into 3T-MTJ devices and annealed in an applied magnetic field by the same processes previously reported [7]. All measurements are performed at room temperature. Fig. 6.1(a) shows the tilted SEM image of the channel and MTJ pillar (with e-beam resist on top) of a device in the series after the ion-mill etching of the pillar. The size of the channel is measured by AFM image to be 440 nm × 600 nm. The channel resistance is about 2.5 kΩ, more than 2 times higher than

similar devices having a pure Pt channel [7] due to the high resistivity of the PtHf channel [18]. The MTJ pillars have two different sizes: 45 nm × 190 nm for HA devices (high aspect ratio = 1:4.2) and 110 nm × 190 nm for LA devices (low aspect ratio = 1:1.7).

The DC measuring circuit is illustrated in Fig. 6.1(a). The state of the MTJ is determined by reading the voltage drop across the MTJ while flowing a small oscillating current through it at a frequency of 1337 Hz by a lock-in amplifier. Fig. 6.1(b) shows the magnetic hysteresis (minor) loops of the MTJ, centered by an offset value H_{off}, (about 0 and -4.5 mT for samples without and with Hf spacer), when an external field is swept parallel to the easy axis of the MTJ by a Helmholtz electromagnet, of HA devices. All devices exhibit sharp field switching behavior. The coercive field of the device without spacer is high ~ 8.5 mT, while that of the one with spacer is much lower ~3.2 mT.

To perform DC current switching, a DC current is applied to the channel to manipulate the magnetization of the free layer, under an applied field H_{off} to bias the free layer into the bi-stable state. The MTJ resistance versus quickly sweeping DC current is shown in Fig. 6.1(c). Note that in our convention, the positive (external) field is in the same direction as the current-induced Oersted field in the free layer (and therefore the spin accumulation). The critical current of the device with the Hf spacer is 0.16 mA, nearly 3 times smaller than that of the one without the spacer which is 0.4 mA. However, the DC critical current I_c depends on the current ramp-rate, as given by the thermally activated model [30,31]:

$$I_c = I_0\left[1+\frac{1}{\Delta}\ln\left(\left|\frac{\dot{I}}{I_0}\right|\tau_0\Delta\right)\right], \qquad (6.1)$$

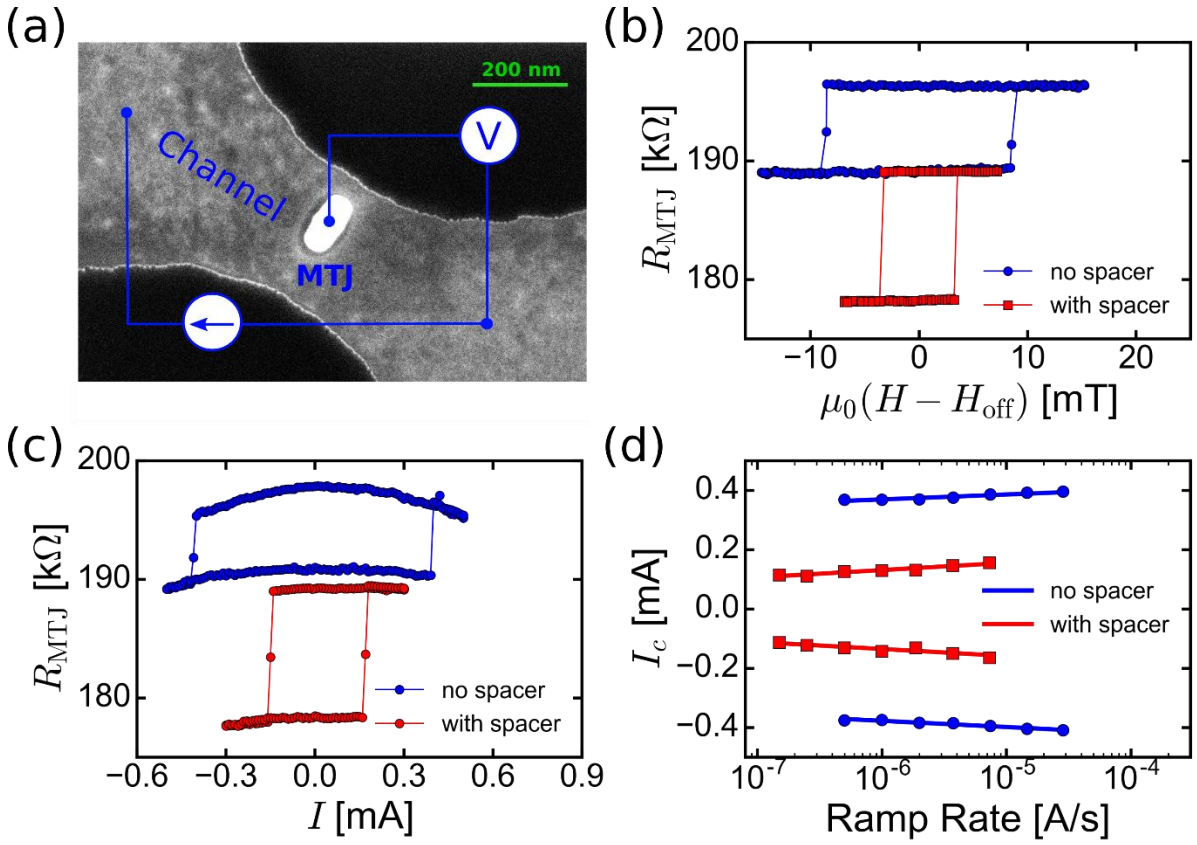

Figure 6.1: (a) Tilted SEM image of a 3T-MTJ device in the series and the basic schematic of the DC measuring circuit. (b) Magnetic minor loop and (c) DC current switching behavior of HA devices without Hf spacer (blue) and with a 0.7 nm Hf spacer (red). The lines are guide to the eyes. (d) DC critical currents versus current ramp-rates for P to AP (positive) and AP to P (negative) transition. The solid lines showed fitted results to the thermally activated switching model. The fitted parameters are summarized in Table 6.1.

where I_0 is the critical current at zero thermal fluctuation, $\Delta = E / k_B T$ the thermal stability factor (E: barrier energy, k_B: Boltzmann constant, T: temperature = 300 K) , $\dot{I}$ the current ramp-rate, and τ_0 the thermal fluctuation time (taken to be 1 ns). The current ramp-rate results for HA devices and fitted lines to equation (6.1) are shown in Fig. 6.1(d). The fitted values of I_0 and Δ, averaged over two identical samples, are respectively ±0.56 ± 0.03 mA, 70 ± 13 for the device without spacer and ±0.38 ± 0.03 mA, 36 ± 8 for the one with Hf spacer (positive (negative) currents are for P to AP (AP to P) transition). These results, together with the values of magnetic damping α and effective field M_{eff} estimated by ferromagnetic resonance measurements (see section 6.S1 of Supplemental Information), are listed in Table 6.1 for our HA PtHf devices and the sample reported in Ref. [7] having the same MTJ aspect ratio, slightly thicker free layer (1.6 nm) and pure Pt channel. The spin torque efficiency ξ_{DL} is calculated from the above parameters by the relation [32]:

$$\xi_{\text{DL}} = \frac{2e}{\hbar} \mu_0 M_s t_{\text{FeCoB}} \alpha \left(H_c + M_{\text{eff}} / 2 \right) / J_0^{\text{DC}}, \qquad (6.2)$$

where $\mu_0 = 4\pi \times 10^{-7}$ N/A^2 is the vacuum permeability, M_s the saturation magnetization, assumed to be 1.2×10^6 A/m (no magnetic dead layer) [7] for all samples, H_c the coercive field determined from the minor loops shown in Fig. 6.1(b) and J_0^{DC} the DC critical current density (absolute value).

Table 6.1: Fitted parameters from FMR, DC and pulse switching measurements of PtHf 3T-MTJ devices, in comparison with the Pt one reported in Ref. [7]. All devices have the same channel size of 330 nm × 600 nm and MTJ size of 45 nm × 190 nm (HA: high aspect ratio = 1:4.2).

Structure	**Pt(5) | Hf(0.7) | FCB(1.6)** **Pt with spacer [7]**	**PtHf(6) | FCB(1.4)** **PtHf no spacer**	**PtHf(6) | Hf(0.7) | FCB(1.4)** **PtHf with spacer**
FMR measurements			
M_{eff} **[Oe]**	4165	3257	3494
α **[×10^{-3}]**	18	26 ± 2	19 ± 1
DC switching measurements			
Δ **[k$_B$T]**	54 ± 5	70 ± 13	36 ± 8
J_0^{DC} **[×10^{11}A/m^2]**	4.0	2.2 ± 0.2	1.4 ± 0.1
ξ_{DL}	0.055	0.098	0.119
Pulse switching measurements			
J_0^{pulse} **[×10^{11}A/m^2]**	6.3	4.5	3.4
t_0 **[ns]**	1.1	0.2	0.4

From Table 6.1, it is readily seen that our samples with 1.4 nm free layer have consistently lower M_{eff} which is most likely due to the thinner free layer which provides stronger out-of-plane anisotropy to reduce the in-plane effective field. The magnetic damping constants of the devices having the Hf spacer are about 30% smaller than that of the one without spacer which we attribute to the role of the Hf spacer in reducing the interfacial spin memory loss [9,33]. Most remarkably, the spin torque efficiencies of the devices having PtHf alloy channel are ~0.11, about 2 times higher than that of the one having pure Pt channel which is consistent with the results measured on perpendicularly magnetized Pt/Co bilayers [18]. Finally, these higher values of spin torque efficiency in combination with lower M_{eff} and slightly thinner free layer result in ~2 times lower J_0^{DC} for the PtHf device without spacer, and ~3 times lower for device with Hf spacer, comparing to the sample having pure Pt channel and Hf spacer. We also note that the thermal stability factor, as well as the coercive field, of the PtHf sample having a Hf spacer is nearly 2 times lower than that of the one without a spacer. Since the structural difference between the two series of samples is the presence of a Hf spacer, we speculate that the difference in the thermal stability and coercive field is due to some unknown effect of the Hf atoms on the curling of the magnetic profile and/or the magnetic subdomains of the FM free layer.

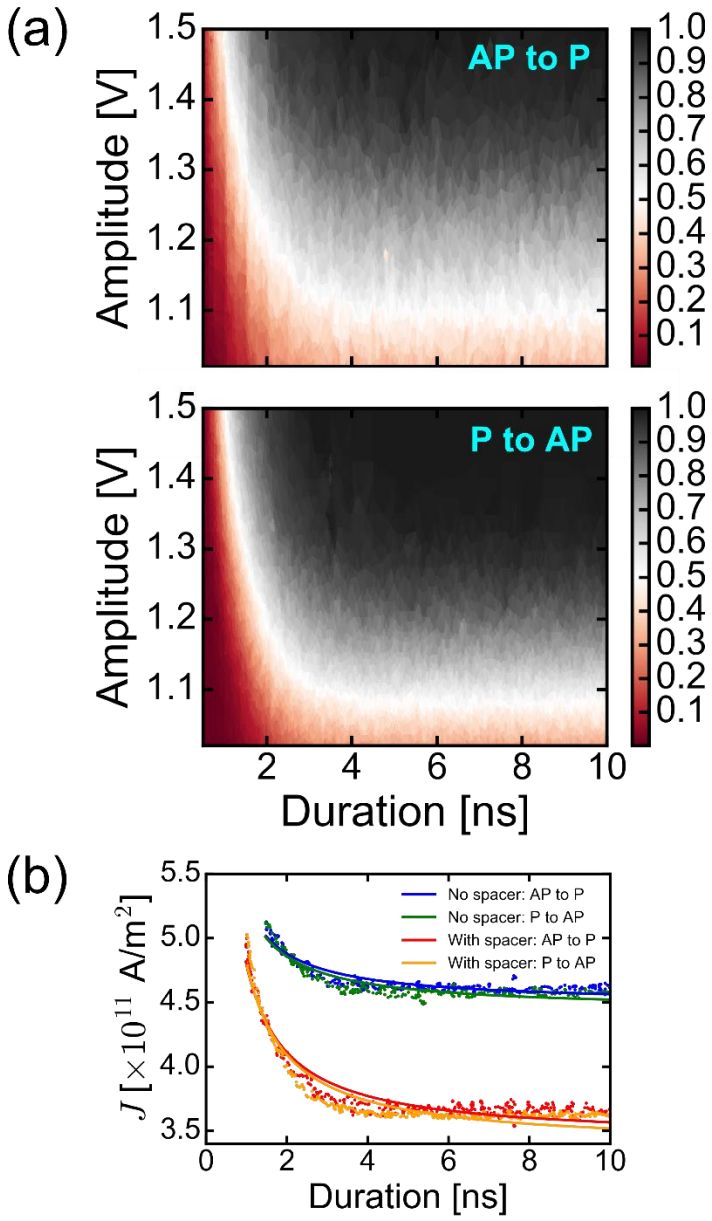

Figure 6.2: Pulse switching measurements on HA devices. (a) Switching phase diagrams of an HA device with a Hf spacer for AP to P (upper) and P to AP (lower) transition. (b) 50% switching probability points (white points in (a), after dividing by the channel's cross-sectional area and resistance and corrected for wave reflection at the probe's tip) for HA devices with and without a Hf spacer. The solid lines show fitted results to the macrospin model. The fitted parameters are summarized in Table 6.1.

We then perform nanosecond pulse switching measurements on the PtHf devices. The measuring circuit and method are described in details in section 6.S2 of Supplemental Information. Fig. 6.2(a) shows the switching phase diagrams of an HA device with spacer for varying pulse amplitude (absolute value) and duration, in which each switching probability is averaged over 1000 switching attempts, under applied fields H_{off} at the center the minor loops. The 50% switching probability points (white areas) are plotted in Fig. 6.2(b), together with those of another HA device without spacer, in which the pulse current is calculated from the pulse amplitude, channel resistance and geometry, taking into account the wave reflection at the tip of the probe due to the impedance mismatch of the channel (having a typical resistance of 2.5 kΩ). By fitting the 50% probability points to the macrospin model [32,34]:

$$J_{50\%} = J_0^{\text{pulse}}(1 + t_{50\%} / t_0), \tag{6.3}$$

we estimated the values of (pulse) critical current density J_0^{pulse} and time t_0, as listed in Table 6.1. The deviation of the fitted lines shown in Fig. 6.2(b) from the data points suggests that the switching mechanism is not solely anti-damping macrospin switching but largely affected by the distribution and evolution of magnetic domains of the free layer by the anti-damping spin torque and the field-like torques induced by the electrical and/or spin current, as fully discussed in Ref. [8]. As listed in Table 1, the values of J_0^{pulse} are about 2 – 3 times higher than their DC counterpart J_0^{DC}, mainly due to the different physical meanings of J_0. The pulse J_0^{pulse} is defined as the asymptotic minimum of the 50% boundary, described by equation (6.3). The DC J_0^{DC} is critical current density of indefinitely long pulses, thus is equivalent to the asymptotic minimum of the boundary between zero and non-zero switching probability regions in the phase diagram. The device without spacer exhibits 1.4 times lower J_0^{pulse} and the device with the Hf spacer nearly

2 times lower than that of the one with pure Pt channel, qualitatively consistent with the corresponding DC results. The PtHf devices also show equally or even faster switching speed comparing to their pure Pt counterpart.

We perform the same DC and pulse measurements on 110 nm × 190 nm LA PtHf devices with Hf spacer. For this series, we observe a variation of coercive field H_c which we attribute to the weak in-plane anisotropy and edge effect. The fitted parameters from DC and pulse measurements are shown in Fig. 6.3(a) as functions of H_c. The results for the LA device having highest $\mu_0 H_c$ = 2.4 mT, close to that of the HA device (with spacer), are similar to those of the HA device, indicating no significant effect of the MTJ aspect ratio. Interestingly, although J_0^{pulse} for LA devices varies around 3.5×10^{11} A/m^2 and $t_0 < 1$ ns with no clear trend (within a large fitting uncertainty), J_0^{DC} and Δ show a strong dependence on H_c. Δ varies linearly 6.2 ± 0.4 $k_B T$/mT with H_c. On the other hand, J_0^{DC} shows a strong variation of more than a factor of 2 and nearly linear $(0.40 \pm 0.04) \times 10^{11}$ A/m^2 per mT with H_c, which is inconsistent with equation (6.2), based on the anti-damping spin-torque switching mechanism, when M_{eff} is much larger than H_c as is the case. This strong dependence of J_0^{DC} on H_c indicates the involvement of field-assisted switching mechanism in combination with SHE-induce anti-damping spin torque. We note however that the current switching of our samples cannot be solely explained by field switching due to the current-induced Oersted field because the Oersted field in our measurements is $\mu_0 H_s / J$ = 0.38 mT per 10^{11} A/m^2, which is considerable but always smaller than the coercive fields.

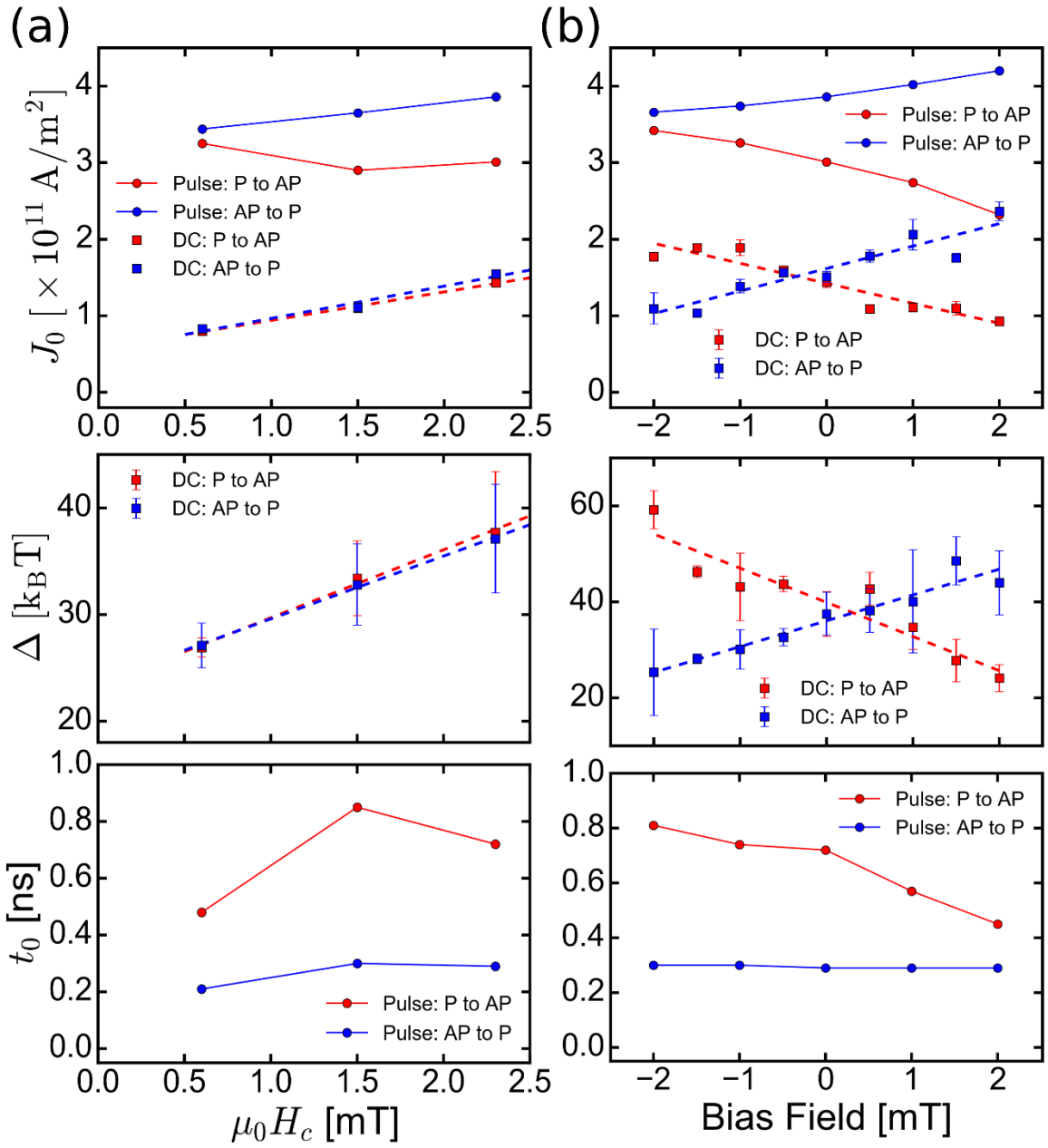

Figure 6.3: DC (squares) and pulse (circles) critical current density, thermal stability factor and pulse critical time for P to AP (red) and AP to P (blue) transition as functions of coercive fields of different LA devices (a) and as functions of bias field for an LA device having coercivity of 2.4 mT (b). The dashed lines show linear fitted results. The solid lines are guides to the eyes.

To study the effect of field-assisted switching mechanism, we perform similar DC and pulse measurements with varying bias field $H = H_{ext} - H_{off}$ for the LA sample having H_c = 2.4 mT. As shown in Fig. 6.3(b), the (fitted) results (versus bias field) are similar to those shown in Fig. 6.3(a) versus coercive fields. In particular, t_0 < 1 ns without a clear trend. J_0^{pulse} shows a weak (linear) variation with bias field, about 20% for AP to P and 30% for P to AP. Since the pulse data do not fit well to the macrospin model (see section 6.S3), we cannot make a more quantitative judgment. On the other hand, J_0^{DC} and Δ vary strongly and linearly with the bias field. This is understood by the thermally assisted switching picture in which the bias field modifies the effective energy barrier, resulting in the variation of the thermal stability factor and critical current as [30]:

$$\begin{aligned} \Delta(H) &= \Delta(0)\cdot(1 \pm H / H_0) \\ J_0^{DC}(H) &= J_0^{DC}(0)\cdot(1 \pm H / H_s) \end{aligned}, \qquad (6.4)$$

where $H = H_{ext} - H_{off}$ is the bias field, H_0 and H_s are constants and the plus (minus) sign corresponds to AP to P (P to AP) transition. From the linear fit to equation (4) (shown as dashed lines in Fig. 6.3(b)), we estimated $\mu_0 H_0$ = 6.0 ± 0.6 mT and $\mu_0 H_s$ = 5.4 ± 0.8 mT. These overlapping values and the strong linear dependence of J_0^{DC} on H_c suggest the role of field-like effects, induced by the electrical and/or spin current, in the switching mechanism of the MTJs. In the spin-torque picture without significant field-assist one [30], we expect $H_s >> H_0$, consequently the field-dependence of J_0^{DC} is much less profound than that of Δ, which does not hold in this case. The Oersted field is in the same direction as the spin accumulation and has considerable magnitude of about 0.2 – 0.5 of H_c at switching current density shown in Fig. 6.3(a), thus cannot be ignored in the macrospin reversal mechanism. Moreover, the SHE-induced spin torque is generally accompanied by a small field-like torque which is reported in many multilayer systems [35–37]. We speculate that the combination of spin torque and field assisted macrospin mechanisms may explain the above

results, at least qualitatively. Furthermore, micromagnetic simulations [8] show that the field-like torque plays an important role in the evolution and reversal of magnetic domains of the free layer, consequently strongly affecting the critical current and switching speed. Thus, it is possible to improve the performance of the 3T-MTJ devices by harnessing the field-assisted switching mechanism with the Oersted and/or bias field.

In conclusion, we demonstrate the enhanced spin torque efficiency of PtHf alloy, due to the intrinsic SHE in Pt, by DC and nanoseond pulse current switching of the 3T-MTJ devices having PtHf channels and a thin Hf spacer. We achieve the critical current density of 3 times lower for DC and 2 times lower for pulse compared to a pure Pt channel, and confirm a 2 times higher spin torque efficiency. These results suggest the opportunity to improve the power consumption of the magnetic switching devices by alloying and interface engineering. We also observe a strong linear dependence of the DC critical current density and thermal stability factor on the coercive field of the samples and the bias field, while the pulse critical current density and speed do not show significant variation. These variations indicate the role of the field-assisted switching mechanism, by the Oersted field and/or SHE-induced field-like torque, in combination with spin-torque assisted and thermally activated ones, which suggests the possibility of further reducing the critical current density by utilizing the field-like effects.

The research is based upon work supported by the Office of the Director of National Intelligence (ODNI), Intelligence Advanced Research Projects Activity (IARPA), via contract W911NF-14-C0089. Additionally, this work was supported by Samsung Electronics Corp. and the NSF/MRSEC program (DMR-1120296) through the Cornell Center for Materials Research. This work was performed in part at the Cornell NanoScale Facility, a member of the National Nanotechnology Coordinated Infrastructure (NNCI), which is supported by the National Science

Foundation (Grant ECCS-1542081).

SUPPLEMENTAL INFORMATION

6.S1. Ferromagnetic Resonance measurements

To estimate the Gilbert magnetic damping and effective field, we performed flip-chip ferromagnetic resonance (FMR) measurements on our stacks. The technique is fully described in the Supplemental Information of Ref. [7]. Fig. 6.S1(a) shows a typical FMR lineshape for the PtHf sample with Hf spacer at excitation frequency f = 8 GHz. By fitting to the derivative Lorentzian function, the resonance field H_0 and linewidth LW of the FMR lineshape are obtained and plotted in Fig. 6.S1(b,c). The effective field M_{eff} is estimated by fitting to the Kittel equation:

$$f = \frac{\gamma}{2\pi}\mu_0\sqrt{H_0(H_0 + M_{\text{eff}})}, \qquad (6.S1)$$

where γ is the gyromagnetic ratio (also a fitting parameter) and $\mu_0 = 4\pi \times 10^{-7}$ N/A^2 the vacuum permeability. The damping coefficient α is similarly estimated by linear fitting to the relation:

$$LW = f \cdot \frac{2\pi}{\gamma}\alpha + LW_0. \qquad (6.S2)$$

The results are listed in Table 1 in the main text. Note that for the sample with Hf spacer, we fit the equation (6.S2) to the linear portion of the data at high frequencies > 4 GHz, as shown in Fig. 6.S1(b).

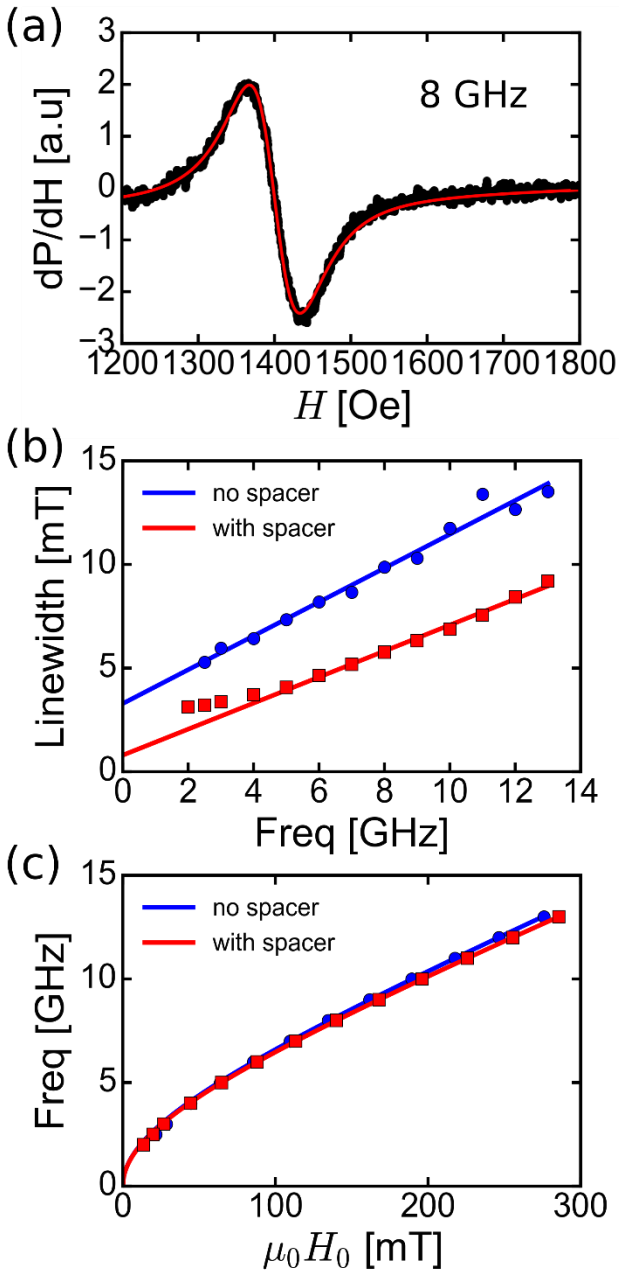

Figure 6.S1: (a) A typical FMR lineshape (shown for sample with Hf spacer at 8 GHz) and a fitted line to the derivative Lorentzian function. (b) Linewidth of FMR lineshape as a function of frequency. Solid lines show linear fitted results. (c) Frequencies versus resonance fields. Solid lines show fitted results to Kittel formula.

6.S2. Pulse switching measurement method

Fig. 6.S2 shows the diagram of the pulse switching measuring circuit, which is similar to that shown in Fig. 6.S1 of Chapter X. The state of the MTJ is determined by measuring the drop voltage across the tunnel barrier when flowing a small current 1 μA through it by a Keithley 2450 digital multimeter. The read voltages are then stored in the internal memory of a NI-DAQmx USB-6361 (up to 64MB) until being transferred to the computer through USB connection. The NI-DAQ is also responsible for sending trigger pulses to two Picosecond Pulse Labs generators for generating reset (PSPL 10070A) and switching (PSPL 10100A) pulses. The switching pulses from the PSPL with resolution of 1 dB go through a Mini-Circuits voltage controlled attenuator (VCA ZX73), which is supplied and controlled by the DAC output of a Signal Recovery 7265 DSP Lock-in amplifier and a Yokogawa 7651 power supply, before being combined with the reset pulses at a Picosecond 5331 power split. A GMW 5403 Electromagnet is used to apply an external field parallel to the easy axis of the MTJ.

For each switching attempt, a reset pulse (of opposite sign to the switching pulse) is sent to the channel to reset the state of the MTJ before a switching pulse. The switching probability is determined by the ratio of successfully switched counts over the successfully reset counts in 1000 attempts. The swiching probability points are grouped into non-overlapping triangles by Delaunay triangulation each of which is colored based on the average value of its vertices. We also employed the adaptive measuring strategy which is described in detail in section 5.S1 of chapter 5.

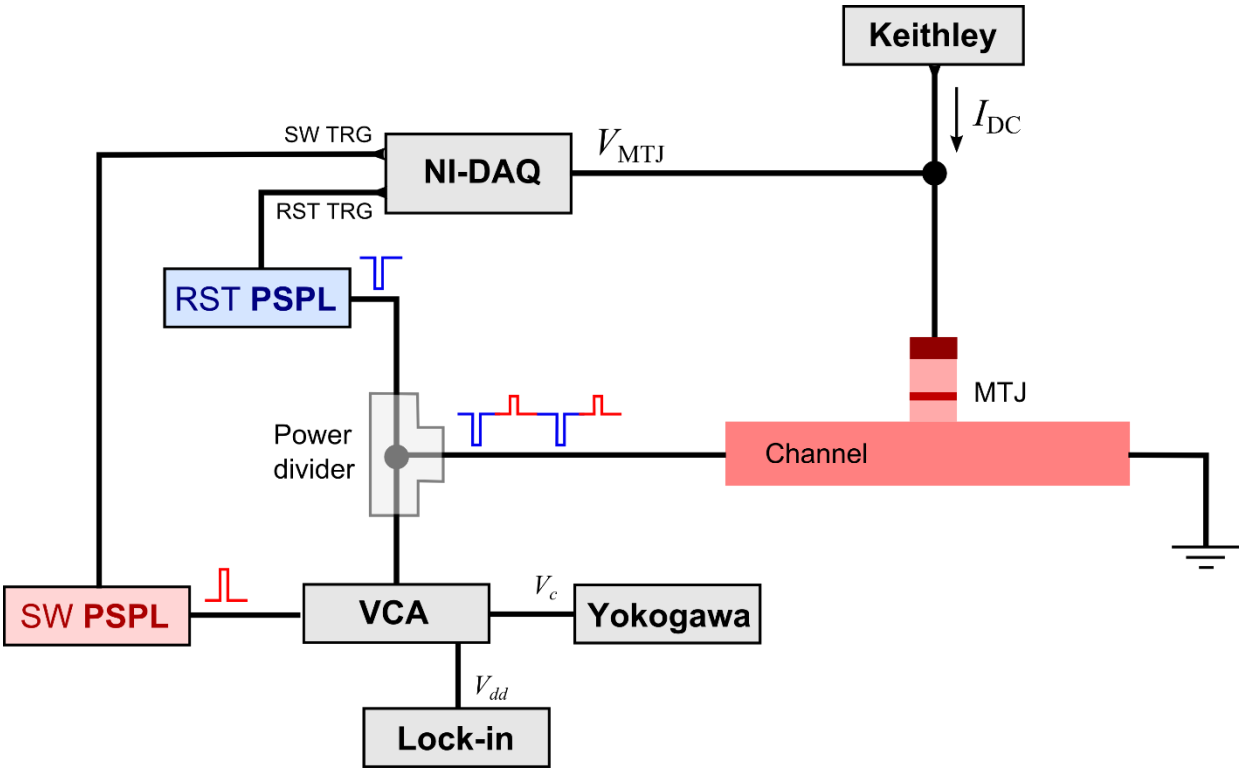

Figure 6.S2: Diagram of pulse switching measurement circuit.

6.S3. Macrospin fitting to pulse switching data of LA devices

Fig. 6.S3 shows the 50% switching probability points for LA devices having different coercive fields (a) and for the LA device having coercive field of 2.3 mT under different bias fields (b). The current density is calculated from the pulse amplitude, taking into account the channel geometry, resistance and the wave reflection at the RF probe's tip due to impedance mismatch of the transmission line and the more resistive channel. The bias field is the externally applied field substrated by the offset field (center of the magnetic minor loop). The solid lines in Fig. 6.S3 show the fitted results to the macrospin model as described by equation (6.3) in the main text. The fitted parameters are summarized in Fig. 6.3 in the main text.

For two cases (a) and (b), an asymmetry between P to AP and AP to P transition is clearly seen. The critical current density of P to AP transition is slightly lower than that of AP to P, which is opposite to the simulation results for pure Pt devices [8]. Moreover, the macrospin fitted line do not match well with the data points. This strongly indicates the complex switching dynamics due to the combination of SHE-induced anti-damping and field-like spin-torque and the considerable Oersted field on the evolution and reversal of magnetic domains of the free layer.

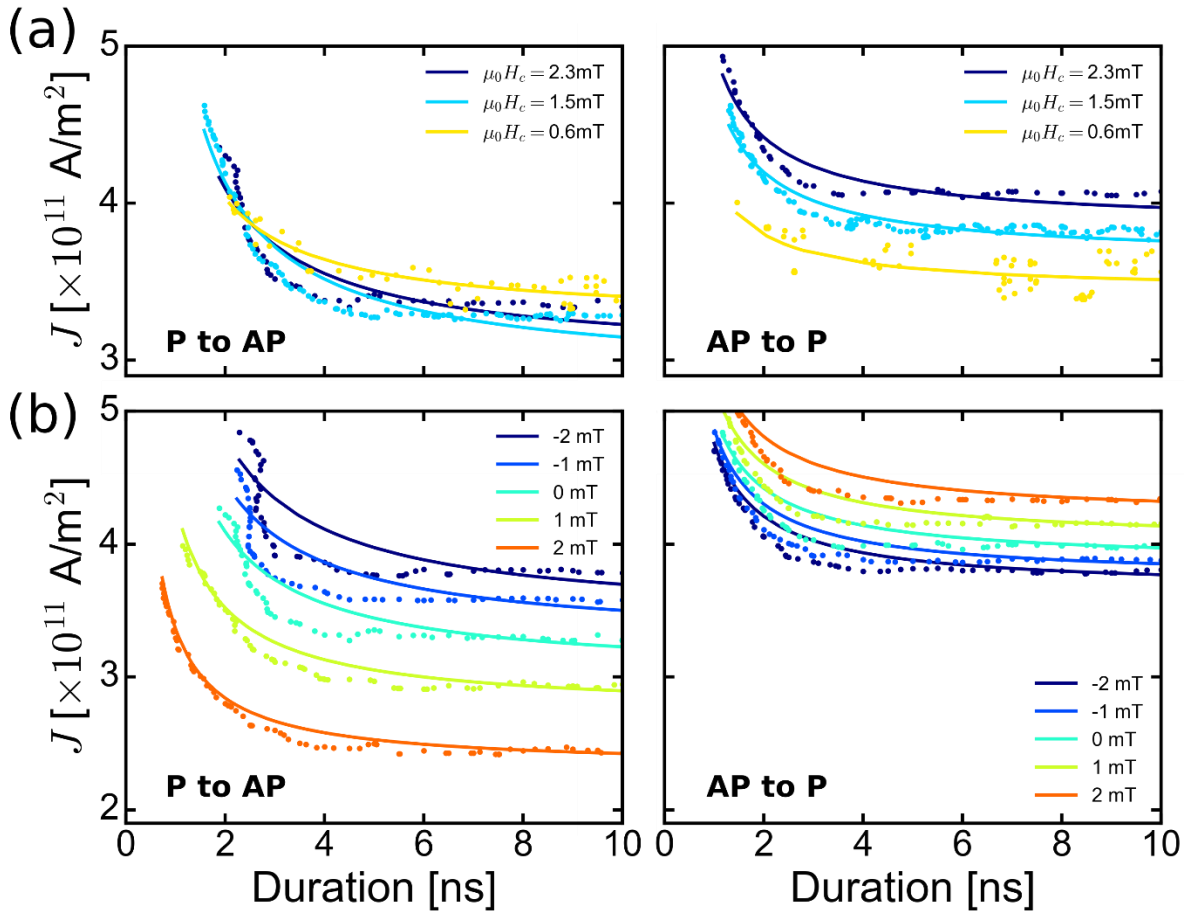

Figure 6.S3: (Pulse) 50% switching probability points at varying pulse current density and duration for LA devices having different coercive fields (a) and for an LA device (having coercive field of 2.3 mT) under different bias fields (b). Solid lines show fitted results to the macrospin model.

REFERENCES

[1] A. D. Kent and D. C. Worledge, Nat. Nanotech. **10**, 187 (2015).

[2] D. C. Ralph and M. D. Stiles, J. Magn. Magn. Mater. **320**, 1190 (2008).

[3] M. I. Dyakonov and V. I. Perel, Phys. Leters **35A**, 459 (1971).

[4] J. Hirsch, Phys. Rev. Lett. **83**, 1834 (1999).

[5] S. Zhang, Phys. Rev. Lett. **85**, 393 (2000).

[6] L. Liu, C.-F. Pai, Y. Li, H. W. Tseng, D. C. Ralph, and R. A. Buhrman, Science **336**, 555 (2012).

[7] S. V. Aradhya, G. E. Rowlands, J. Oh, D. C. Ralph, and R. A. Buhrman, Nano Lett. **16**, 5987 (2016).

[8] G. E. Rowlands, S. V. Aradhya, S. Shi, E. H. Yandel, J. Oh, D. C. Ralph, and R. A. Buhrman, Appl. Phys. Lett. **110**, 122402 (2017).

[9] M.-H. Nguyen, C.-F. Pai, K. X. Nguyen, D. A. Muller, D. C. Ralph, and R. A. Buhrman, Appl. Phys. Lett. **106**, 222402 (2015).

[10] C. T. Boone, H. T. Nembach, J. M. Shaw, and T. J. Silva, J. Appl. Phys. **113**, 153906 (2013).

[11] C.-F. Pai, Y. Ou, L. H. Vilela-Leão, D. C. Ralph, and R. A. Buhrman, Phys. Rev. B **92**, 064426 (2015).

[12] W. Zhang, W. Han, X. Jiang, S.-H. Yang, and S. S. P. Parkin, Nat. Phys. **11**, 496 (2015).

[13] L. Liu, T. Moriyama, D. C. Ralph, and R. A. Buhrman, Phys. Rev. Lett. **106**, 036601 (2011).

[14] C.-F. Pai, L. Liu, Y. Li, H. W. Tseng, D. C. Ralph, and R. A. Buhrman, Appl. Phys. Lett. **101**, 122404 (2012).

[15] A. Ghosh, K. Garello, C. O. Avci, M. Gabureac, and P. Gambardella, Phys. Rev. Appl. **7**, 014004 (2017).

[16] K.-U. Demasius, T. Phung, W. Zhang, B. P. Hughes, S.-H. Yang, A. Kellock, W. Han, A. Pushp, and S. S. P. Parkin, Nat. Commun. **7**, 10644 (2015).

[17] H. An, Y. Kageyama, Y. Kanno, N. Enishi, and K. Ando, Nat. Commun. **7**, 13069 (2016).

[18] M.-H. Nguyen, M. Zhao, D. C. Ralph, and R. A. Buhrman, Appl. Phys. Lett. **108**, 242407 (2016).

[19] Y. Ou, S. Shi, D. C. Ralph, and R. A. Buhrman, Phys. Rev. B **93**, 220405(R) (2016).

[20] Y. Niimi, Y. Kawanishi, D. H. Wei, C. Deranlot, H. X. Yang, M. Chshiev, T. Valet, A. Fert, and Y. Otani, Phys. Rev. Lett. **109**, 156602 (2012).

[21] Y. Niimi, M. Morota, D. H. Wei, C. Deranlot, M. Basletic, A. Hamzic, A. Fert, and Y. Otani, Phys. Rev. Lett. **106**, 126601 (2011).

[22] Y. Niimi, H. Suzuki, Y. Kawanishi, Y. Omori, T. Valet, A. Fert, and Y. Otani, Phys. Rev. B **89**, 054401 (2014).

[23] P. Laczkowski, J.-C. Rojas-Sánchez, W. Savero-Torres, H. Jaffrès, N. Reyren, C. Deranlot, L. Notin, C. Beigné, A. Marty, J.-P. Attané, L. Vila, J.-M. George, and A. Fert, Appl. Phys. Lett. **104**, 142403 (2014).

[24] L. K. Zou, S. H. Wang, Y. Zhang, J. R. Sun, J. W. Cai, and S. S. Kang, Phys. Rev. B **93**, 014422 (2016).

[25] M. Morota, Y. Niimi, K. Ohnishi, D. H. Wei, T. Tanaka, H. Kontani, T. Kimura, and Y. Otani, Phys. Rev. B **83**, 174405 (2011).

[26] M. Isasa, E. Villamor, L. E. Hueso, M. Gradhand, and F. Casanova, Phys. Rev. B **91**, 024402 (2015).

[27] M.-H. Nguyen, D. C. Ralph, and R. A. Buhrman, Phys. Rev. Lett. **116**, 126601 (2016).

[28] E. Sagasta, Y. Omori, M. Isasa, M. Gradhand, L. E. Hueso, Y. Niimi, Y. Otani, and F. Casanova, Phys. Rev. B **94**, 060412(R) (2016).

[29] L. Wang, R. J. H. Wesselink, Y. Liu, Z. Yuan, K. Xia, and P. J. Kelly, Phys. Rev. Lett. **116**, 196602 (2016).

[30] E. B. Myers, F. J. Albert, J. C. Sankey, E. Bonet, R. A. Buhrman, and D. C. Ralph, Phys. Rev. Lett. **89**, 196801 (2002).

[31] P. M. Braganca, I. N. Krivorotov, O. Ozatay, A. G. F. Garcia, N. C. Emley, J. C. Sankey, D. C. Ralph, and R. A. Buhrman, Appl. Phys. Lett. **87**, 112507 (2005).

[32] J. Z. Sun, Phys. Rev. B **62**, 570 (2000).

[33] J.-C. Rojas-Sánchez, N. Reyren, P. Laczkowski, W. Savero, J.-P. Attané, C. Deranlot, M. Jamet, J.-M. George, L. Vila, and H. Jaffrès, Phys. Rev. Lett. **112**, 106602 (2014).

[34] R. H. Koch, J. A. Katine, and J. Z. Sun, Phys. Rev. Lett. **92**, 088302 (2004).

[35] X. Fan, H. Celik, J. Wu, C. Ni, K.-J. Lee, V. O. Lorenz, and J. Q. Xiao, Nat. Commun. **5**, 3042 (2014).

[36] Y. Ou, C. F. Pai, S. Shi, D. C. Ralph, and R. A. Buhrman, Phys. Rev. B **94**, 140414(R) (2016).

[37] S. Emori, T. Nan, A. M. Belkessam, X. Wang, A. D. Matyushov, C. J. Babroski, Y. Gao, H. Lin, and N. X. Sun, Phys. Rev. B **93**, 180402 (2016).

CHAPTER 7

Conclusion and Outlook

The Pt thickness dependence of the spin torque efficiency in perpendicularly magnetized anisotropy (PMA) Pt/Co bilayers, discussed in chapter 2, strongly supports the intrinsic spin Hall effect (SHE) mechanism being dominant in Pt in which the spin Hall conductivity is the characteristic constant. The spin Hall angle (SHA), however, is proportional to the electrical resistivity which may be nonuniform in very thin Pt films. Although the spin Hall conductivity is a more fundamental parameter in studying the SHE in Pt, the (averaged) SHA is still a good figure of merit for switching applications. Thus, it is beneficial to enhance the SHA of Pt by increasing the resistivity as long as the spin Hall conductivity remains relatively constant. As described in chapter 3, the damping-like (DL) spin torque efficiency of $Pt_{85}Hf_{15}$ alloy is estimated to be 0.16 – 0.23, about 2 times higher than that of pure Pt (0.7 – 0.12), depending on the interfacial spin transparency, in PMA multilayers with thin Co. The 2 times higher spin torque efficiency of PtHf is confirmed by the DC and pulse switching measurements of the in-plane magnetized three-terminal magnetic tunnel junction (3T-MTJ) devices, detailed in chapter 6, whose results show that the critical current density of the 3T-MTJ device having PtHf channel and a thin Hf spacer is reduced by a factor of 3 for DC and 2 for pulse measurements comparing to its pure Pt counterpart. These measurements also confirmed the results presented in chapter 4 showing that a thin, < 1 nm, Hf spacer between the Pt and the FM layers reduces the Gilbert magnetic damping by a factor of 2 without significant detrimental effect on the interfacial transparency. These results strongly suggest the PtHf-based 3T-MTJ structure a promising candidate for power efficient and fast magnetic memory applications. The performance of the Pt-based 3T-MTJ devices is shown in

chapter 5 to be robust at a cryogenic temperature of 3.1 K and easy to integrate with superconducting logic devices.

Despite the rapid development in research on the SHE in heavy metals, many questions are still remain unanswered. The existence of the field-like (FL) spin torque associated with the SHE-induced DL torque complicates the analysis of ST-FMR measurements. Although a remedy was proposed [1], it is based on the assumption that both the DL and FL torque efficiencies are constant over a wide range of ferromagnet (FM) or normal metal (NM) thickness, which does not hold in general. Micromagnetic simulations [2] show the important role of field-like effects in the evolution and reversal of the magnetic domains of the FM free layer in 3T-MTJ devices, consequently in the critical current density and speed of the devices; however better quantitative models which take into account both the DL and FL torques are needed. A report by Emori *et al*. suggests that a FL torque can originate from the FM/oxide interface even without the presence of the spin Hall layer [3], indicating the presence of interfacial Rashba-Edelstein effect. However, counter-evidence reported by Ou *et al*. prove the connection of the FL torque and the SHE-induced spin current from the spin Hall layer [4]. Thus, the origin(s) and nature of the FL torque still remain unclear.

The analyses used in the works presented here assume all the spin current comes from the bulk of the Pt layer without dependence on the magnetization of the adjacent FM layer. Recent theoretical works [5,6] suggest a considerable contribution from the interface to the overall spin current, and that the spin transmission through the interface may depend on the FM magnetization. So far there is no conclusive experimental determination of the interfacial component of the SHE.

For MRAM applications, it is crucial to search for stronger SHE materials as well as more efficient switching mechanisms. Efforts have been made into studying the SHE in binary alloys of

strong SHE metals, such as PtMn [7] and W oxides [8], and topological insulators [9]. It is suggested by experiments [10] and micromagnetic simulations [2] that the FL effect by the FL spin torque and current-induced Oersted field can be harnessed to speed up the magnetic reversal, results in faster switching with minimal incubation delay. The shape of the MTJ in 3T-MTJ devices, which determines the magnetic profile of the FM layers, can be engineered to boost up the performance. Beside applications in 3T-MTJ structures, the giant SHE in heavy metals is also used for driving magnetic domains [11] and skyrmions [12].

REFERENCES

[1] C.-F. Pai, Y. Ou, L. H. Vilela-Leão, D. C. Ralph, and R. A. Buhrman, Phys. Rev. B **92**, 064426 (2015).

[2] G. E. Rowlands, S. V. Aradhya, S. Shi, E. H. Yandel, J. Oh, D. C. Ralph, and R. A. Buhrman, Appl. Phys. Lett. **110**, 122402 (2017).

[3] S. Emori, T. Nan, A. M. Belkessam, X. Wang, A. D. Matyushov, C. J. Babroski, Y. Gao, H. Lin, and N. X. Sun, Phys. Rev. B **93**, 180402 (2016).

[4] Y. Ou, C. F. Pai, S. Shi, D. C. Ralph, and R. A. Buhrman, Phys. Rev. B **94**, 140414(R) (2016).

[5] K. Chen and S. Zhang, Phys. Rev. Lett. **114**, 126602 (2015).

[6] L. Wang, R. J. H. Wesselink, Y. Liu, Z. Yuan, K. Xia, and P. J. Kelly, Phys. Rev. Lett. **116**, 196602 (2016).

[7] Y. Ou, S. Shi, D. C. Ralph, and R. A. Buhrman, Phys. Rev. B **93**, 220405(R) (2016).

[8] K.-U. Demasius, T. Phung, W. Zhang, B. P. Hughes, S.-H. Yang, A. Kellock, W. Han, A. Pushp, and S. S. P. Parkin, Nat. Commun. **7**, 10644 (2015).

[9] A. R. Mellnik, J. S. Lee, A. Richardella, J. L. Grab, P. J. Mintun, M. H. Fischer, A. Vaezi, A. Manchon, E.-A. Kim, N. Samarth, and D. C. Ralph, Nature **511**, 449 (2014).

[10] S. V. Aradhya, G. E. Rowlands, J. Oh, D. C. Ralph, and R. A. Buhrman, Nano Lett. **16**, 5987 (2016).

[11] S. Emori, U. Bauer, S.-M. Ahn, E. Martinez, and G. S. D. Beach, Nat. Mater. **12**, 611 (2013).

[12] W. Jiang, P. Upadhyaya, W. Zhang, G. Yu, M. B. Jungfleisch, F. Y. Fradin, J. E. Pearson, Y. Tserkovnyak, K. L. Wang, O. Heinonen, S. G. E. te Velthuis, and A. Hoffmann,

Science **349**, 283 (2015).